CAPACITY FADING INDUCED ON ELECTROCHEMICAL ENERGY STORAGE CELLS AS A RESULT OF HIGH C DISCHARGE

by

Biju Shrestha

Presented to the Faculty of the Graduate School of
The University of Texas at Arlington in Partial Fulfillment
of the Requirements
for the Degree of

DOCTOR OF PHILOSOPHY

THE UNIVERSITY OF TEXAS AT ARLINGTON
December 2013

Acknowledgements

I would like to express the deepest appreciation to my committee chair and advisor Dr. David A. Wetz, who has shown the attitude and the substance of a genius: he continually and persuasively conveyed a spirit of adventure in regard to research and scholarship, and an excitement in regard to teaching. Without his supervision and constant help this dissertation would not have been possible.

Beside my advisor, I would like to thank the rest of my committee member: Dr. Fuqiang Liu, Dr. Rasool Kenarangui, Dr. Wei-Jen Lee, and Dr. William E. Dillon, for their support. I thank my fellow lab mates: Peter, Anthony, James, Jay, Isaac, Clint, Greg, Simon, Nadim, Jamila, and Nathan, for their help.

I would like to thank the college of engineering department at the University of Texas at Arlington for providing me an opportunity to be a student.

Last but not the least; I would like to thank my parents for supporting me throughout my life.

November 20, 2013

Abstract

CYCLING FATIGUE INDUCED ON ELECTROCHEMICAL ENERGY STORAGE CELLS AS A RESULT OF HIGH C DISCHARGE

Biju Shrestha, PhD

The University of Texas at Arlington, 2013

Supervising Professor: David Alan Wetz

A number of electrochemical energy storage devices have been developed and used widely to power portable electronic systems. Lithium-ion batteries are extremely popular for use in portable devices as a result of their high energy density, which is higher than almost all other similar technologies available. Despite their high energy density, most commercial off-the-shelf (COTS) cells are only modestly power dense, limiting them from being used to drive high power or pulsed power applications. Recently, improvements in the electrode structures and electrolytes have led to the development of lithium-ion batteries which have a higher combined power and energy density than ever before. Cells with power densities as high as 28 kW/kg have been developed with energy densities near 52 Wh/kg [8]. In addition to lithium-ion batteries, advanced electrochemical capacitors, such as electric double layer capacitors (EDLC's) and lithium-ion capacitors (LICs), have been developed with extremely high power densities making them a suitable candidate for use in high and pulsed power applications which do not require high energy density. There have been many previous research efforts aimed at understanding the aging of these devices when they are used at their nominal ratings. However, what is lacking is an understanding of how these cells age when they are used to source high currents in either pulsed or continuous modes of operation. This knowledge is critical as high rate currents must be sourced if these devices are to be used in applications such as hybrid electric vehicles, renewable energy platforms, and even high pulsed power applications. The research documented here is aimed at understanding the limitations of these types of devices and to understand their future potential for use in continuous and pulsed high current applications. A novel test stand has been constructed to characterize the performance of these types of devices when they are discharged at rates 10’s to 100’s of times their rated C values in a high frequency pulsed fashion. Three identical high power Nickel- Cobalt-Aluminum-Oxide (NCA) lithium-ion batteries have been cycled at nominal, high C pulsed, and high C continuous rates respectively in order to understand the impact high rate cycling has on the aging of these types of cells. In-situ diagnostics have been used as a means of comparison between the different experimental methods.

Table of Contents

List of Illustrations

List of Tables

Chapter 1

Introduction

Since the commercialization of lithium-ion batteries by Sony in 1991, a large amount of research and development has occurred. These batteries have gotten lighter, smaller, and hold more capacity. Along with these advances in battery research, development, and manufacturing society has greatly increased the amount of wireless devices they possess. The need for high energy storage has become critical to keep up with the ever increasing demands of portable electronics. These devices have found their way into countless people’s everyday lives and have become a necessity for their daily productivity and entertainment. Prior to this advancement in digital technology, most batteries were designed with steady current draws in mind. Because digital electronics as well as power inverters require switching at various frequencies, pulsed discharge profiles of batteries have increased in importance. Not all energy storage devices are created equally and for that reason, no one type of energy storage device technology can power every application. There has been an exponential growth in the capability of energy storage technologies in recent years. Researchers and manufacturers have increased both the energy and power density of electrochemical cells; however, a large improvement in one property most often comes at a cost to the other.

Traditional lithium-ion batteries typically possess a high energy density, but only modest power density. Other technologies, such as electric-double-layer capacitors (EDLCs), often possess opposite properties than that of a lithium-ion battery. There are also lithium-ion capacitors (LICs), which are a hybrid technology offering the same power density as an EDLC along with a slightly larger energy density. More about EDLCs and LICs will be discussed section II. The power and energy densities of these different devices are shown graphically in the Ragone plot found in Figure 1-1.

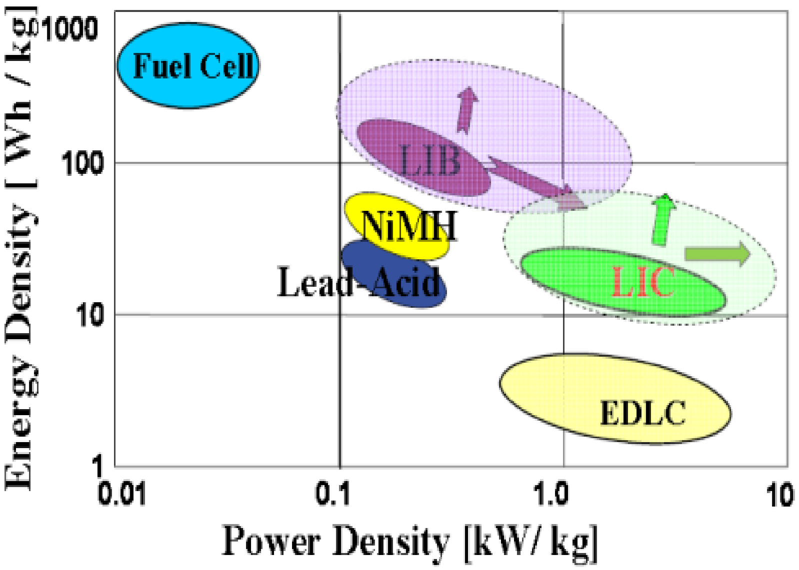

Figure 1-1 Ragone plot comparing the power and energy density of various conventional off-the-shelf energy storage technologies (typical values when these devices are used to power electronic systems in steady state operation) [2]

In a typical portable consumer electronics application, such as a cellular telephone or a laptop computer, a lower power density does not usually cause too many problems and a lithium-ion battery fulfills the needs adequately. In specialty applications, such as a compact high pulsed power system, the prime power source must utilize energy storage devices, which offer a high combined energy density and power density. To meet the demands of this type of advanced system, researchers and manufacturers have been developing new specialty lithium-ion battery technologies which optimize the energy and power density as much as possible. These cells gain their higher power density from their lower internal equivalent series resistance (ESR) which can be less than 1 mΩ in some cases [6][8][9]. The decrease in the internal ESR has increased the available power density significantly and in many cases the power density of the specialty lithium-ion batteries can occasionally exceed that of EDLCs [6][8][10]. The increased power density comes at the cost of a reduced energy density when compared to that of a traditional lithium-ion battery.

Since lithium-ion batteries are so widely used in countless applications, they have been studied extensively and their aging mechanisms are well understood when they are cycled within their rated conditions [4][11]. Use of the new specialty cells in high power applications is very limited. However, as a result there is very little documentation of any experiments where these types of cells have been used to discharge high currents in a pulsed mode of operation. Chen et.al. showed that a single pulsed current in excess of 5 kA can be extracted from a Saft VL8V lithium-ion battery cell for time durations up to 15 milliseconds [6], and while this proves that lithium-ion batteries are capable of achieving high power densities, it is still unclear how these types of cells perform and age when numerous successive elevated rate discharges are extracted in a pulsed form. Extracting current in a pulsed form at elevated rates is representative of the manner in which these types of devices are operated when their energy is conditioned through a power electronic converter. The converters regulate the power by either stepping it up or stepping it down for the intended application. However, it is unclear how the aging mechanisms and the operational safety of the cells are affected after continuous use in high pulsed modes of operation.

In an effort to pave the way in this area of research, a novel experimental test stand, similar to that of Chen, et. al. [6], with an increased action capability, has been developed and used in the work documented here. The stand has been constructed to perform research aimed at understanding the operational capability, safety, and fundamental aging mechanisms of high power electrochemical energy storage devices when they are cycled at elevated rates in a pulsed fashion. The test stand will be discussed in Chapter 3.

The first development of a rechargeable battery dates back to 1800, as seen in Figure 1-2. In 1859, the lead acid battery was developed and it has truly withstood the test of time. This type of cell is still being used as the starting power source in countless automotive systems. In 1888, the alkaline battery was introduced with a higher energy density compared to lead acid battery. The higher energy density made it more portable, finding its way into portable power sources in the early wars. In 1970, the Ni-Cd battery was introduced into the market and it is still used today in many consumer power tools.

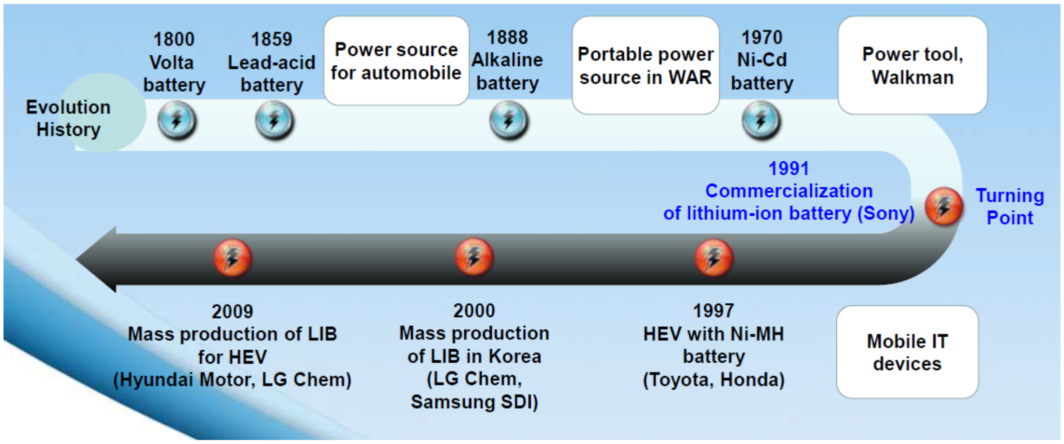

Figure 1-2 Rechargeable battery evolution [1]

In 1991, a turning point occurred with Sony's introduction and commercialization of the lithium-ion battery. The lithium-ion battery packs an order of magnitude higher energy density than previous rechargeable technologies. This led to what has been referred to as the ‘wireless revolution’, forever transforming society's use of portable electronics. In 1997, Toyota and Honda started using Ni-MH batteries in their hybrid electric vehicles (HEVs). Since that time, the lithium-ion battery has significantly matured and mass production of lithium-ion batteries by companies such as LG and Samsung has reached levels previously unthought-of. Current HEVs, such as the Chevrolet Volt, have started using lithium-ion batteries as their renewable energy source. This is only the beginning of what is expected to be a revolution in the automotive industry.

Ever since the introduction of the lithium-ion battery by Sony in 1991, research has continued to improve the energy density of these types of cells. Figure 1-3 shows the trend in increasing gravimetric energy density and volumetric energy density since 1991. A cell, which in 1991 offered a capacity of 860 mAh, can today offer 3000 mAh capacity, approximately 3.5 times higher, without any increase in size.

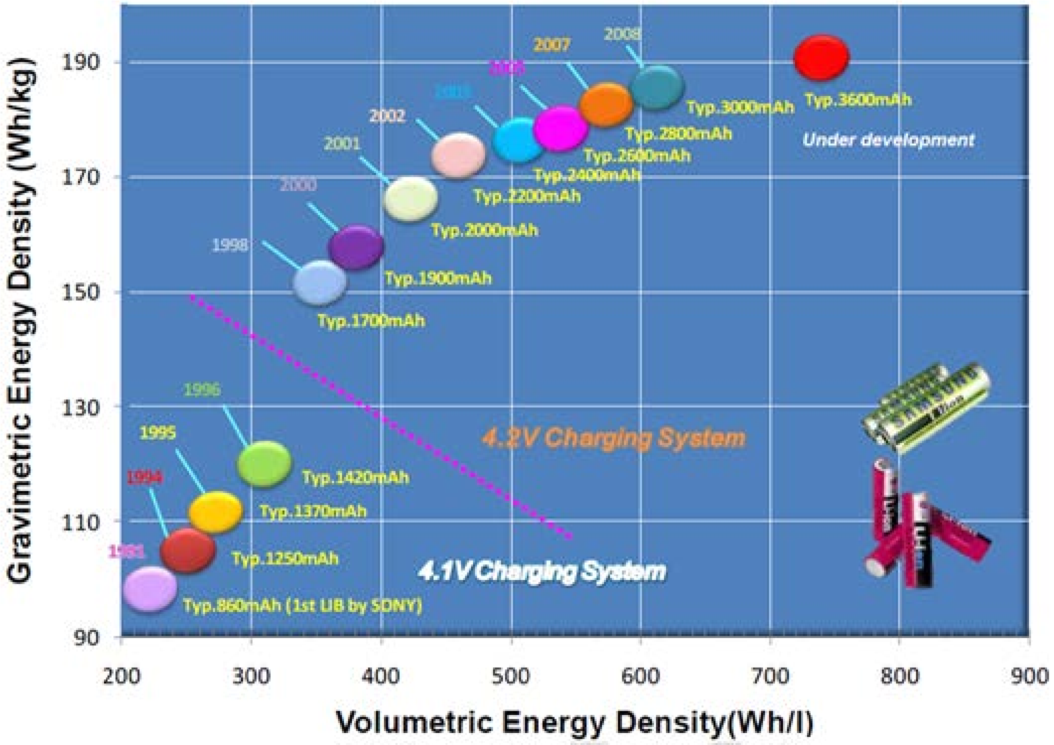

Figure 1-3 Progress on lithium-ion battery [1]

Lithium-ion batteries have become widely used in many devices for many applications, which directly or indirectly affect the quality of life. Figure 1-4 shows the market trends of rechargeable batteries. Batteries with capacities in the range of watt-hour (Wh) are widely used for mobile IT devices. Batteries with capacities in the kWh range are used in transportation sized systems such as electric scooters, hybrid vehicles, etc. Finally, those sized with capacities in mega watt-hour (MWh) range are used as power storage in wind farms, frequency regulation systems, uninterruptible power sources (UPS), etc.

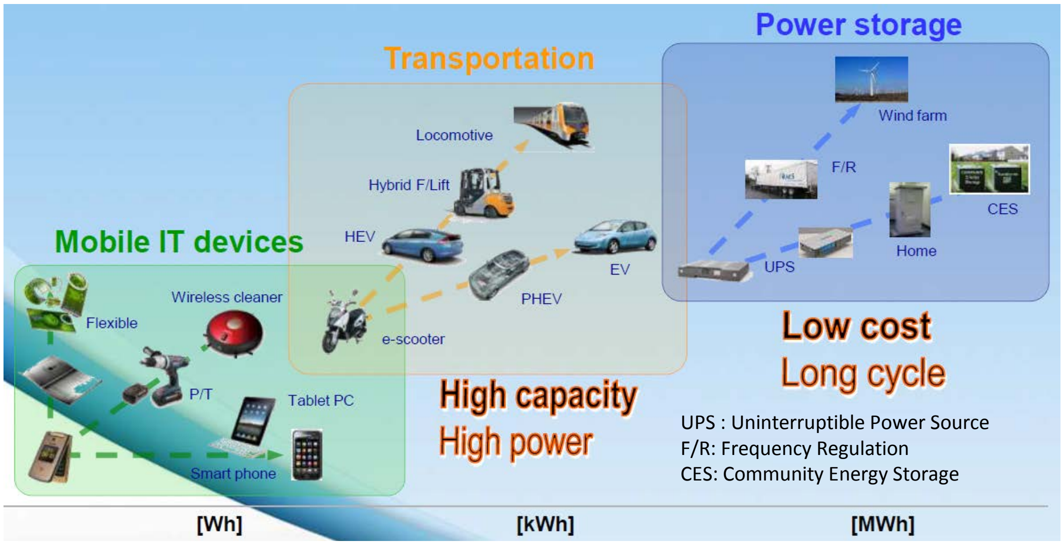

Figure 1-4: Market trends of rechargeable batteries [1]

While these are the typical applications most think of when considering the use of energy storage systems, there is also a high demand for energy storage to be used as the prime power source of high pulsed power applications. Some of these include compact Marx generators, laser systems, electromagnetic (EM) launchers, and seed current sources for flux compression generators, among others. In these applications, as well as all the others previously discussed, power electronic converters are used to regulate the batteries unregulated voltage. These types of converters extract power from the energy storage in the form of pulse width modulated (PWM) current and voltage trains. As the power demanded by the application increases, it is critical that the power density of the energy storage increase as well. How lithium-ion batteries age when they are used to source high pulsed currents to power electronic converters is unclear and this research aims to better educate the community about the aging of electrochemical devices in these types of conditions.

There have been numerous studies performed on rechargeable batteries, including lithium batteries, to better understand their performance limitation and aging over time. These studies have been limited to devices typically commercially available off the shelf (COTS) and at nominal rates in continuous modes of operation. Few if any published studies are available which document how batteries age when they are operated in high C rate pulsed modes of operation. Furthermore, few, if any, studies are available documenting how specialty high power cells age when they are cycled at high current rates, the mode of operation for which they are specifically designed. This work aims to fill these technological gaps.

Chapter 2

Background

Pulsed power

The work here is being performed to understand how batteries age when they are used to supply current, and therefore power, to a load in a high continuous and pulsed mode of operation. Among many others, the key applications that will utilize batteries in this mode of operation are HEVs, grid backup storage, and pulsed power systems. It is assumed that most readers will be familiar with the HEV and grid backup applications as these are commonly discussed and used in most everyday life. Pulsed power, on the other hand, is much more limited in scope and application. For this reason it will be briefly described here.

Pulsed power is a scheme where energy is taken from a high energy source, which is almost always grid tied, and stored slowly in an intermediate energy storage device with a high power density. One stored, the energy is discharged rapidly as electrical energy, into a load, in a single short pulse or as short pulses with a controllable repetition rate. Figure 2-1 illustrates the transformation of power in pulsed power systems. As seen here, the energy is first stored slowly at modest voltage, current, and power rates. The energy is then discharged, often through a single or many stages of pulse compression, resulting in the same amount of energy being compressed into a pulse with a high peak to average power ratio.

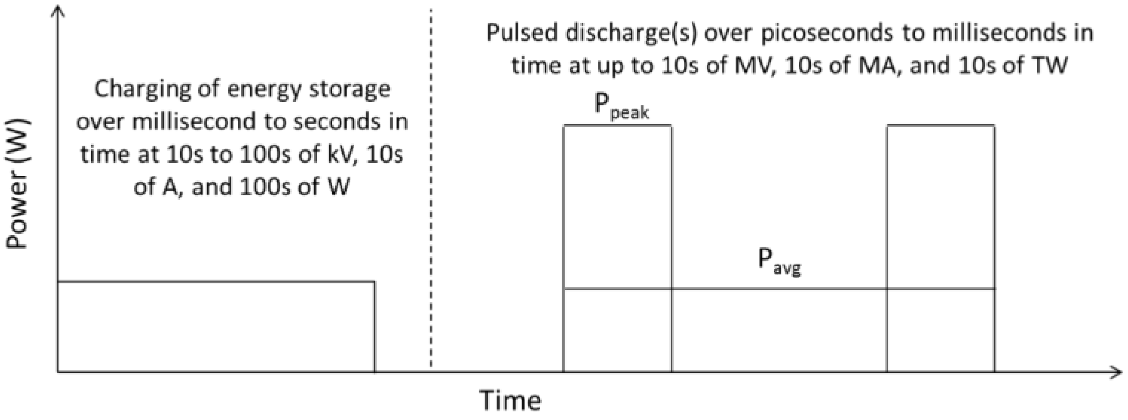

Figure 2-1: Use of pulsed power as a method for pulsed discharge

Figure 2-2 describes the typical architecture of a pulsed power system. Such a system is made up of prime power source which supplies energy to an intermediate energy storage system. Generally, the intermediate energy storage is a set of capacitors, inductors, or rotating machines. The intermediate energy storage is connected to a pulse shaping device through some sort of switch, which is usually either a gas or liquid break down switch, explosive switch, fuse, or solid state device. The pulse shaping device, as the name suggests, is used to shape the pulse's rise time and duration. The output of the pulse shaping lines is finally connected to the load, often through some second form of switch but not always. There are many different types of pulsed power loads with a few listed in Table 2-1 and shown graphically in Figure 2-3.

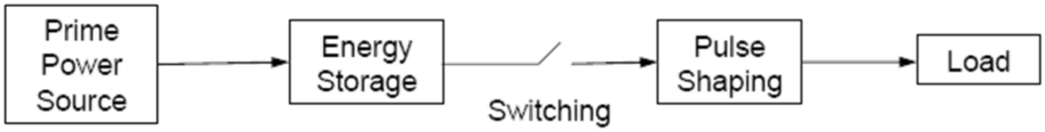

Figure 2-2 Pulsed power systems

Table 2-1 Pulsed power loads

Military	**Civilian**
• Radar	• Radar
• EMP simulation and testing	• Magnetic Forming of Metals
• Nuclear Fusion	• Materials and Surface Treatment
• Nuclear Radiation Effects	• Liquid Shock Wave Application
• Electromagnetic Accelerators	• Medical
• High Power Microwaves	
• Compact and Explosive Flux Compression Generator Systems	

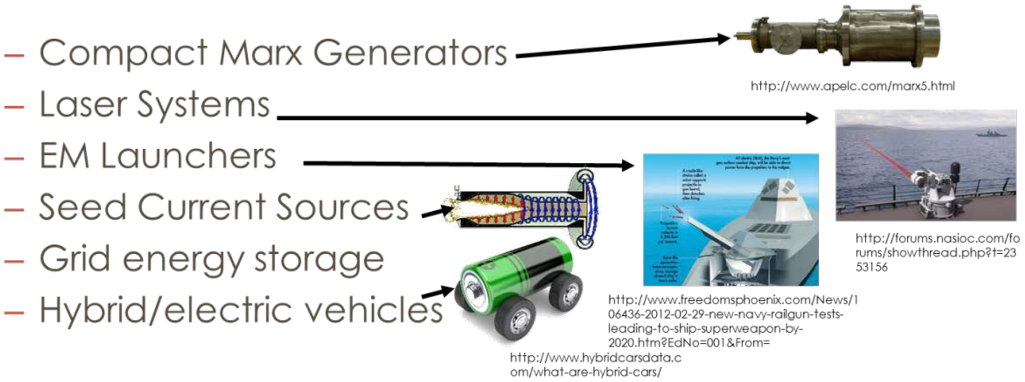

http://www.apelc.com/marx5.html

http://forums.nasioc.com/forums/showthread.php?t=2353156

http://www.freedomsphoenix.com/News/106436-2012-02-29-new-navy-railgun-tests-leading-to-ship-superweapon-by-2020.htm?EdNo=001&From=

http://www.hybridcarsdata.com/what-are-hybrid-cars/

Figure 2-3: Graphical representation of high power loads of interest

As seen in the table most, though not all, of the pulsed power loads are used in military applications. In nearly all of the applications listed, grid connected power supplies are used as the prime power source. In civilian applications, where size and mobility is not of major concern, this is perfectly acceptable and does not limit the use of the pulsed power device. This is not the case in military applications, most of which must be portable, light weight, low volume, and as efficient as possible. These latter requirements make batteries the only feasible option for use as the prime power source on board mobile applications. Often it is feasible to use a vehicles onboard electrical generation to recharge the batteries during any down time when the vehicle is not required to move quickly. During times when the vehicle's on-board generation cannot supply power to the pulsed power system, the batteries must act as the sole prime power source and are used to supply energy to the intermediate energy storage at high rates through a high frequency DC/DC converter.

Use of these types of applications is not new, though several challenges exist when attempting to develop rep-rate pulsed power systems, including input power management, DC-DC converter efficiencies, and thermal management. Each area of focus presents a large window of opportunity for increase in efficiency and optimization of hardware, volume, and mass. When it comes to input power management, the electrical power system utilized on a mobile, platform such as a ship, cannot typically handle high pulsed loads, like the repetitive charge of an intermediate energy storage capacitor bank [42]. In this application, it is most efficient to use batteries as an intermediate storage device in order to directly charge the capacitor on demand, thus presenting a smaller load to the ship's electrical grid in the form of a battery charger system. DC-DC converters are used to boost the lower voltage provided by the battery pack to a level sufficient to charge the high voltage capacitor. As the primary energy source is a limited store of chemical energy, an efficient converter will enable more capacitive charge cycles per battery charge. With any shipboard application, volume is a key metric. As the switching frequency increases in the converter, the required magnetic components, such as the transformer, can shrink in size. With current insulated-gate bipolar transistor (IGBT) technologies, the maximum switching frequency with hard switching is around 20 kHz. Utilizing soft switching topologies can increase the maximum frequency to around

70 kHz. The US Naval Research Laboratories (NRL) is currently developing a demonstration system intended to charge a 4800 µF load to 5 kV within five seconds. The system is designed to repetitively charge the capacitive load at a rate of ten times a minute for five minutes. Lithium iron phosphate ($LiFePO_4$) batteries are being used as the prime power source and a novel DC-DC converter, configured in an LLC configuration, will employ a soft switching topology to maximize efficiency. Despite ongoing development, the authors cite the need to better understand the capabilities of the battery source before success will be achieved. The work performed in this thesis has directly supplied knowledge to this ongoing NRL effort.

Though railgun systems with muzzle energies larger than a few hundred kJ have not been developed or demonstrated which use electrochemical energy storage as its prime power source, a few small scale proof-of-principal ones have been documented by Sitzman [51] and Allen [17]. In Sitzman's design, lithium-ion battery modules developed by Saft Americas are used to source 4 kA into an inductive energy storage element. Utilizing coupled inductors, the seed current is amplified into a roughly 20 kA current pulse, capable of driving a launcher with muzzle energy around 30 J. In the system developed by Allen, dry lead acid batteries act as the prime power source for a 2000 V, 15 mF capacitive pulsed power source that drives a ~15 kJ launcher. A high current, solid-state based inverter and step-up transformer raises the low voltage DC source to a high voltage DC source capable of charging up the capacitors. Though the two systems discussed are conceptually very different, both utilize a form of electrochemical energy storage as their prime power source. This enables them to operate independent of an electrical grid or on-board generator.

Marx generators, ranging in energies from a few J to a few kJ, have been developed using rechargeable batteries as their prime power source. For example, Applied Physical

Electronics L.C. developed a compact 1.8 kJ system that masses 170 kg and can deliver 5 GW to a 25 Ohm HPM load with a peak pulse voltage of 300 kV [18]. The French Department of Defense (DGA) has sponsored research that lead to the development of a compact 1.4 J battery powered Marx generator that produces 1.5 ns pulses with an amplitude of roughly 200 kV [19]. In that generator, six lithium-polymer 7.2-V/1350-mAh battery units are connected in a series/parallel arrangement to create a 16.8 V / 1.5 kW DC primary source. The batteries are able to source enough energy for 35000 shots in this low energy configuration. In 2002, Peterkin, et. Al. of the Naval Surface Warfare Center (NSWC) Dahlgren reported on a testbed that they constructed to evaluate the performance of compact Marx generators [26]. In order to isolate the testbed from the main electrical grid, they utilized a battery pack as the prime power source from which two 50 kV power supplies drew their power to charge the Marx. In the development, they evaluated both lead acid and nickel cadmium (NiCd) battery technologies and ultimately chose to develop a NiCd system. The supply was made up of 264 Sanyo 1800 mAhr batteries configured in a 320 V configuration. The 2 MJ battery source was capable of sourcing 10 kW of average power for short periods of time which requires the batteries to be operated at 22 times their rated C value. Also in 2002, Dragt, et. Al., of Honeywell FM&T in Albuquerque, NM developed a compact battery-powered, 400 kV, 40 J Marx generator that fits in a volume of 6.44 L [20]. Two 12 V, 2.3 Ahr lead acid batteries act as the prime power of the generator which feed two 25 kV DC-DC converters operating in parallel that charge the Marx capacitors. Data presented by Dragt shows that the generator can source a roughly 100 nanosecond wide pulse with a risetime of 20 nanoseconds, a voltage amplitude of 87 kV, and a current of 701 A into a 100 Ohm load.

Another type of pulsed power source that can be used to drive a pulsed power load is one that employs a solid state semiconductor opening switch (SOS) diode to convert energy stored intermediately in an inductor into a useable voltage pulse. As described in [21], an SOS diode is a p+-p-n-n+ structure that is fabricated to obtain an ultra-short reverse-recovery time. The SOS conducts reverse current for the specific characteristic period due to the residual charges in the p and n region of semiconductor structure. The residual charges are provided by the forward pumping current through the SOS diodes. Then, when the polarity of the voltage across the SOS diodes becomes reverse, reverse current flows through the diodes. The recombination of the residual charges in the diode structure results in fast current interruption. This current interruption phenomenon is called the SOS effect.33

In 2000, Lyubutin, et. Al., presented the design of an SOS based quasi-rectangular pulse generator that can drive a 50 kV into a 4 – 5 Ω load for a pulse duration of 100 nanoseconds [22]. The intermediate capacitive store of that design requires a prime power source voltage of 600 V, which can be supplied directly from a series stack of electrochemical devices. Their circuit topology is shown schematically in Figure 2-4.

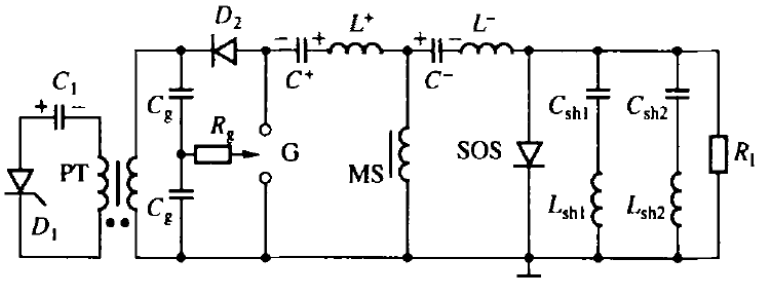

Figure 2-4. Circuit diagram of an SOS diode based pulsed power generator for driving low impedance loads [22].

In SOS based generators, the energy is initially stored in a capacitor, C1 in this case, and is transferred into the magnetic field of an inductive energy storage system, L+ and L-, via a closing switch, which in this case is a spark gap. Often the closing switches are developed in the form of saturable inductors or transformers which combine both the inductive energy store and closing switch into one package. The saturable inductors use cores made of high permeability magnetic material so that the switching transition between the linear and saturation regimes is quick. The closing of the magnetic switch initiates the reverse SOS pumping process and the fast current interruption described above creates a very fast voltage pulse across the load that is proportional to the instantaneous rate of change of current (dI/dt) across of the SOS switch.

In 2006, Bushlyakov, et. Al., documented the design of an SOS based generator that outputs a 400 kV to 1 MV voltage pulse into 50 Ω – 300 Ω loads at peak power levels of 4 GW [23]. Operation at repetition rates of 1 kHz has been demonstrated. Tang, et al., have shown that compact SOS based generators capable of sourcing 4.5 kV for 20 ns and 7.5 kV for 5 ns at 20 Hz into 10 Ohm cuvette loads for medical applications [24]. The brief literature search just presented has shown that several different battery powered high voltage pulsed power sources have been developed that can drive time varying, low impedance loads. Despite this widespread use, no research has been presented to show how the battery energy storage performed and aged as the application was used. This is widely because most of these systems were developed as laboratory demonstration systems which are never widely used. When the work presented here is coupled with the previous work, a complete picture is available of how energy storage devices can be used and will perform in these types of unique pulsed power applications

Energy Storage

Some of the characteristics that are used to determine the applicability of an energy storage technology to an application include the nominal voltage, surge current, energy density, power density, cost per unit energy, number of available charge/discharge cycles, self-discharge rate, and overall efficiency. A typical rating used to identify batteries is its C rating. For those unfamiliar, the C rating of a cell represents the continuous current that it is able to source for one hour. When current is extracted from a cell at its C rate for one hour, the voltage across the cell is decreased from its full rated voltage to its minimum safe operating voltage. If current is extracted at twice the C rated value, the discharge occurs at a rate of 2C and it will be able to supply that current for roughly half an hour. The trend of decreasing discharge time continues as the discharge rate continues to increase. As one may expect, the larger the C rating, the larger the battery. This is because the C rate scales directly to the size of the cell's active electrode area.

Despite the exponential growth in the capabilities of energy storage technologies, it is still impossible to find one type of energy storage technology that can be used to universally power all applications. As seen in Figure 1-1 earlier, each different type of energy storage device has a unique combination of power and energy density. This stems from the unique combination of electrode materials and electrolytes that each technology utilizes. Among the most common types of devices either being used today or being considered for use in the future are lead acid (Pb-acid) batteries, nickel metal hydride (NiMH) batteries, lithium-ion batteries (LIBs), electric-double-layer-capacitors (EDLCs), and lithium-ion capacitors (LICs).

Lead Acid Batteries (Pb-Acid)

Lead acid batteries are the oldest secondary electrochemical cell. They consist of a lead and lead oxide electrode, a separator, and sulfuric acid. The overall chemical equation is shown in equation (1) and (2). Because of their long history, the technology in lead acids is relatively mature and cost effective. The largest drawbacks to these cells is their mass. Lead is one the heaviest elements on the periodic table, which limits its application space. However, certain submersible applications such as submarines and undersea research vehicles make use of the large density as ballast. Lead acid batteries are one of the most economic batteries for larger power applications in which the weight is not an issue. It is used widely in hospital equipment, wheelchairs, emergency lighting and UPS systems. The half reactions of a Pb-Acid battery are given in equations 1 and 2.

Negative electrode reaction:

$$Pb + PbO_2 + 2H_2SO_4 \leftrightarrow \ 2PbSO_4 + 2H_2O \quad (1)$$

Positive electrode reaction:

$$3H^+ + PbO_2 + HSO_4^- + 2e^- \leftrightarrow \ PbSO_4 + 2H_2O \quad (2)$$

Nickel Metal Hydride (NiMH)

NiMH batteries use nickel oxyhydroxide (NiOOH) as a positive electrode and the negative electrodes use a hydrogen-absorbing alloy. The energy density of NiMH is less than that of a lithium-ion cell, typically operating around 1.2 V per cell. The demand of NiMH has fallen significantly with the evolution of LIBs. The significant drawback of NiMH is the high rate of self-discharge which is approximately 20% on first day and up to 4% per day of storage after that. Nickel metal hydrides have been used in the Toyota Prius hybrid electric vehicle. The half cell reactions are given in equations 3 and 4 below.

Negative electrode reaction:

$$H_2O + M + e^- \leftrightarrow OH^- + MH \quad (3)$$

Positive electrode reaction:

$$Ni(OH)^2 + OH^- \leftrightarrow NiO(OH) + H_2O + e^- \quad (4)$$

Lithium-ion Batteries (LiBs)

LIBs have become one of the most common components used in consumer electronics. The LIBs electrodes are constructed from an intercalated lithium compound and graphite while the electrolyte is usually some sort of organic solvent, such as ethylene carbonate, dimethyl carbonate, or diethyl carbonate. During discharge, lithium-ions move from the anode to the cathode. During recharge, the opposite occurs. This is shown graphically in Figure 2-5.

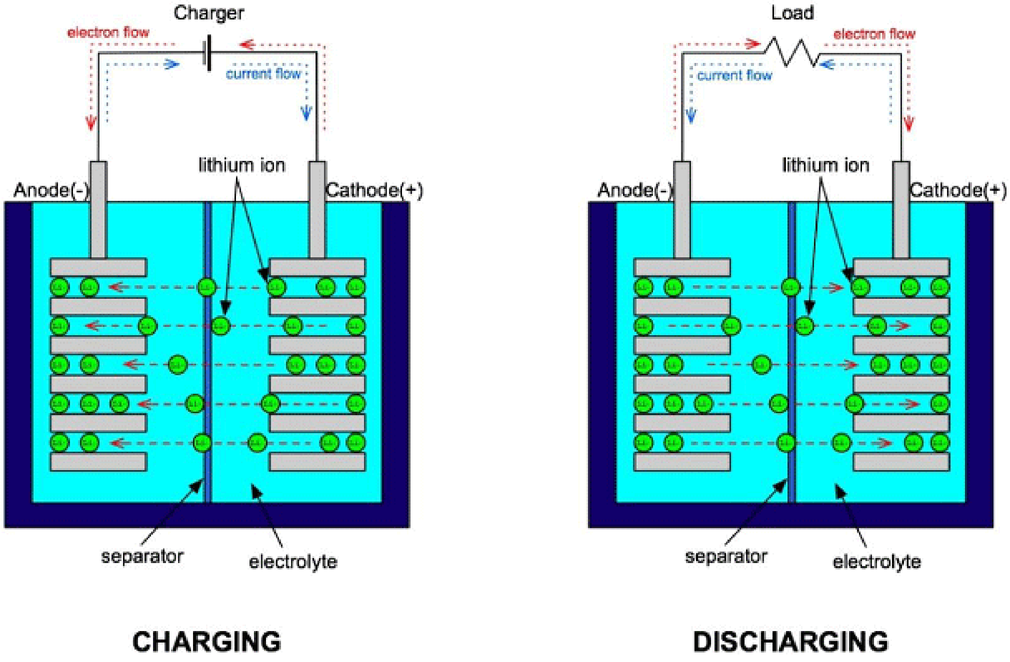

Figure 2-5: Lithium-ion batteries in charging and discharging mode [25]

There are several advantages to using LiBs making them a popular choice. These include having a high energy density, no memory effect, low self-discharge rate, high cell voltage, and high life time. There are several chemistries being used to make up LiBs and which one is used for a particular application depends upon its performance, cost, and safety. A few different chemistries include lithium cobalt oxide ($LiCoO_2$), lithium iron phosphate (LFP), lithium manganese oxide (LMO), lithium nickel manganese cobalt oxide (NMC), lithium titanate (LTO), and lithium nickel cobalt aluminum oxide (LNCAO), among others. The high energy density of LIBs poses several safety hazards and should be handled very carefully. In the work discussed here, cells made up of a few of the different chemistries just listed have been evaluated. The anode half reaction of a $LiCoO_2$ cell is represented in equation 5 while that at the cathode is represented in equation 6.

Negative electrode reaction:

$$xLi^{+} + xe^{-} + 6C \Leftrightarrow Li_{x}\,C_{6} \tag{5}$$

Positive electrode reaction:

$$LiCoO_2 \Leftrightarrow Li_{1-x}CoO_2 + xLi^{+} + xe^{-} \tag{6}$$

Electric Double Layer Capacitors (EDLCs)

Conventional capacitors store energy electrostatically and are very power-dense. However, because of their limited electrode surface area, traditional electrostatic capacitors are not very energy dense. Electric double layer capacitors (EDLC's), also known as supercapacitors, ultracapacitors, or symmetrical capacitors, are a different form of capacitor technology whose unique construction and materials enable them to have a higher energy density then conventional capacitors but also maintain a high power density. The electrodes used in ELDC's are constructed from metallic conductors coated with a porous activated carbon which enables their surface area to be quite high. The electrodes are separated by an electrolyte, which can either be aqueous, non-aqueous, or a solid polymer [27]. While EDLCs provide nowhere near the energy density of lithium-ion batteries their energy density is still quite high, 4.5 Wh/kg, and their power density is significantly higher, 6.94 kW/kg. Additionally, their cycle life has been shown to exceed 100,000 cycles when used near their rated conditions [27].

A simple schematic of an EDLC is shown in Figure 2-6 and Figure 2-7a. A photograph of a cell manufactured by Maxwell Technologies is shown in Figure 2-7b. When a potential is applied across the electrodes, the ions in the electrolyte are polarized. This creates an alignment of opposing charges along the electrode/electrolyte interface. It is important to notice that, like conventional capacitors, the electrodes on either side are identical. Since the area of the electrodes is so large and the charge is separated by an extremely short distance of a few nanometers, the capacitance of the cell is extremely high (100 F/g^{-1}). The large electrode surface area coupled with their light weight (1000 m^2g^{-1}) gives them their high energy density. However, because the charges are separated by such a small distance, the potential the cell is able to provide is small. The potential can be as high as 5V but is normally less than 3 V, in order to prevent electrical breakdown of the cell. One component not shown in the schematic is a dielectric separator running down the center of the cell that prevents the plates from touching and current from flowing through the electrolyte. A number of different electrolyte materials have been tested with various conductivities to minimize the losses in the electrolyte and reduce the series resistance of the cells [27]. A plot of a cell's steady state charge and discharge voltage profile is shown in Figure 2-8Figure 2-8. Since the electrodes are symmetrical, a potential is developed across each electrode/electrolyte interfaces that is equal and opposite to that of the opposing electrode. The output voltage of the cell is the differential voltage developed across the electrodes.

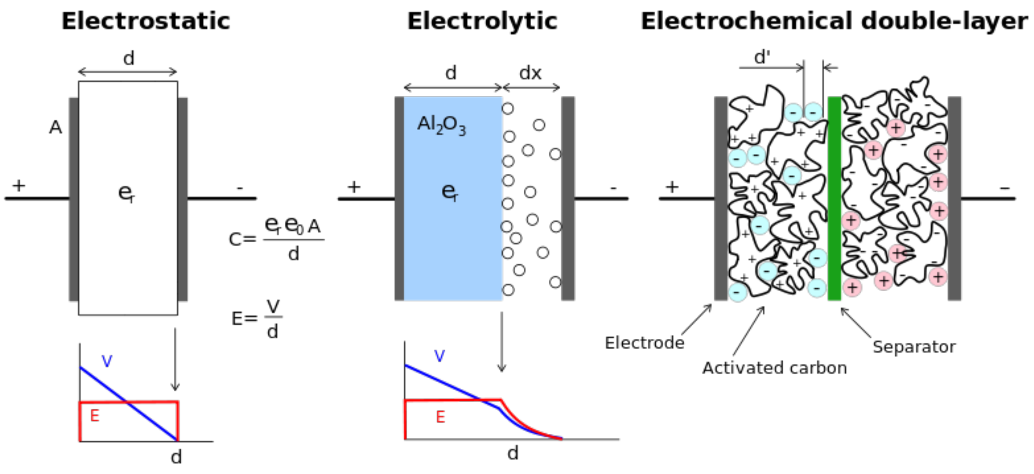

Figure 2-6: Electrochemical double layer capacitor

(a) **(b)**

Figure 2-7. (a) Simple electric double layer capacitor schematic [1] and (b) sample Maxwell technologies K2 series cell [28].

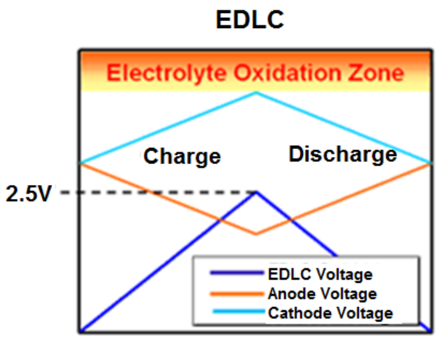

Figure 2-8. Voltage potential profile of an EDLC [29].

There are many types of electrolytes that can be used in ELDCs. The type of electrolyte used really determines the maximum working voltage of the cell. Roughly 1 V is achievable with aqueous electrolytes, 2.3-2.5 V with organic electrolytes, and 3-4 V with ionic liquids. The electrolyte should be resistant to electrochemical reduction and oxidation with carbon and produce high specific capacity at the interface with the electrode [27]. The ionic conductivity of the electrolyte determines the power available from the device. Increasing the temperature, up to the boiling point, strongly increases the conductivity of the electrolyte. It has been noted that in hybrid vehicle applications, heating the electrolyte using waste heat from the combustion engine is feasible [27].

Lithium-ion Capacitors (LiCs)

A simple schematic of a lithium-ion capacitor is shown in Figure 2-9a. As seen in the schematic, a lithium-ion capacitor combines the anode of a lithium-ion battery with one of the electrodes of an EDLC which is why they are typically called asymmetrical capacitors. By doping the anode with lithium, the anode capacity is increased and its potential is held near zero while the potential across the cathode is identical to that in an EDLC. The differential voltage across the cell is therefore larger across a lithium-ion capacitor, seen in Figure 2-10. Due to the fact that the cathode in lithium-ion capacitors do not include an oxygen compound, no thermal chain reaction or thermal runaway occurs since the cathode cannot react with the electrolyte [2][1]. Over charge, over discharge, overheating, and nail punch tests performed by JSR Micro Inc. have shown that thermal runaway doesn’t occur as a result of any of these tests [2][1]. The model shown in Figure 2-9b is a prismatic flat pouch type of cell. As with supercapacitors, the capacitance of the cathode is extremely high due to the porous nature of the activated carbon. Because this technology has only really hit the market within the last ten years, there has been very little research published on this technology.

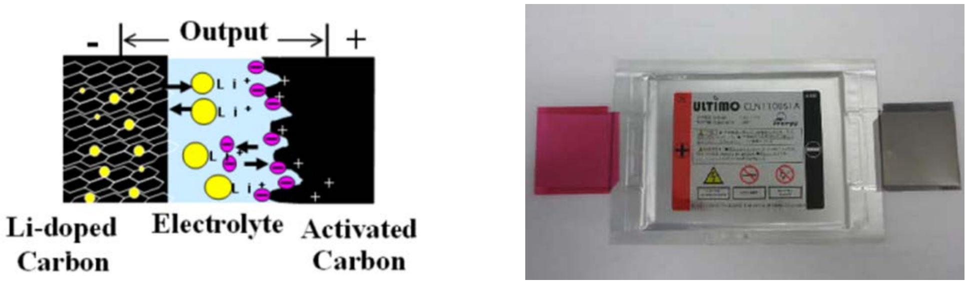

(a) (b)

Figure 2-9. (a) Simple lithium-ion capacitor schematic [2] and (b) sample 2200 F lithium-ion capacitor [2].

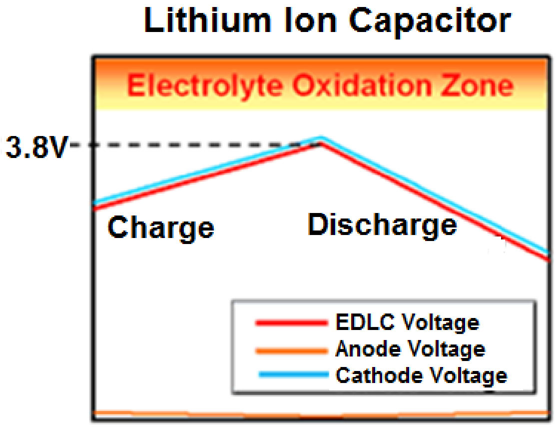

Figure 2-10. Voltage potential profile of a lithium-ion capacitor [2].

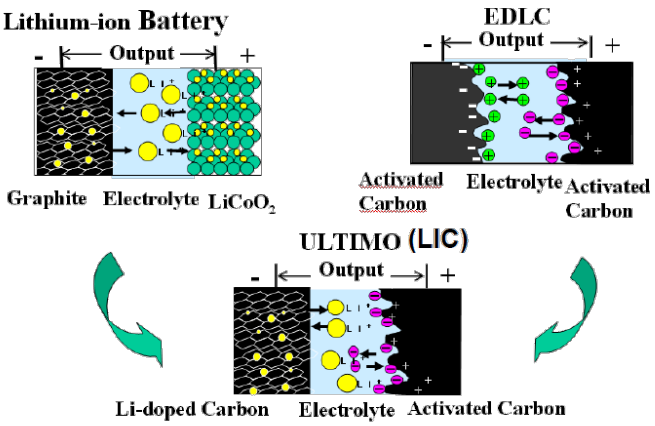

Figure 2-11: Structure of different electrochemical cell [2]

The weight of lithium-ion capacitors is reduced ~66% over that of EDLCs and the volume is reduced by ~80%. The reported energy density of the lithium-ion capacitor is 14.5 Wh/kg which is almost 3 times that of the EDLC (4.5 Wh/kg) [1]. Currently, JSR has manufactured Ultra-low Resistance cells with series resistances of roughly 0.8 mΩ. Despite the higher series resistance, the power density of lithium-ion capacitors is equal to that of EDLCs. In a full DC discharge comparison of a 2,700 F, 2.5 V, supercapacitor and a 2,200 F, 3.8 V, lithium-ion capacitor Lambert, et.al, found that because the supercapacitor could output a larger instantaneous current than the lithium-ion capacitor, ±625 A versus ±250 A, the supercapacitor provided a larger actual instantaneous power, 1.5 kW, than the lithium-ion capacitor, 950W. However, when both devices were discharged at the upper current level of the lithium-ion capacitor, the lithium-ion capacitor provided a greater instantaneous power over 87.5% of its voltage range compared to the supercapacitor [31]. One drawback about lithium-ion capacitors is that like lithium-ion batteries, they should not be completely discharged. Their working voltage is roughly 2.2 V to 3.8 V rather than 0 V to 3.8 V as one might expect.

Self-discharge tests performed by JSR Micro showed >95% voltage retention after being stored at room temperature for over three months. Additionally, after over 100,000 constant current charge and discharge cycles, at 100 A within the safe rated voltage range of 2.2 V – 3.8 V, the cell retained 90 % of its initial capacitance and the DC series resistance increased by ~15% [2].

High Power Electrochemical Cells

As was mentioned earlier, the recent advances in electrochemistry has enabled manufacturers such as Saft, GAIA Advanced Lithium Battery Systems, Maxwell Cooperation, and JM Energy to develop electrochemical energy storage devices that are more power and energy dense than ever before. The ability to reduce the internal impedance below 1 mΩ in many cases has increased the power density and increased the likelihood of using these cells as the prime power source in HEVs, UPS, and pulsed power applications. Cells of varying chemical make-ups have been developed. For example, Saft and GAIA have both developed high power $LiNiCoO_2$ and $LiFePO_4$ batteries that offer different levels of performance and safety. Internal impedances as low as 0.4 mΩ and operating voltages around 4 V are available [9]. As part of the research effort discussed here, a collection of different cells including LIBs, EDLCs and LICs, were experimentally validated using a test protocol in which the cells were each pulsed across a 250μΩ load for 100 ms. All of the cells tested are listed in Table 2-2. More about these experiments will be discussed later, though it is worth noting now that the primary cell evaluated in this research is the Saft Vl3A, which is listed in bold typeface in the table

Table 2-2: Table Datasheet properties from many cells experimentally validated at high pulsed rates

Storage Device	**Mass (kg)**	**Cont Mass (kg)**	**ESR (mΩ)**	**Initial Cell Voltage (V)**	**D.S. Energy Density (Wh/kg)**	**D.S. Pwr. Density (kW/kg)**
GAIA 27 Ah $LiNi_xCo_{1-x}O_2$ LIB [9]	0.939	0.318	1.42	4.1	103.32	1.91
GAIA 18 Ah $LiFePO_4$ LIB [9]	0.918	0.318	0.58	3.8	62.81	2.12
Saft 10 Ah $LiFePO_4$ LIB (Super-Phosphate™ VL10VFe) [16]	0.603	N/A	0.70	3.6	54.73	5.00
Saft 3 Ah LiNixCoyAl1-x-yO2 LIB (VL3)	**0.159**	**N/A**	**1.10**	**4.1**	**12.07**	**20.20**
Saft 22 Ah $LiNi_xCo_yAl_{1-x-y}O_2$ LIB (VL22V) [16]	0.934	N/A	0.32	4.1	89.94	6.35
Saft 34 Ah $LiNi_xCo_yAl_{1-x-y}O_2$ LIB (VL34P) [16]	0.904	N/A	0.35	4.1	132.74	1.32
Saft 30 Ah $LiFePO_4$ LIB (Super-Phosphate™ VL30PFe) [16]	0.926	N/A	0.97	4.1	106.91	1.01
Saft 5Ah LiNixCoyAl1-x-yO2 LIB (VL5U)	0.350	N/A	0.38	4.1	52.14	28.0
2200 F Laminate LIC (STD) [29]	0.214	0.021	1.82	3.8	14.00	3.85
2200F Laminate LIC (LR) [29]	0.265	0.021	1.28	3.8	11.00	5.98
2200F Laminate LIC (ULR) [29]	0.278	0.021	0.61	3.8	10.00	12.0
2000 F Maxwell EDLC [28]	0.414	0.059	0.34	2.7	4.90	6.94
K2 Energy 2.6 Ah $LiFePO_4$ LIB (LPF26650P) [15]	0.081	0.018	11.45	3.6	102.72	1.2
K2 Energy 2.6 Ah $LiFePO_4$ LIB (PK111230-2, 26650) [15]	0.083	0.018	11.37	3.6	100.24	0.75
A123 Systems 2.5 Ah $LiFePO_4$ LIB (26650m1-B Nanophosphate®) [56]	0.072	0.009	10.34	3.6	114.58	1.29
A123 Systems 0.7 Ah Ah $LiFePO_4$ LIB (AHR18700M1Ultra Nanophosphate®) [56]	0.038	0.009	5.11	3.6	60.79	7.71

Electrochemical Cell Aging Mechanisms

Battery manufacturers define the end of a battery's life as the point when it can only deliver roughly 80% of its nameplate capacity. As the reader may expect, each application imposes different requirements from the energy storage. Most manufacturers provide, on their datasheet, the cycle life a user can expect under conditions for which the battery is notionally rated. For example, GAIA informs users that over 1000 cycles can be expected before the capacity of their 18 Ah $LiFePO_4$ cell is reduced to 80% of its initial capacity when it is cycled to 100% DoD at 20^oC under 1C charge and discharge conditions [9]. While this is informative, it provides no information to the user about how the cell will age when it is used in any other conditions that their application may require. This is especially true if the cell is intended to be cycled at high discharge rates. Though the capacity is reduced, a battery is still usable for many non-sensitive applications after end of life at the cost of lower capacity and degradation in performance. With this in mind there have been numerous research efforts performed to better describe the manner in which properties such as temperature, rate and level of charge, rate and level of discharge, and the DoD impact the cycle life of batteries [12]. There have been many research efforts performed in the past to understand the physical processes that occur inside of lithium-ion batteries as they are cycled and age at their nominal power ratings [32][33]. Many of the known causes and effects of various published aging mechanisms are shown in Table 2-3.

Even under normal operation, a battery operates at a voltage range which is beyond the electrochemical stability window of the electrolyte components and the lithium-ion is consumed at interface layer when the system is at charged state [5]. As a result, aging occurs in the bulk electrode and electrolyte materials as well as at the interface between each respective electrode and the common electrolyte. At the anode/electrolyte interface, processes such as graphite exfoliation, electrode cracking, electrolyte decomposition, stabilization, expansion, dissolution, and conversion of the solid electrolyte interphase (SEI) layer, lithium plating, and corrosion are among the possible occurrences [5]. On the cathode side, micro-cracking, electrolyte decomposition, gas evolution, conductive particle oxidation, dissolution, binder decomposition, surface layer formation, and oxidation are among the processes leading to capacity fade and power loss of the cell [5]. Graphics created by [5] briefly summarize these aging mechanisms at the anode/electrolyte and cathode/electrolyte interfaces respectively. Graphics highlighting the anode/electrolyte aging mechanisms are shown in Figure 2-12 and Figure 2-14. Similarly, the aging of cathode/electrolyte interface is summarized in Figure 2-13 and Figure 2-15 [5]. Though the properties summarized in the figures is representative of those occurring in all types of lithium-ion cells, the manner in which the anode and cathode materials age varies from chemistry to chemistry.

Table 2-3: Lithium-ion aging causes and effects [5]

	Cause	Effect	Leads to
1	Electrolyte decomposition (→SEI) (Continuous side reaction at low rate)	Loss of lithium Impedance rise	Capacity fade Power fade
2	Solvent co-intercalation, gas evolution and subsequent cracking formation in particles	Loss of active material (graphite exfoliation), Loss of lithium	Capacity fade
3	Decrease of accessible surface area due to continuous SEI growth	Impedance rise	Power fade
4	Changes in porosity due to volume changes, SEI formation and growth	Impedance rise, Overpotentials	Power fade
5	Contact loss of active material particles due to volume changes during cycling	Loss of active material	Capacity fade
6	Decomposition of binder	Loss of lithium, Loss of mechanical stability	Capacity fade
7	Current collector corrosion	Overpotentials, Impedance rise, Inhomogeneous distribution of current and potential	Power fade, Enhances other ageing mechanisms
8	Metallic lithium plating and subsequent electrolyte decomposition by metallic Li	Loss of lithium (Loss of electrolyte)	Capacity fade (power fade)

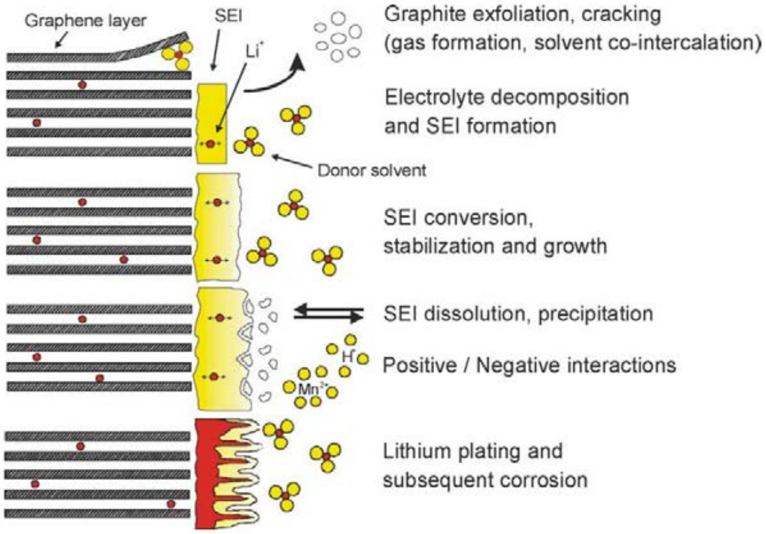

Figure 2-12 Aging of anode materials [5]

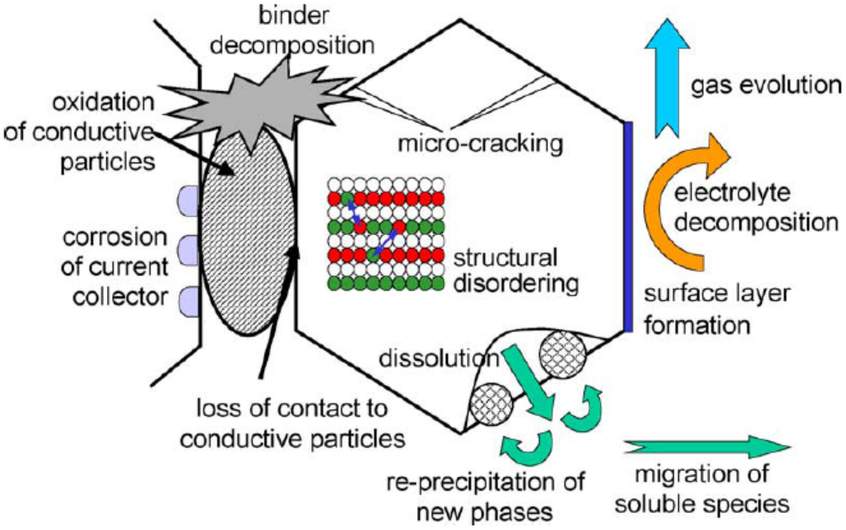

Figure 2-13 Aging of cathode materials [5]

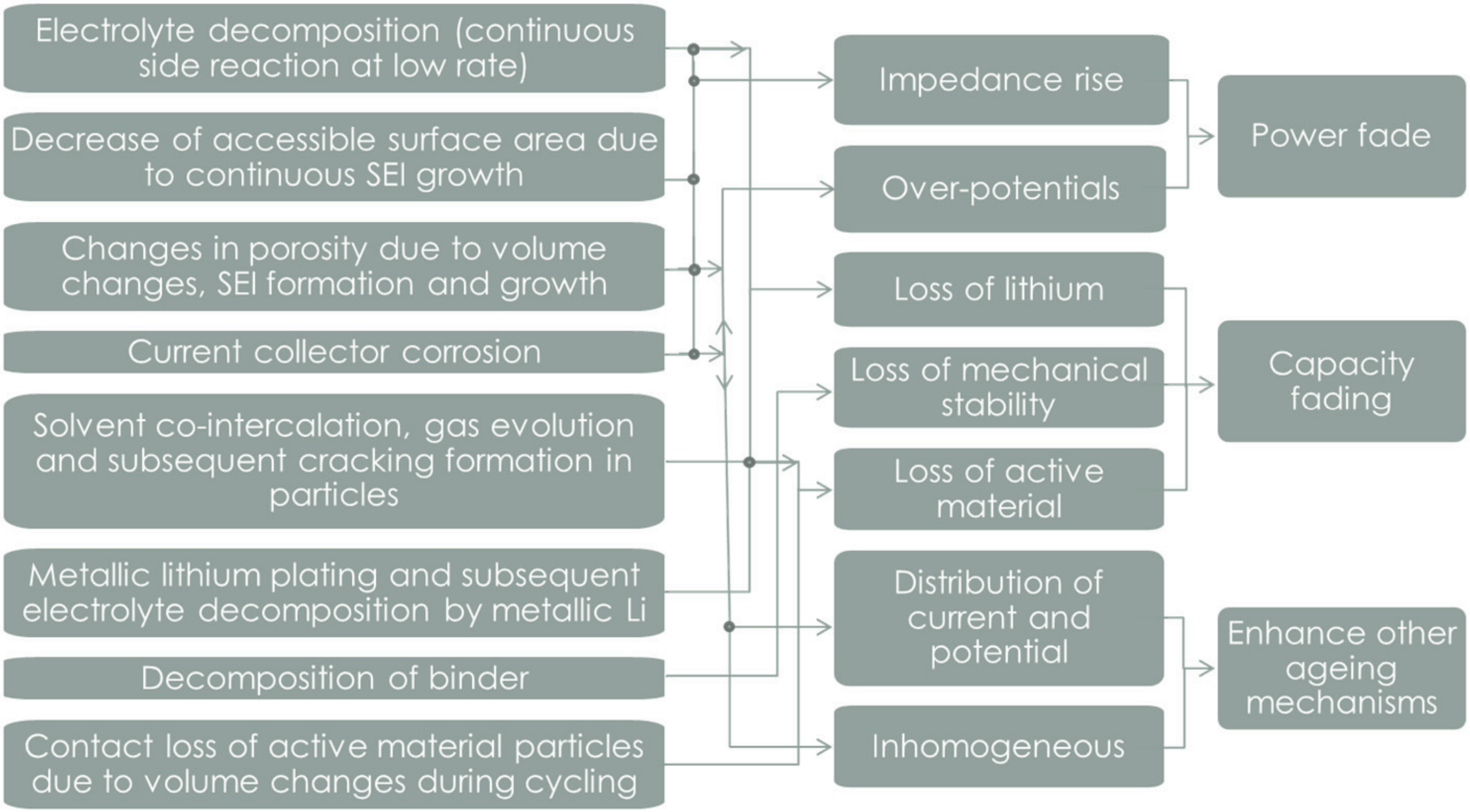

Figure 2-14: Block diagram on aging of anode materials [5]

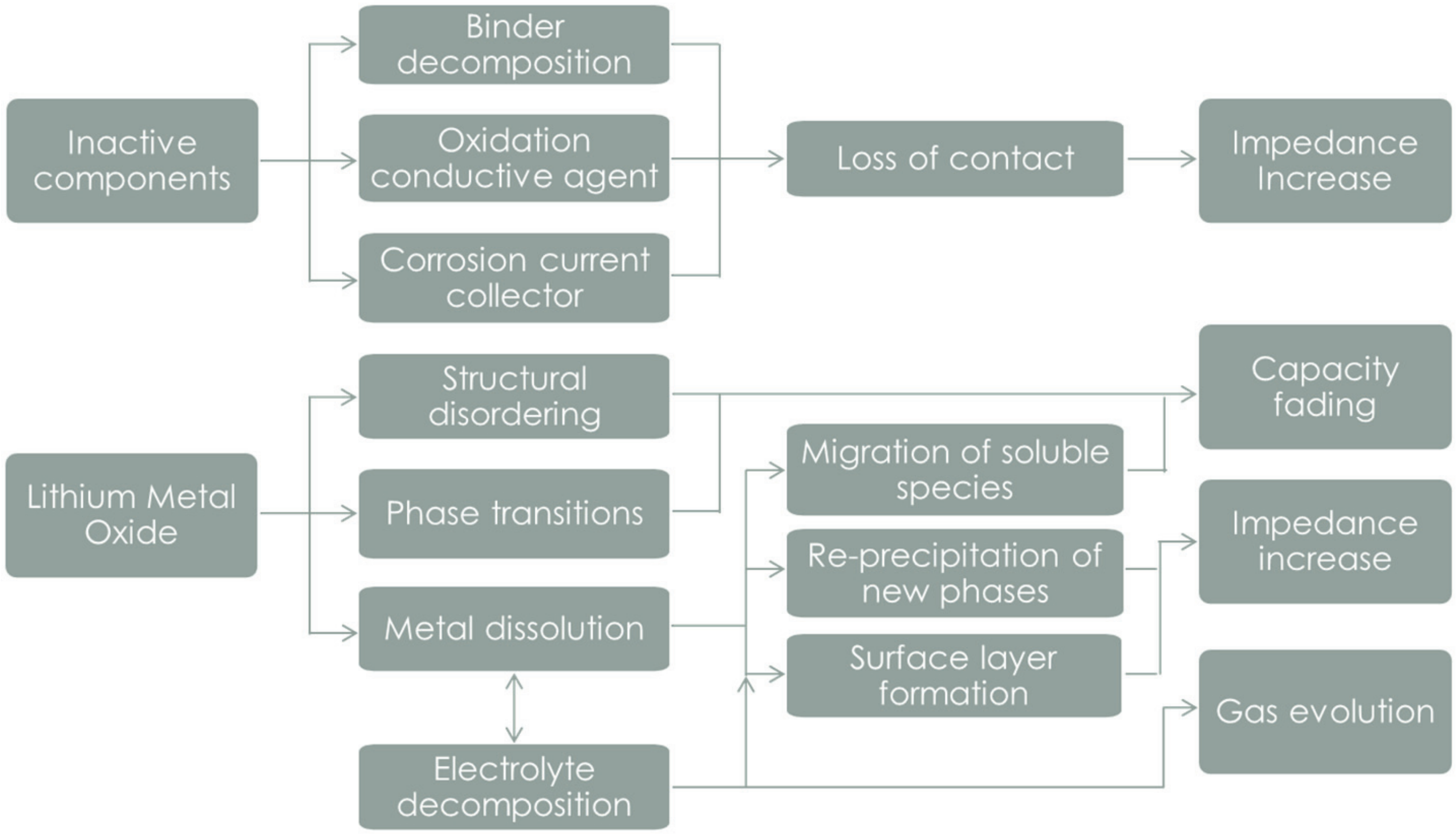

Figure 2-15: Block diagram of aging of cathode materials [5]

When the cell is under use, there occur a chemical reactions and often results in electrochemical decomposition results in a layer formation between anode and an electrolyte. This layer is referred to as solid electrolyte interphase (SEI) layer [57]. At the anode/electrolyte interface, reductive electrolyte decomposition accompanied by irreversible consumption of lithium-ions takes place when the electrode is in the charged state (polarized to low potentials) [5]. As described by [5], the decomposition products build up “protective layers” that cover the electrode’s surface. This process occurs mainly (but not exclusively) at the beginning of cycling, especially during the first cycle and proper formation is critical for a long battery life. The layers, which form on the surface of graphite, may be principally divided in two types according to their different functions. At certain graphite surface sites (i.e., at the prismatic surfaces and defects in basal planes) lithium-ion transport into/from the graphite structure by intercalation/deintercalation takes place. Here, the protective layers have to act as a so-called solid electrolyte interphase, SEI [5]. The properties of the SEI layer are unique since they are in first approximation permeable for lithium cations but rather impermeable for other electrolyte components and electrons. Thus, normally the SEI reasonably protects (i) the electrolyte compounds from further reduction and (ii) the charged electrode from corrosion. At high rates, the rapid diffusion of lithium-ions out of the anode and into the electrolyte can cause hot spots at the interphase layer, causing long term damage. Buildup of the SEI layer over time can also lead to an increased cell impedance, decreasing the overall efficiency and capacity of the cell. Many argue that it is changes in the SEI layer’s stability, structure/composition, and the presence of polluting agents which contribute most to the aging of lithium-ion batteries [11].

On the cathode electrode side, the key factors seem to be material structure evolution and oxidation of the organic solvents [11]. As previously mentioned, the development and use of new specialty high power lithium-ion cells is still quite recent and there have been no documented research efforts detailing the effect extremely elevated discharge rate cycling has on capacity and power fade. This research studies the effect of very high rate continuous and pulsed discharge coupled with 1C charge rate at room temperature without added cooling to the cells.

Though desirable, there are many challenges which must be dealt with when utilizing lithium-ion batteries at high charge and discharge rates. Most simply, high rate operations contribute to an increase in heat generated internal to the cell. The heat is generated as a result of joule heating which is proportional to the square of the current passing through the cell. This means that even a high power lithium-ion battery’s small internal resistance can generate a significant amount of heat when large quantities of charge flow through them. Though elevated temperatures cause the ionic conductivity of the electrolyte to increase, the ratcheting effect of repeated high rate charge and discharge can cause the cell to reach its maximum safe operating temperature rather quickly. If the cell is continuously cycled at high rates and therefore operated at high temperatures, the capacity and cycle life of the cell is adversely affected [34] as the electrolyte is placed under higher stress and may experience decomposition at a faster rate. If it is allowed to get far too hot, it is possible for a non-reversible chemical reaction to occur, leading to either cell failure or even catastrophic damage. Also note that the temperature measured in the experimental results only models the external temperature of the cell. It can be assumed that the internal cell temperature is significantly hotter, and the path of least resistance likely has enough thermal energy to break covalent and ionic bonds.

The ionic diffusion rate is also a concern when high rate procedures are used. Overcharging occurs when a batteries potential exceeds its maximum rating during the charge process. Batteries must be operated within a safe range of voltages, which is chemistry dependent. As expected, the cell’s potential is proportional to the amount of charge stored within each respective electrode. During recharge, ions are de-intercalated from the cathode and intercalated into the anode. While it would be great to be able to transfer 100% of the ions from electrode to electrode during each respective process, extracting too many ions form the cathode during recharge causes the cell to reach a state of irreversibility at which point thermal runaway events can start to occur. The extent of damage done during overcharge is dependent on how far the battery is overcharged. In most of the cases, excessive overcharging causes a significant rise in the cell’s internal temperature and a pressure buildup inside the battery due to gas formation [49][50]. As expected, an excessive pressure buildup can result in an explosion and release toxic chemicals and gases [12]. In one of the lab incident which included charging a lithium-ion battery module without battery monitoring system resulted in overcharging of the battery causing an explosion and release of toxic gases. For example, an experiment in which a Ni-MH battery was overcharged by 0.2 V resulted in roughly a 40% loss of cycle life [12].

When the charge or discharge current rate attempts to force the electrochemical reactions faster than the intercalation or de-intercalation rate of lithium-ions from the respective host material, it may not be possible to fully transition the ions in to and out of each respective electrode. In lithium-ion batteries, the presence of a solid-electrolyte interface (SEI) layer prevents ions from quickly diffusing in and out of the carbon anode. The inability of the ion to work its way into the structure can lead to phenomena such as lithium plating and dendrite growth [35]. In the case of lithium plating, a thin layer of lithium is formed on top of the SEI layer, which further prevents the intercalation of ions. Dendric growth refers to a physical structure that forms on the electrode surface. The dendrite is essentially a concentrated buildup of lithium on the electrode surface. A scanning electron microscope (SEM) image of one such dendrite is displayed in Figure 2-16.

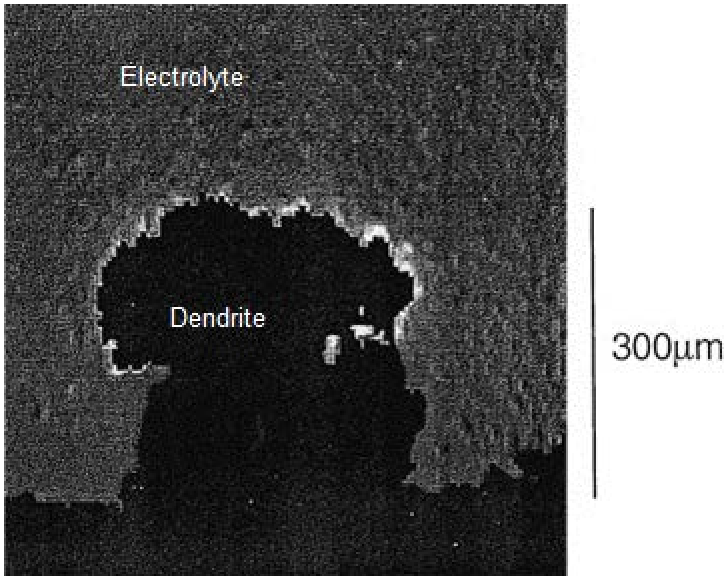

Figure 2-16 SEM image of dendric growth on a graphite anode [35].

If the dendrites are allowed to build long enough, the structures may pierce the separator leading to a possible short circuit of the cell internally. Diffusion also leads to another form of failure, known as salt formation. In normal operation, the salt allows the ion to travel from the anode to the cathode. If there are too many ions present in the electrolyte, as the case with high rate cycling, the highly electropositive lithium cation will bond with a free anion. The type of salt formed depends greatly on what type of electrolyte is used. Regardless of the salt formed, the lithium-ion is no longer available to intercalate, decreasing the overall capacity of the cell

While material degradation may not typically be a primary cause of capacity fading in lithium-ion batteries, it plays a larger role at both electrodes under high rate cycling. Aging at the anode is enhanced by high cycling rates and is evidenced through two primary results which will be discussed in Chapter 4. One source is the volume change that occurs at the active material due to intercalation/de-intercalation which can lead to material breakdown of the composite anode. This can result in contact loss between the carbon particles themselves, the carbon and the current collector, the carbon and the binder, and between the binder and current collector all of which result in a loss of active material. Secondly, the electrode porosity is also affected by the volume change of the active material resulting in an impedance rise of the cell [5]. High rate operation causes structural changes to both electrodes, especially in layered structures. The rapid insertion and removal of ions from the electrode forces the electrode to expand and contract more rapidly than they are notionally designed for. Any mechanical failure of the electrode can result in contact loss either within the electrode itself or between the electrode and the current collectors. In general, contact loss (mechanical or electronic) within the composite electrode results in higher cell impedance. Capacity fading at the NCA cathode is primarily caused by structural changes due to the insertion/extraction of lithium-ions which cause mechanical stress of the electrode. While the aluminum dopant helps lead to a stabilization of the structure reducing the total volume changes, the electrode aging is accelerated by high SOC and high cycling rates [41]. Due to the high cycling rate of this study, it is important to mention the resulting acceleration of the material degradation at both the anode and cathode. Similarly, the higher thermal, mechanical, and quantum-mechanical stresses felt on the SEI layer during high rate operation results in faster conversion or growth of the SEI layer leading to quicker impedance growth.

Over discharging occurs when the battery’s potential is allowed to drop below its minimum rating during discharge. Similar to overcharging, this results in too many ions being removed from the anode and negatively impacts the life of a battery. In an experiment performed where a Ni-MH battery was discharged to 0.3 V, a 66% capacity loss was observed [12]. The DoD at which a cell is cycled to has a significant impact on the cycle life of the battery. This is illustrated graphically in Figure 2-17 [12], where is observed that while a battery lasted for 5000 cycles when discharged to 10% DOD in each cycle, the same type of cell lasted only 500 cycles when it was discharged to 80% DOD at the same rate.

Figure 2-17: Effects of DOD on cycle life [12]

In-Situ Electrochemical Measurements

Despite knowing the possible different changes that may be occurring internally, it is currently nearly impossible to quantify each of the respective mechanism's contribution to the overall aging of a particular cell. The most conclusive analysis technique involves deconstructing the cell upon the completion of cycle life experiments for analysis under a scanning electron microscope (SEM). However this limits the number of experimental parameters that can be studied, and the deconstruction process may alter the cell's properties. Despite these difficulties, it is critical to be able to understand how lithium-ion cells age when they are operated at high rates and to be able to predict when the end of their lifetime is near before they can be widely deployed in directed energy applications. Several in-situ techniques are used to evaluate how cells are aging in real time. A few include simple measurement of the cell voltage and current, measurement of the coulombic efficiency over time, and electrochemical impedance spectroscopy (EIS).

Voltage and Current Measurement

As one may expect, analysis of how a cell is performing is easily evaluated by measuring the voltage across the cell's terminals and the current sourced or sinked by the cell. The voltage measurement is as expected and is simply used to see how the cells voltage decreases as a function of the depth of discharge (DoD). Similarly, it is used to ensure the cell is operated within its safe operating limits. One of the most useful metrics used to evaluate a cell is its capacity, which was briefly discussed earlier when describing the C rating.

Coulomb Counting and Efficiency

As can be expected from the discussion above, coulomb counting is the procedure of measuring and integrating the current flow over time. As the capacity decreases, the coulombs counted will decrease as well providing an indication of the expected usable life of the cell.

A cell's capacity describes the number of coulombs which can be stored in it and then taken out of it to perform electrical work across the load. The capacity is often described in units of Ampere-Hours (Ah). For example a 3 Ah battery is able to supply 3

A across a load for 1 hour, i.e. its 1C rating is 3 Ah. Initially, the nameplate provides the user with the full capacity of the cell. As the cell is cycled, the capacity decreases as a result of the aging mechanisms described earlier. Once the cell's capacity decreases to 80% of the value it had initially, the cell is typically no longer considered usable. The capacity is calculated by measuring the current into and out of the cell and then integrating it with respect to time. This is shown in equation 3.

$$Capacity = \int_0^t I dt \qquad (5)$$

The capacity a cell is able to release or accept is heavily dependent upon the rate at which it is extracted or applied. This is illustrated in Figure 2-18 which shows the discharge curves measured from a GAIA 18 Ah $LiFePO_4$ cell at rates ranging from 0.5C to 35C. At the lower C rate, almost 19 Ah is extracted from the cell. At 35C, only 5.5 Ah is extracted. This variation is heavily determined by the internal voltage drop across the battery's ESR. At higher rates, the lower cell voltage range is reached sooner, preventing the cell's full capacity from being extracted.

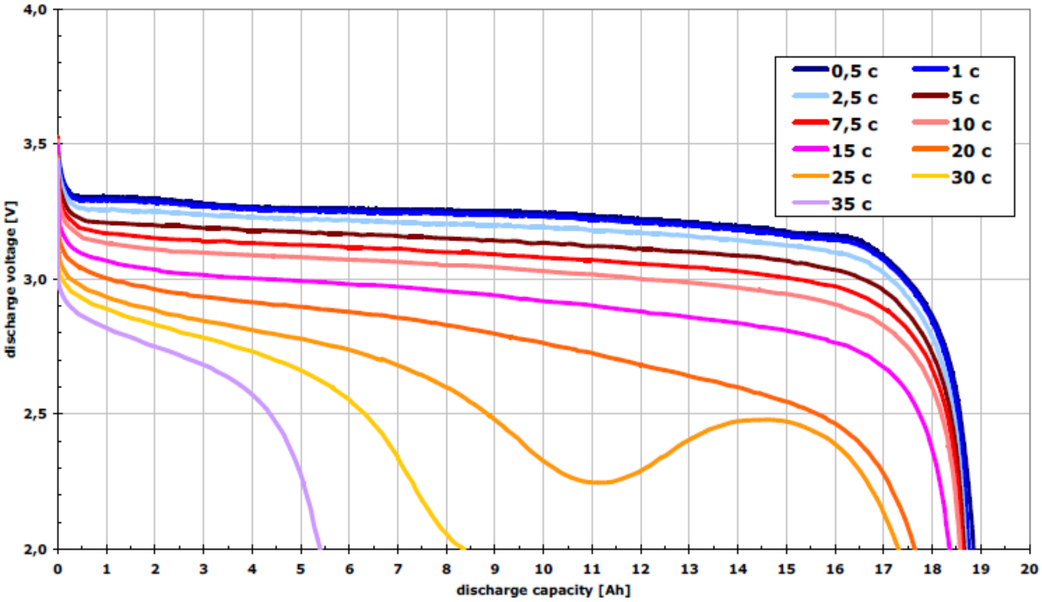

Figure 2-18: Discharge capacity at different C rates for GAIA 18 Ah $LiFePO_4$ [9]

When evaluating the discharge capacity fade of a cell as a function of cycle life, it is critical that the coulombs always be counted at the same discharge rate and after same recharge procedure has been performed. The rate used should always be low, around 1C, in order to provide a fair metric of comparison. Simply evaluating how many coulombs the cell is able to supply as a function of cycle life provides a good insight as to what may be occurring and how long the cell can be expected to last under the conditions at which it is being cycled. In the work documented here, a variety cells are being discharged at high continuous and pulsed elevated rates. Periodically, 1C baseline procedures are run to evaluate how the cell's capacity is fading as a function of the high rate procedure being performed. More about this will be discussed in the experimental results section later.

Electrochemical Impedance Spectroscopy (EIS)

As mentioned earlier, batteries are a closed and sealed system. Thus, understanding the physical changes occurring inside the battery without cutting it apart is not entirely possible. From an electrical engineering perspective, the changes to the electrical parameters within the cell are often enough to model and design an application. EIS is one method, which can be used to help understand the electrical as well as the physical parameters changing within a cell. EIS is a non-destructive procedure in which a wide range of small amplitude, few millivolts, sinusoidal signals, across a wide frequency spectrum, typically varying from near DC to 10s of kilo Hertz, are applied to the terminals of the cell under test. The cell's response to the applied signals is recorded and the frequency dependent response provides a feedback of the systems impedance and physical structure. For example, the Nyquist plot recorded from a lead acid battery is shown in Figure 2-19. As noted on the figure, the various changes in the curve's shape reveal the effects of conductance, the effects caused by the charge transfer and the electrochemical double layer, and the effects caused my mass transport.

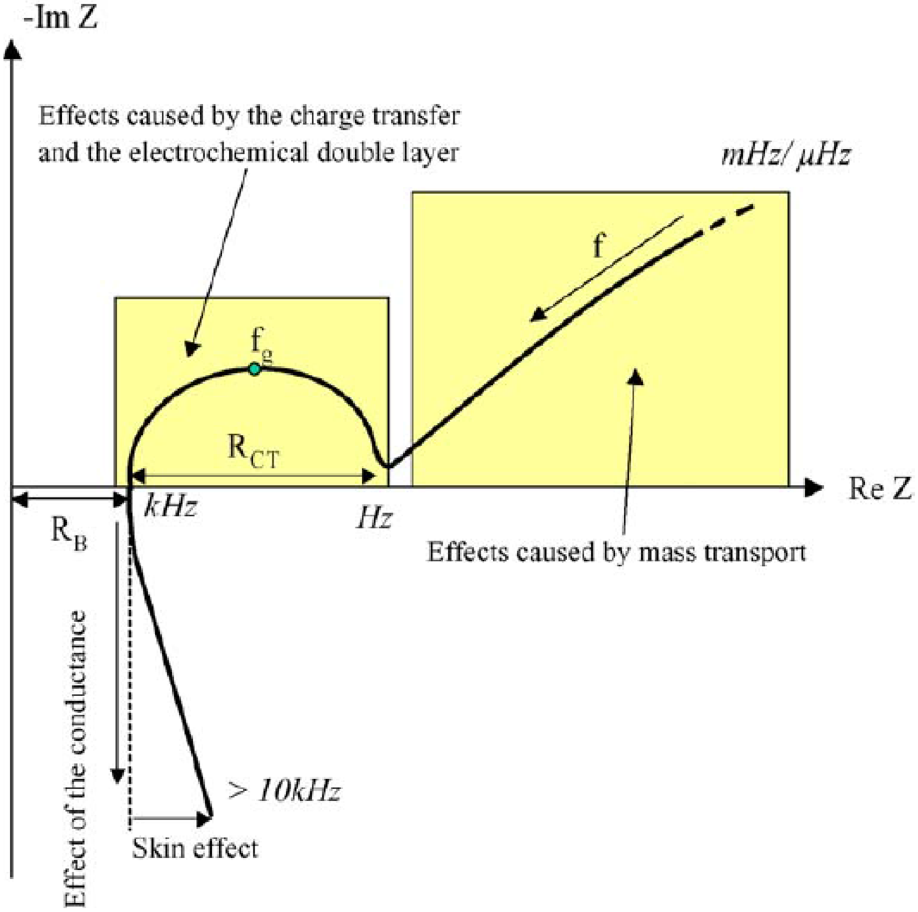

Figure 2-19 Nyquist plot for a lead acid battery

Figure 2-20 shows the Nyquist plot obtained from a lithium nickel cobalt aluminum (NCA) oxide battery. Note that there are two semicircles observed in the EIS plot compared to one semicircle observed on the lead acid battery's EIS curve above. The leftmost semicircle is known as the medium frequency semicircle representing the passive film formation on the electrodes, especially on the cathode [11]. The rightmost semicircle is known as the low frequency semicircle representing the internal charge transfer resistance (both the interfacial and surface film resistances of the cathode and anode) [11].

Nyquist plot of a battery can roughly be divided into three parts [11]. The high frequency part, with negative imaginary impedance, is caused by conductance in wires. The mid-frequency semi-circle can be related to charge transfer and the electrochemical double layer, representing the kinetics of the electrochemical battery reactions. The low frequency part, characterized by the 45° slope, is caused by limitations in mass transfer and diffusion.

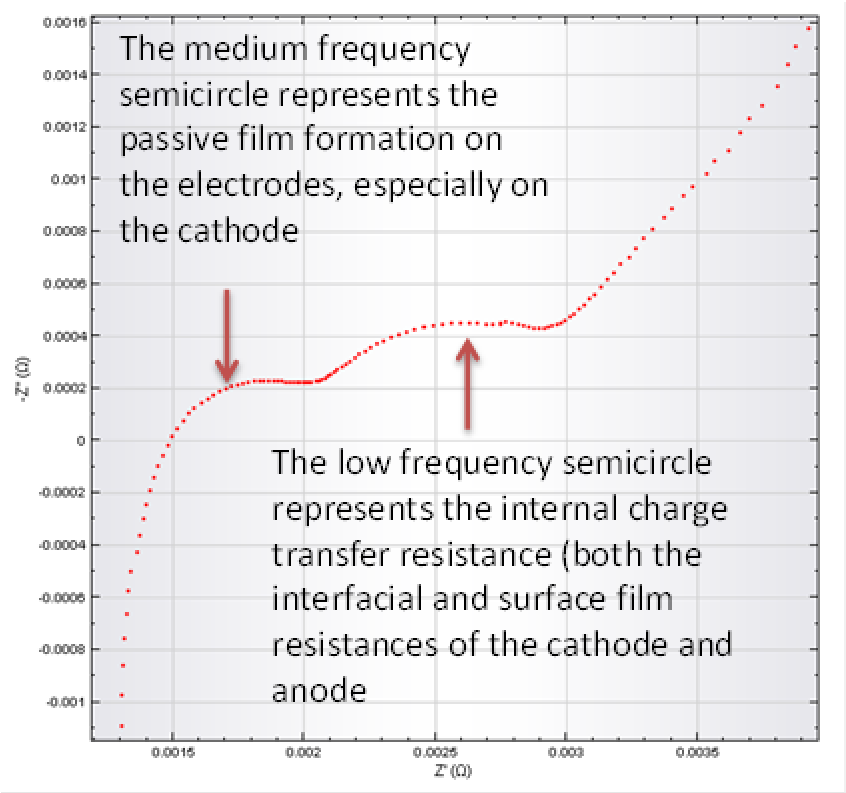

The medium frequency semicircle represents the passive film formation on the electrodes, especially on the cathode

The low frequency semicircle represents the internal charge transfer resistance (both the interfacial and surface film resistances of the cathode and anode

Figure 2-20: Nyquist plot for a lithium-ion battery

Previously Conducted Research

There have been several studies performed to understand the fundamental manner in which lithium-ion batteries age. A few of those will be highlighted in the following sections.

Pulsed Discharge of a Lithium-ion Battery

In the wide literature search performed, there were no published works found in which high C rate pulsed discharge was evaluated as a variable impacting the cycle life of lithium-ion batteries. In their work to evaluate the high discharge capability of new high power lithium-ion batteries, Chen et al. developed two versions of a novel low impedance test stand utilizing high power MOSETs. The two versions of the stand, which are shown in Figure 2-21, were designed to discharge a single cell into a controllable low-impedance load. Chen's work was focused on evaluating single high rate pulsed discharges from a cell rather than a full high rate discharge's impact on aging. Figure 2-22 shows one of Chen's single pulsed discharge waveforms recorded from a Saft VL8V into a 1.25 mΩ load. This work inspired the work being performed here, which will be discussed next.

From the experiment, it was observed that the single high power 8 Ah lithium-ion cell could be used to perform a single pulsed discharge for 5 ms and get a current of up to 1.7 kA. The work shows that a new high powered lithium-ion cell is capable of handling a high C rate pulsed discharge. However, the work done here did not focus on fully discharging the cell at high C rates and no aging studies were conducted either.

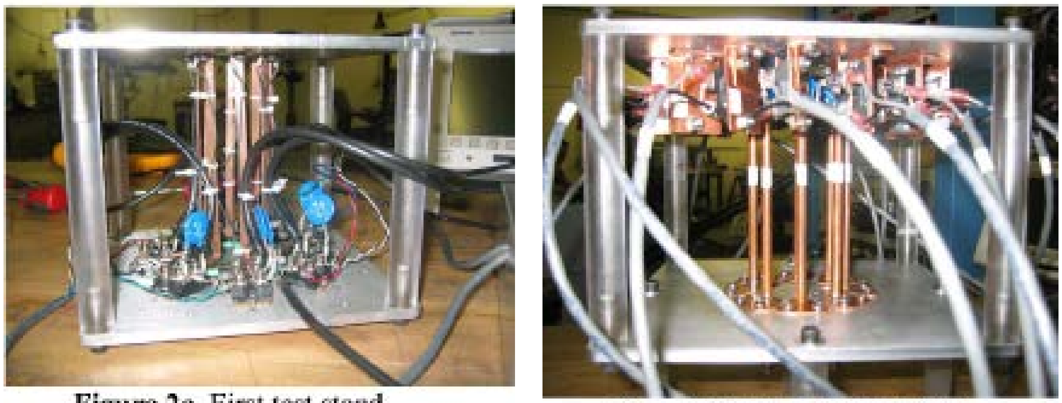

Figure 2a. First test stand. **Figure 2b.** Second test stand.

Figure 2-21 Low impedance stand for single pulsed discharge [6]

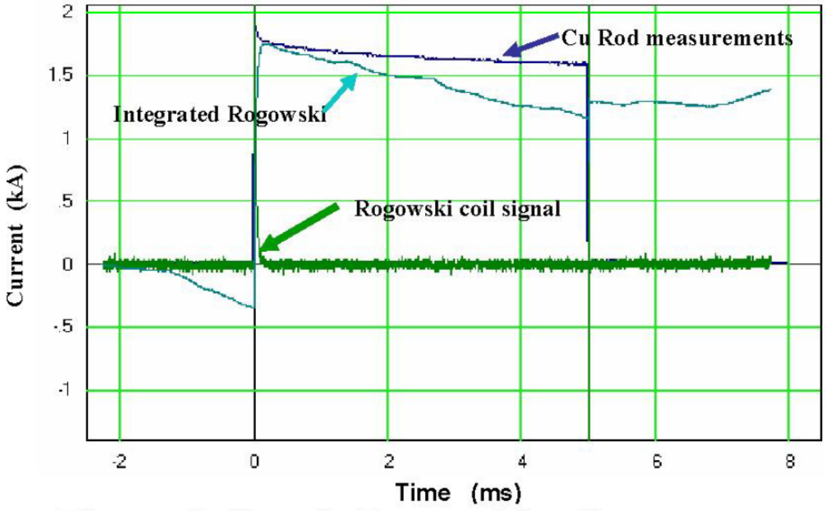

Figure 2-22 Pulsed discharge of a Saft VL8V into a 1.25 mΩ load [6]

Nominal Rate Cycling of Lithium-ion Battery

Murphy et. al. [11] performed cycle life experiments on a prismatic Sanyo UF653467 lithium-ion battery with a nominal capacity of 930 mAh. Cycling was performed using a 1C charge rate to 4.1 V, followed by 0.5 hours at open circuit, and finally 1C discharge to 3.0V. Cycling in this manner was repeated until the capacity reached 700 mAh. A curve of the battery's capacity as a function of cycle number is shown in Figure 2-23.

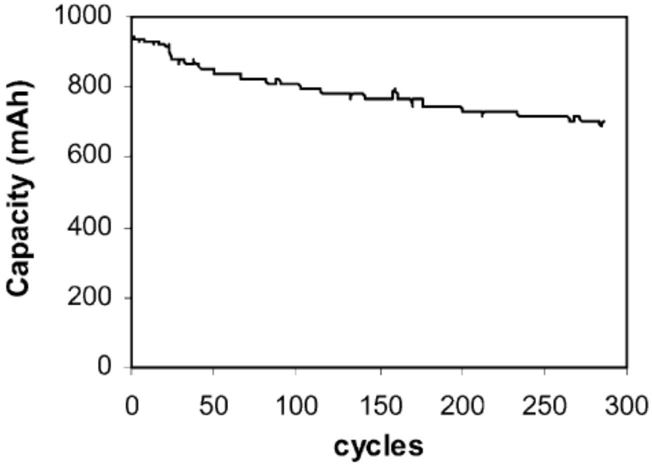

Figure 2-23 Capacity vs. cycles [11]

Murphy et. al. also obtained an EIS measurement from the cell after each cycle while it was in the discharge state. The EIS data collected after 0, 40, and 286 cycles are shown in Figure 2-24. Each of the EIS measurements were made after the cell had rested in an open circuit state for one hour, enough time for the cell to stabilize. The medium frequency semicircle is depressed and has no distinctive change with increasing cycles. The low frequency semicircle represents the internal charge transfer resistance (both the interfacial and surface film resistances of the cathode and anode) and the diameter of the low frequency semicircle is increasing with cycle life, indicating a significant increase in the total internal resistance of the cell.

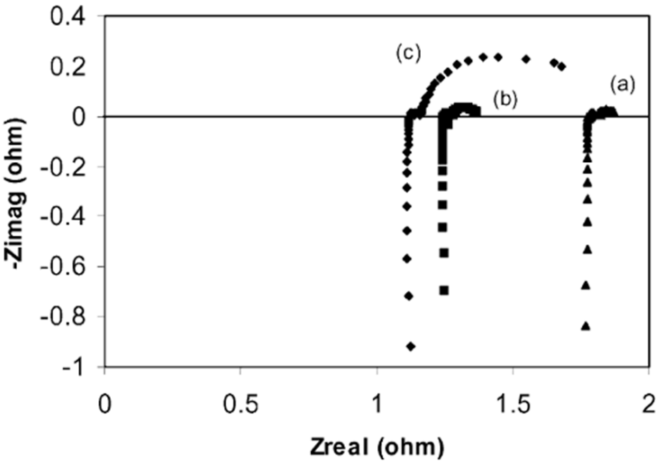

Figure 2-24 Nyquist plot from EIS measurement after a) 0 cycles, b) 40 cycles, and c) 286 cycles [11]

High Rate Discharge Cycling of a Lithium-ion Battery

Ning performed a high rate discharge cycling on Sony US 18650 Li-ion battery at ambient temperature [38]. The cycling was performed on three cells in which all of the cells were charged using a same nominal rates but each cell was discharged at different rates of 1C, 2C, and 3C, respectively. After 300 cycles, it was observed that the cell with 1C, 2C, and 3C showed a capacity loss of 9.5%, 13.2%, and 16.9% respectively. The capacities of all three cells were measured after every 50 cycles using 1A constant current discharge method. The capacity fading of three cells discharged at different rate is shown in Figure 2-25.

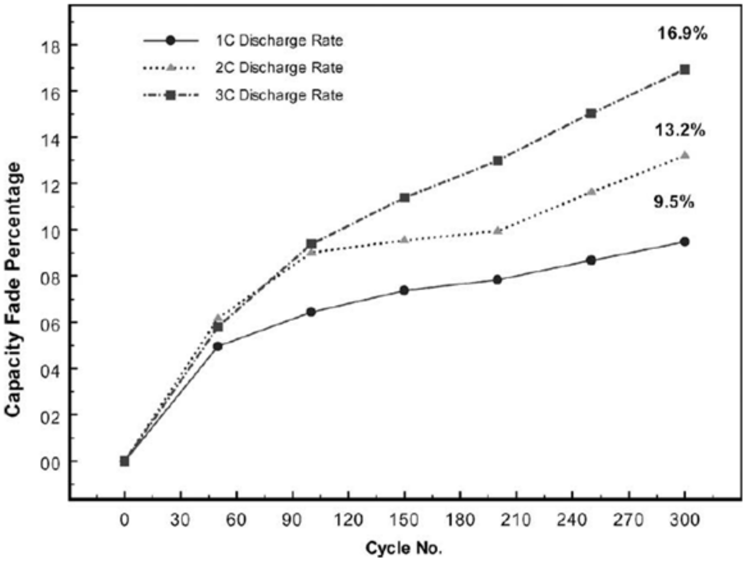

Figure 2-25: Capacity fading of cells discharged at 1C, 2C, and 3C [38].

Pulsed Discharge Cycling of a Lithium-ion Battery

Williard [36], performed a pulsed discharge test on a lithium ion battery with a discharge profile that pulsed between 1C, 0.5C, and 0C each for 30 seconds effectively giving an average discharge level of 0.5C. For comparison, other two test was performed on similar cell with a constant discharge rate of 0.5C and 1C. The capacity fade comparison between pulsed discharge, 0.5C constant rate discharge, and 1C constant rated discharge is shown in Figure 2-26. It was observed that the capacity fade of the combined current pulses degrades slower than either one of the constant discharge current profiles. Williard concluded that these phenomena could be due to the 30 second rest period that occurs between each pulse which may allow the battery to remain close to a stable electrochemical equilibrium.

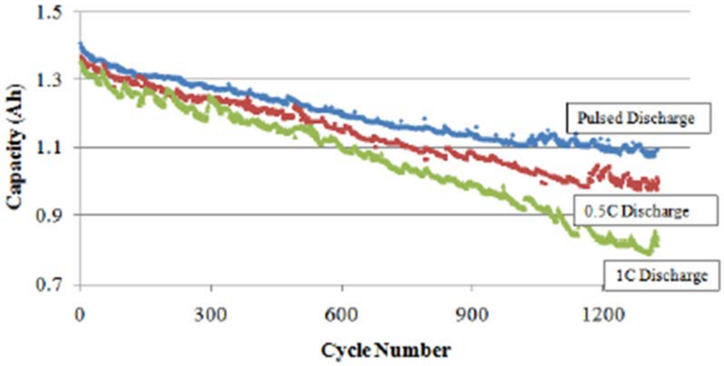

Figure 2-26: Capacity fade comparison between pulsed discharge, 0.5C discharge, 1C discharge [36]

Chapter 3

Experimental Setup

In the aging study performed here, several unique experiments were performed using two different types of experimental battery cyclers. The experiments performed will be discussed in the following sections.

Custom Built Discharge Stand

As already mentioned in the introduction, an experimental test stand, similar to that of Chen, et. al. [6], has been developed and fabricated so that electrochemical energy storage devices can be pulse discharged at elevated rates well in excess of their rated C value. The stand can conduct peak pulsed currents of 10 kA, and has the flexibility to vary the load’s series inductance and resistance. A CAD model of the stand is shown in Figure 3-1 and a photograph of the constructed stand is shown in Figure 3-2. The primary difference between this stand and that of Chen’s is the electrical action capability, which thermally limited the earlier test stand to handle single pulse discharges, and the variability of the stand’s resistance and inductance. An altered configuration of the stand, which will not be discussed in detail here, is being using to recharge the same types of electrochemical energy storage devices at high pulsed rates [7].

The cell under test is housed in a thick walled stainless steel chamber to ensure that any thermal runaway events are safely contained. The positive terminal of the cell is oriented downward and is connected directly to a 1.58 cm diameter C11000 copper rod, which is one of four conductors that makes up the variable inductor. The variable inductor is essentially a two turn inductor that is varied by adjusting the vertical location of two saddle clamp conductors over the conductor length of 0.1 m to 1.5 m, providing a circuit inductance range of 0.1 μH to 2.3 μH and resistance of 10 μΩ to 425 μΩ when copper rods are used. Alternative materials, such as steel or aluminum, can be used to increase the adjustable resistance while not changing the inductance range. The output of the inductor is terminated into the aluminum plate located below the cell. From the lower aluminum plate, the current is fed into a total of sixty Semikron SKM111AR MOSFET modules that are all connected in parallel. The sixty MOSFETs are grouped in six sets of ten, and each set feeds current into its own 2.54 cm diameter C11000 copper bus bar that conducts the current into the aluminum bus plate above the cell. The center of the upper plate has a circular cutout in it that is big enough to remove the steel chamber. This cutout breaks the electrical path back to the cell. In order to reclose the circuit, a circular disk of aluminum that is larger than the cutout, as well as a 2.54 cm diameter stock of copper that extends upwards from negative terminal of the battery, is firmly pressed against the upper aluminum plate as well, using four hold down clamps. This portion incorporates the second safety feature of the test stand. The circular disk of aluminum is connected to two vertical springs that pull the disk upwards breaking electrical contact if it is not held down with the clamps. Four electrically activated solenoids are used to mechanically pull back the clamps, thus allowing the upper aluminum disk to rise and break the circuit in the event of thermal runaway. From the center aluminum disk, the current is fed through a ~48.9 μΩ custom made current viewing resistor (CVR), and finally back to the negative terminal of the battery. The size of all of the bus bars as well as the number of MOSFETs, were chosen to both increase the electrical action capability of the stand as well as reduce the series resistance of the stand to a low enough value, so that in most cases the cell's ESR is the dominating impedance of the circuit. Each SKM111AR module has a nominal on-state resistance of roughly 8 mΩ, giving a parallel on-state impedance as low as 150 μΩ when all sixty are conducting. An equivalent circuit schematic of the stand is shown in Figure 3-3.

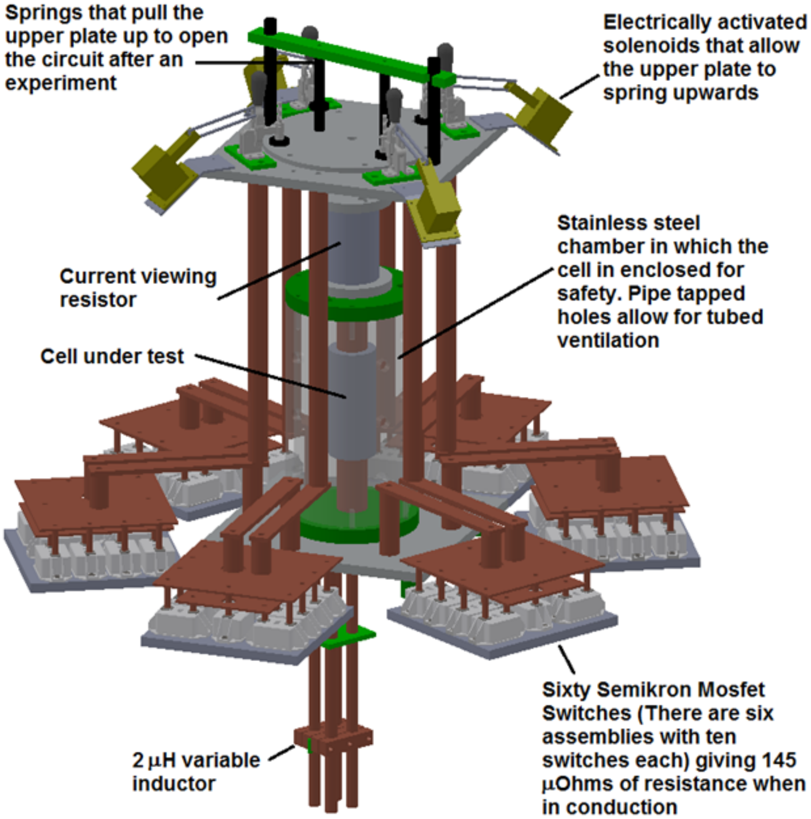

Figure 3-1 CAD model of a stand in discharge configuration

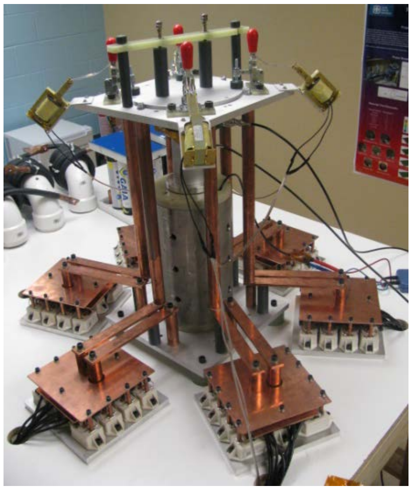

Figure 3-2 Photograph of the constructed test stand

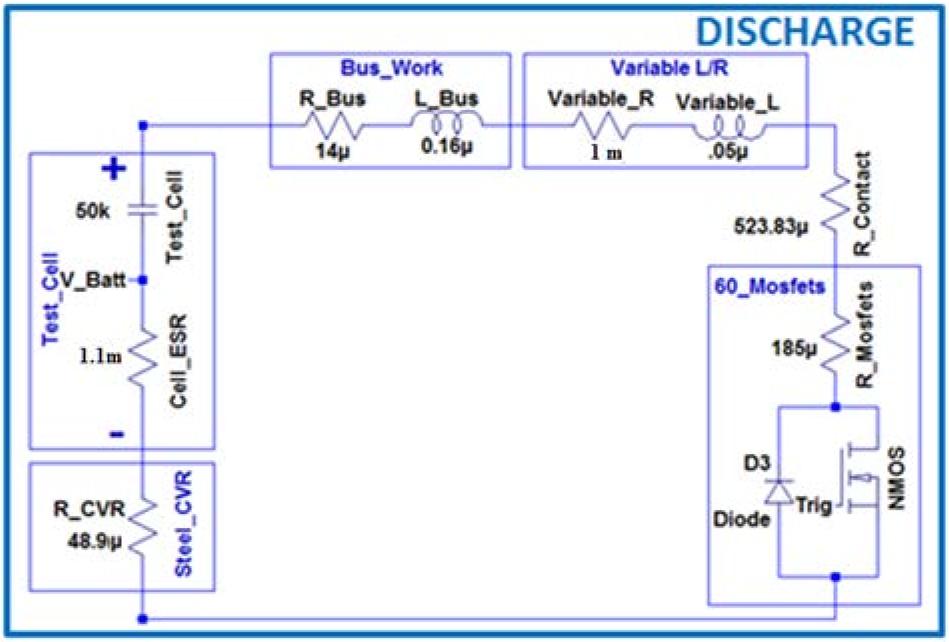

Figure 3-3 Equivalent circuit diagram of stand in discharge configuration

In order to monitor the voltage across the cell and the MOSFETs, three Fluke high voltage differential probes are used. The voltage across the CVR is monitored and used to back out the current that is extracted from the cell. As a backup measurement, a Rogowski coil made by Power Electronic Measurements Ltd. is used. All of these measurements are made using a National Instruments PXI-e chassis equipped with PXIe-6361 differential voltage acquisition cards. Because the I^2R losses are quite high and the temperature rise of the cell is a key parameter regarding its performance and aging mechanisms, a 0.076 mm K-type thermocouple is attached to the cell and monitored using a 16 channel NI-9213 thermocouple module in an NI CompactDAQ data acquisition system (CDAQ). The NI-9213 is a multiplexed device capable of sampling at a rate of 1200 samples per second.

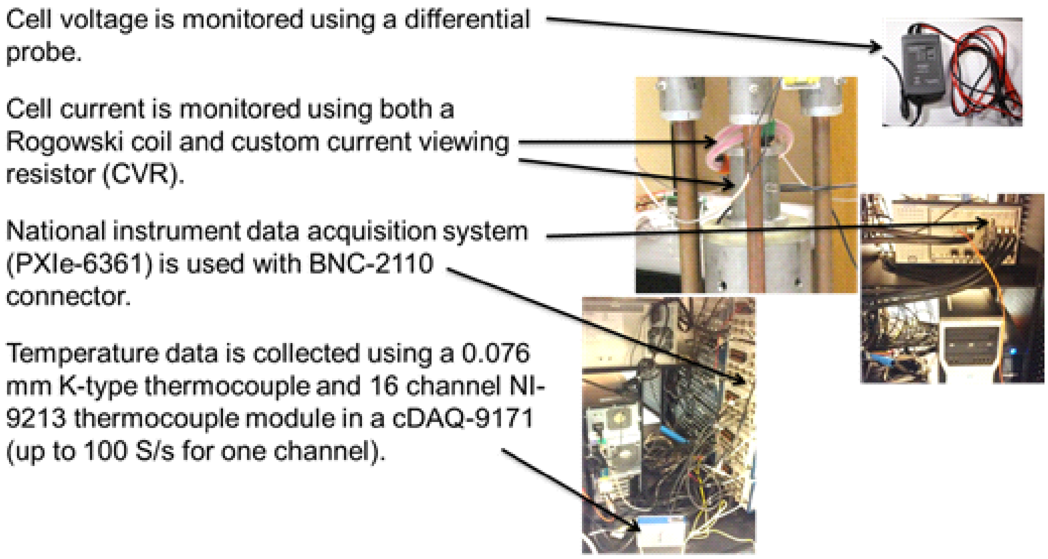
Cell voltage is monitored using a differential probe.

Cell current is monitored using both a Rogowski coil and custom current viewing resistor (CVR).

National instrument data acquisition system (PXIe-6361) is used with BNC-2110 connector.

Temperature data is collected using a 0.076 mm K-type thermocouple and 16 channel NI-9213 thermocouple module in a cDAQ-9171 (up to 100 S/s for one channel).

Figure 3-4: Data acquisition system

MACCOR System

In addition to the custom made test stand, a 4000 series battery cycler manufactured by Maccor Incorporated, shown in Figure 3-5, is also used in the work performed here. The cycler offers five simultaneous channels which can charge and discharge cells at potentials between 0 V and 5 V with current rates as high as 240 A per channel. When operated in that range the cycler has a measurement accuracy of ±125 mA and ±2 mV. In addition, the cycler has two channels which can be used to charge and discharge cells/modules at potentials between 0 V and 60 V with currents as high as 100 A per channel. The cycler also offers four digital input/output channels for communication with other experimental hardware, as well as thirty two Type T thermocouple inputs for real time thermal monitoring. Though not used in any of the work performed here, two thermal chambers are also available for use. One is an ESPEC BTZ-133 with a usable space of 1.5 ft^3 and the other is a BTX-475 with a usable space of 4.5 ft^3. Both operate over a temperature range of -70^oC to 180^oC.

Figure 3-5: Maccor inc. 4000 series battery cycler

Potentiostat

All of the EIS measurements are made using a MetrOhm PGSTAT 302N/FRA and 20 A current booster, shown in Figure 3-6. As explained earlier, EIS is a method whereby the frequency dependent impedance of the closed battery system can be determined by measuring it's response to the application of a sinusoid with a magnitude in the few mV range across a wide frequency spectrum. This measurement has been reported on by a wide number of authors as a type of in-situ technique that can be used to hypothesize what may be occurring within a battery's bulk materials and interface layers [4][5][11]. Despite widespread use, to date there have been no concrete breakthroughs that enable EIS to absolutely define what is occurring inside the cell. Regardless, EIS remains as one of the best techniques available to produce qualitative data. Due to the non-invasive nature of this measurement technique, evaluation of the periodic changes measured is used to gauge the impact each elevated rate procedure has on the aging of the cell. The current booster is needed to ensure enough current is available when low impedance cells are tested. In a typical EIS measurement, a frequency varying sinusoid with an amplitude between 1 mV and 10 mV is applied to the terminals of the cell under test. When cells with an ESR in the 10's of mΩ are tested, currents on the order of 1 A are required from the potentiostat. Therefore, when the high power cells being considered here are used, having ESR values as low as 300 μΩ, currents on the order of 17 A are required if a 5 mV signal is applied. Because of this, a current booster is required to ensure adequate measurements can be made.

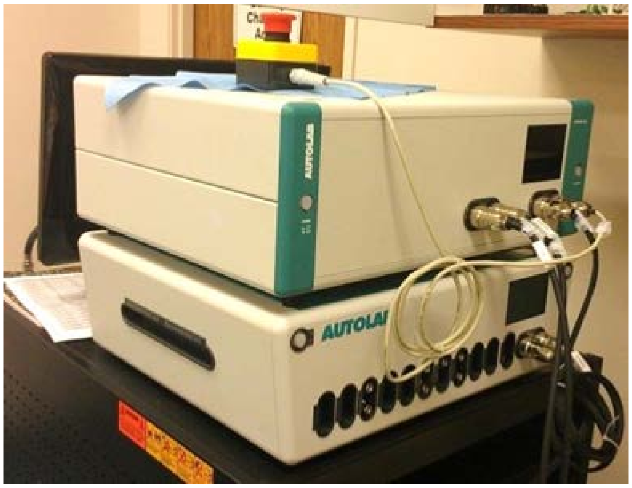

Figure 3-6: Metrohm PGSTAT 302N/FRA potentiostat with 20 A current booster

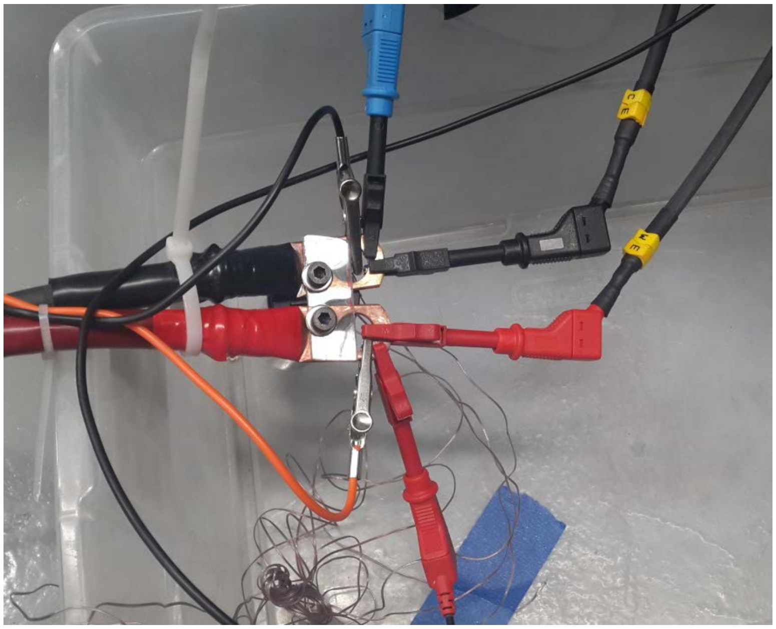

Figure 3-7: Potentiostat connected to the terminal of the cell

Test Setup

When the stand is used, the cell is enclosed in a steel chamber to ensure safe operation can be maintained at high rates. When using the Maccor cycler, it was thought that enclosing each of the seven possible cells under test in its own steel chamber would not be cost effective. As a means to provide both safety and ease of operation, custom rolling experimental platforms were made for each of the seven channels. Each platform, seen in Figure 3-8, was outfitted with quick disconnect ports for the cycler’s sense voltage leads, high current cables, and thermocouple. The high current connections are made using SB-350 gray connectors. Each cell is placed in a passive thermal isolation cooler on top of each platform. This was done for both safety and to maintain a steady ambient temperature around each cell.

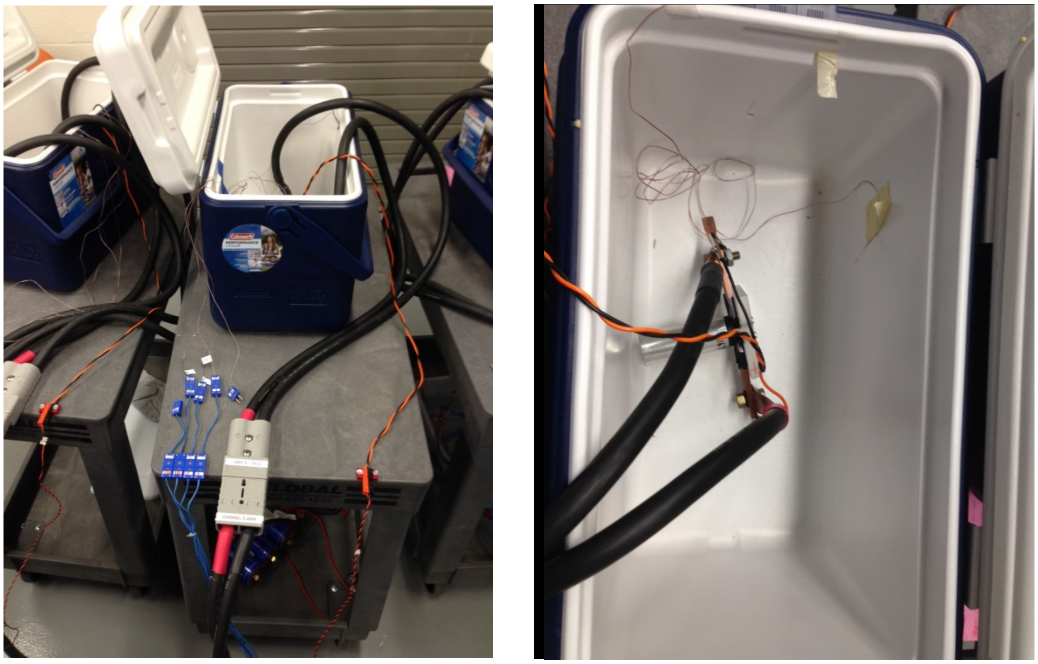

Figure 3-8: Experimental setups in a utility cart with quick connect/disconnect

Chapter 4

Experimental Results and Analysis

While the primary results to be discussed here involve the high rate testing of three 3 Ah NCA lithium-ion batteries, other tests were also performed early on in the stand's development to understand the capabilities of these new high power cells, to commission the test stand, and to develop the correct experimental procedures. A few of those experiments, as well as those conducted on the three NCA cells, will be discussed now.

Single Pulse Discharge Characterization

Using the custom built test stand discussed previously, several different types of cells were pulsed discharged for 100ms to understand the capability of each type of cell as well as characterize their ESR. The results display the wide range of energy and power densities available from today's high power energy storage devices. Fifteen different cells, listed in Table 4-1, have been pulsed discharged for 100 ms using the test stand, which acts as a roughly 0.26 mΩ to 1.07 mΩ load, depending on the contact resistance which varies from cell to cell. The measured conduction current and voltage from each cell tested is shown in

Figure 4-1 and Figure 4-2 respectively. It is important to note that each cell possesses uniquely impressive properties and capabilities. The intent of these experiments is to measure cell ESR values at high conduction rate and to measure the power densities available from the vastly different types of cells in a single pulsed discharge of 100ms pulse width.

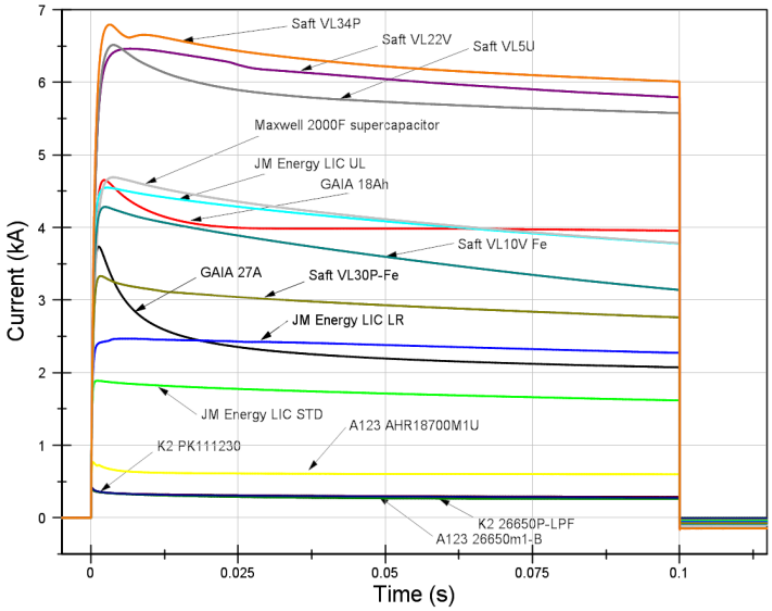

Figure 4-1 : Current measured during each 100 ms discharge.

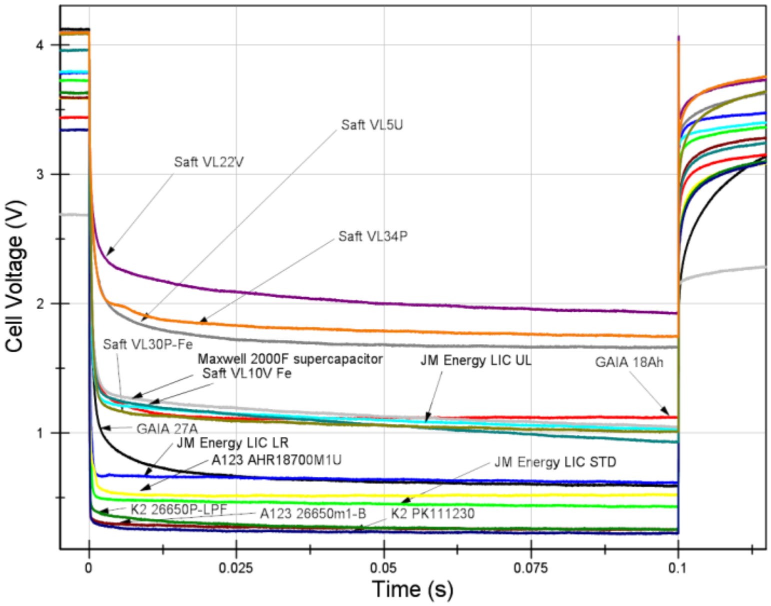

Figure 4-2: Voltage measured during each 100 ms discharge.

In the Figure 4-1, it can be seen that the conduction current for the Saft VL34P is the highest with a peak current of 6.75 kA and the conduction voltage of the Saft VL22V is the highest with approximately 2.08V. The power sourced from the cell and dissipated across the impedance of the stand, is calculated by multiplying the conduction voltage and current, is plotted in Figure 4-3. Powers in excess of 10 kW are sourced by the Saft VL22V, Saft VL34P, and SaftVL5U. A calibrated Rogowski coil manufactured by PEM UK Ltd. is used to measure the cell current.

Initially the reader may look at the data presented in Figure 4-1 and Figure 4-2, and make the wrong initial assumptions about the cells due to the wide differences between the lowest and highest conduction currents and voltages. Along with the measured data, it is important for future designers to consider the cell cost, lifetime, capacity, and mass when designing a prime power source.

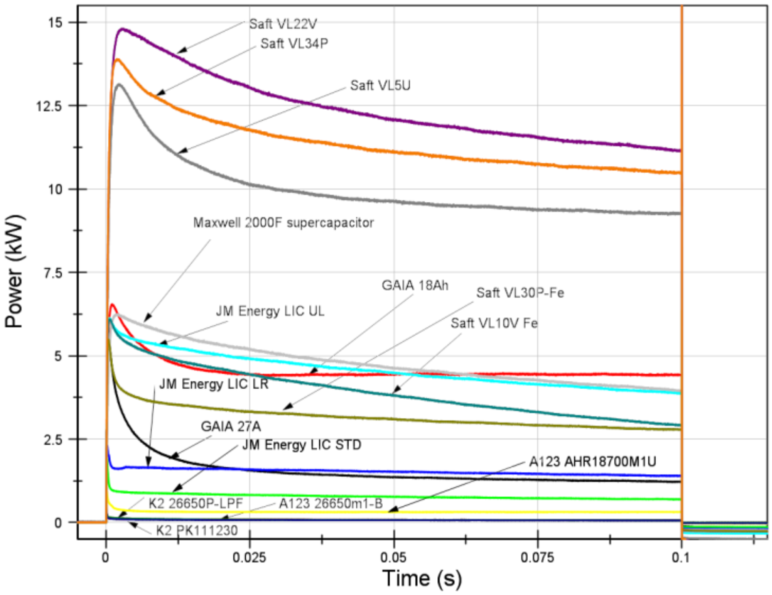

Figure 4-3: Power sourced by the cell and dissipated across the stand impedance during each 100ms discharge.

The cells' capacity and mass are interrelated properties since increasing the cell capacity requires it to have a larger electrode surface area. Since EDLCs and LICs are being plotted alongside LIBs, normalization with respect to capacity is not really a valid comparison. It is also important to remember that like ELDCs and LICs, LIBs also have an electric-double-layer capacitance component that contributes to their current and power capabilities. Larger electrodes result in higher capacity batteries, which increases the double-layer capacitance. This property contributes significantly to their higher current and power sourcing capabilities. For those reasons, the current and power curves have been normalized with respect to cell mass. These new curves are plotted in Figure 4-4 and Figure 4-5 respectively.

In the new plots, the Saft VL5U has the highest steady state gravimetric current density and highest gravimetric power density. Keep in mind that the data plotted is from the original version of the Saft VL5U and not their newer low temperature version known as the VL5U-LT [8]. The JM Energy Ultra Low (UL) resistance LIC displays a gravimetric current density that is 50% larger than the 2000 F Maxwell EDLC and a power density that is roughly 30% higher. These results show that there is no single cell that is ideal in every category, thus researchers must consider all of the different properties when choosing a particular cell or technology. The difference becomes slightly clearer when the data is compared in the different Ragone charts seen in Figure 4-8 through Figure 4-10.

Figure 4-6 plots the energy density that each manufacturer lists on their cell data sheet when the cell is discharged at its rated C value versus the power density obtained experimentally. Keep in mind that this energy density is almost certainly less than the energy density that would be obtained if the cell is repeatedly pulsed or continuously discharged at these elevated rates. Though it is hard to imagine that weight is not an issue, in the extremely rare case it isn’t, the raw energy stored value listed on the data sheet is plotted versus the experimentally obtained power in Figure 4-7. The conduction voltages versus the conduction currents are plotted in Figure 4-8.

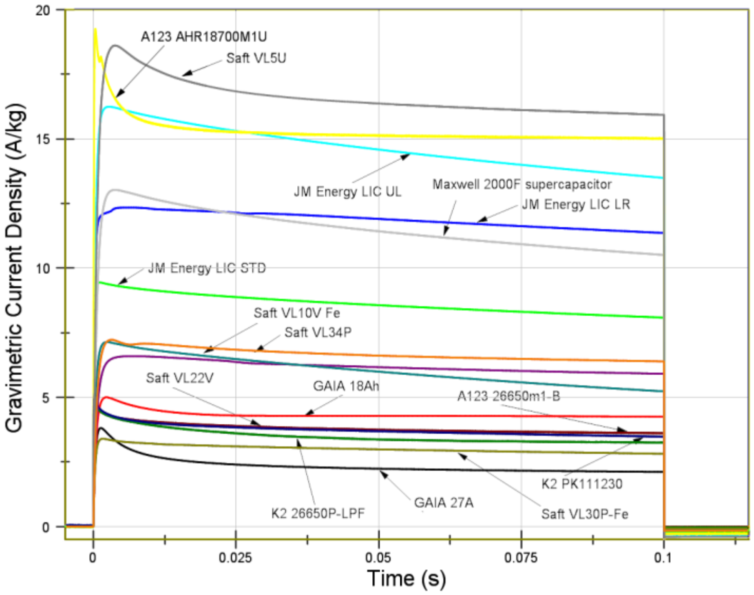

Figure 4-4. Gravimetric current density.

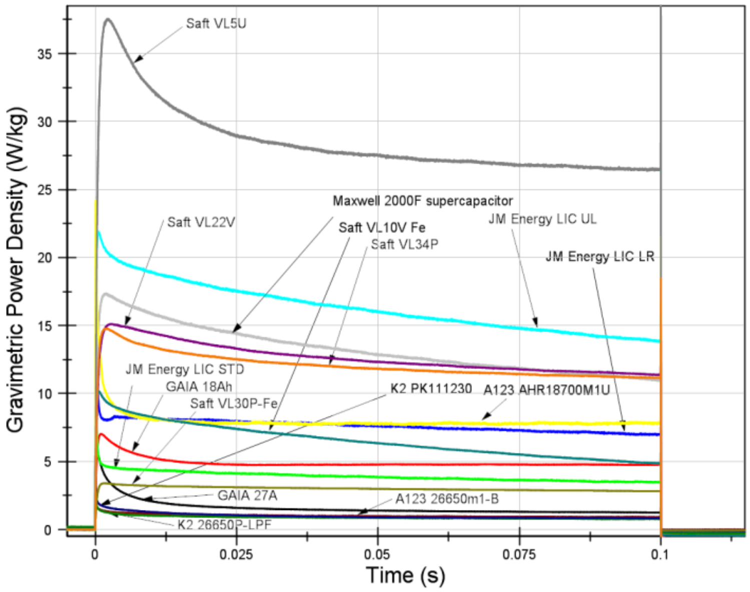

Figure 4-5. Gravimetric power density.

The cells conduction ESR versus the raw cell power is plotted in Figure 4-9 and Figure 4-10. The reason for two plots is due to the wide difference between the smaller and larger capacity cells. All of the results presented are provided in Table 4-1. Notice that when almost all of the cells were tested, the load resistance was roughly 300 µΩ with the only exceptions being the smaller 26650 and 18700 cylindrical cells, which connect to the stand in a very different manner than the large format cells. It is also worth noting that in most cases, this low impedance does not result in the maximum achievable power from the cells. The maximum power would be achieved when the load resistance is equivalent to that of the source impedance and can be easily calculated using the data presented here. In many instances, the power delivered from the cells is higher in earlier published data where the contact impedance of the stand was higher [18]. The experiments presented here were aimed at showing the peak pulsed currents and conduction voltages that could be obtained from these cells into an extremely low impedance load.

Though not factored into the gravimetric plots seen earlier, it is also important to take into account the mass of the containment in which the different cells are housed. Where available, the masses of the cell containments are listed in Table 4-1 under the header *Cont. Mass*. Some cells possess heavy military grade housing, while other cells have thin aluminum pouches. If high currents are not needed, and therefore high electromagnetic forces do not need to be contained, researchers may be able to work with manufacturers to reduce containment mass to make a particular cell more applicable.

Table 4-1: Tabular form of the experimental results from the 100ms pulsed discharge experiment

Storage Device	**Mass (kg)**	**Cont Mass (kg)**	**ESR (mΩ)**	**Initial Cell Voltage (V)**	**Cond. Voltage (V)**	**Cond. Current (kA)**	**Load Imp. (mΩ)**	**D.S. Energy (Wh)**	**Cond. Pwr. (kW)**	**D.S. Energy Density (Wh/kg)**	**Cond. Pwr. Density (kW/kg)**
GAIA 27 Ah $LiNi_xCo_{1-x}O_2$ LIB [9]	0.939	0.318	1.42	4.10	0.69	2.40	0.29	97.02	1.66	103.32	1.76
GAIA 18 Ah $LiFePO_4$ LIB [9]	0.918	0.318	0.58	3.44	1.12	4.02	0.28	57.66	4.50	62.81	4.90
Saft 10 Ah $LiFePO_4$ LIB (Super-Phosphate™ VL10VFe) [16]	0.603	N/A	0.70	3.94	1.17	3.94	0.30	33.00	4.61	54.73	7.64
Saft 22 Ah $LiNi_xCo_yAl_{1-x-y}O_2$ LIB (VL22V) [16]	0.934	N/A	0.32	4.10	2.08	6.31	0.33	84.00	13.12	89.94	14.05
Saft 34 Ah $LiNi_xCo_yAl_{1-x-y}O_2$ LIB (VL34P) [16]	0.904	N/A	0.35	4.09	1.84	6.50	0.28	120.00	11.96	132.74	13.23
Saft 30 Ah $LiFePO_4$ LIB (Super-Phosphate™ VL30PFe) [16]	0.926	N/A	0.97	4.07	1.11	3.06	0.36	99.00	3.40	106.91	3.67
Saft 5Ah LiNixCoyAl1-x-yO2 LIB (VL5U)	0.350	N/A	0.38	4.05	1.77	6.03	0.29	18.25	10.67	52.14	30.49
2200 F Laminate LIC (STD) [29]	0.214	0.021	1.82	3.72	0.46	1.79	0.26	3.00	0.82	14.00	3.85
2200F Laminate LIC (LR) [29]	0.265	0.021	1.28	3.78	0.65	2.44	0.27	2.92	1.59	11.00	5.98
2200F Laminate LIC (ULR) [29]	0.278	0.021	0.61	3.79	1.16	4.32	0.27	2.78	5.01	10.00	18.03
2000 F Maxwell EDLC [28]	0.414	0.059	0.34	2.68	1.20	4.40	0.27	2.03	5.28	4.90	12.75
K2 Energy 2.6 Ah $LiFePO_4$ LIB (LPF26650P) [15]	0.081	0.018	11.45	3.63	0.31	0.29	1.07	8.32	0.09	102.72	1.11
K2 Energy 2.6 Ah $LiFePO_4$ LIB (PK111230-2, 26650) [15]	0.083	0.018	11.37	3.30	0.23	0.27	0.85	8.32	0.06	100.24	0.75
A123 Systems 2.5 Ah $LiFePO_4$ LIB (26650m1-B Nanophosphate®) [56]	0.072	0.009	10.34	3.60	0.29	0.32	0.91	8.25	0.09	114.58	1.29
A123 Systems 0.7 Ah Ah $LiFePO_4$ LIB (AHR18700M1Ultra Nanophosphate®) [1]	0.038	0.009	5.11	3.60	0.48	0.61	0.79	2.31	0.29	60.79	7.71

Table Abbreviations – Cont. = Containment, Cond. = Conduction, Imp. = Impedance, D.S. = Data Sheet, Pwr.= Power

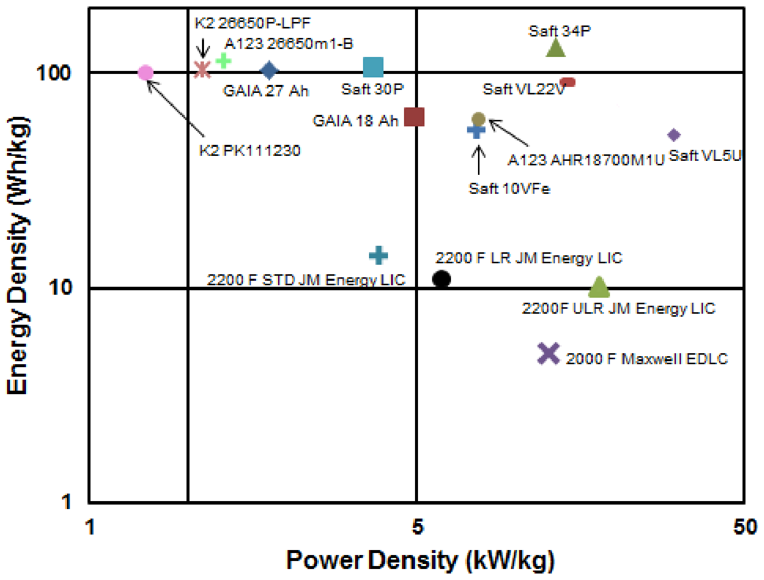

Figure 4-6. Manufacturer's 1C rate data sheet energy density versus experimentally obtained 100 ms power density.

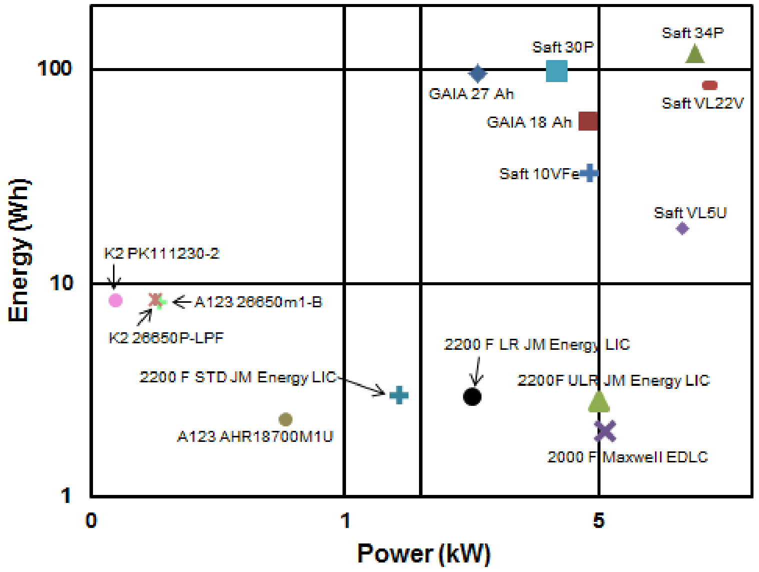

Figure 4-7. Rated data sheet stored energy versus experimentally obtained 100 ms power.

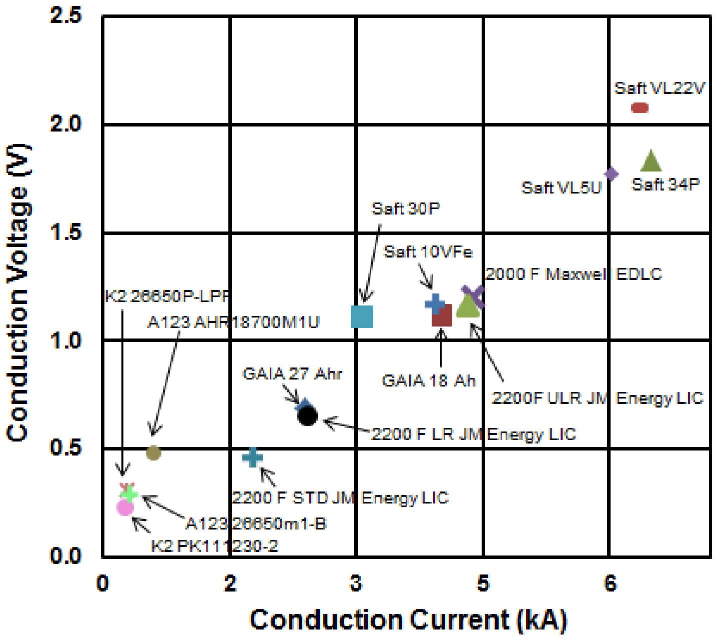

Figure 4-8. Conduction voltage versus conduction current recorded during the 100 ms pulsed discharge of each cell.

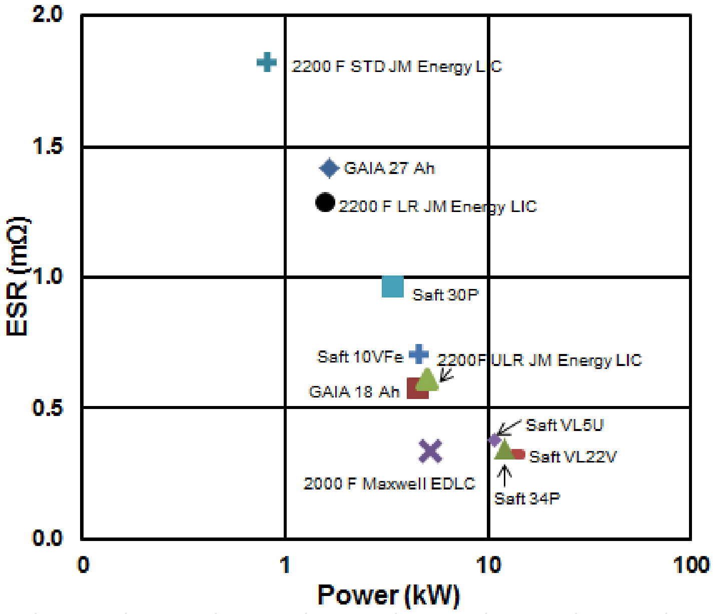

Figure 4-9: ESR value calculated when the cell is discharged for 100ms.

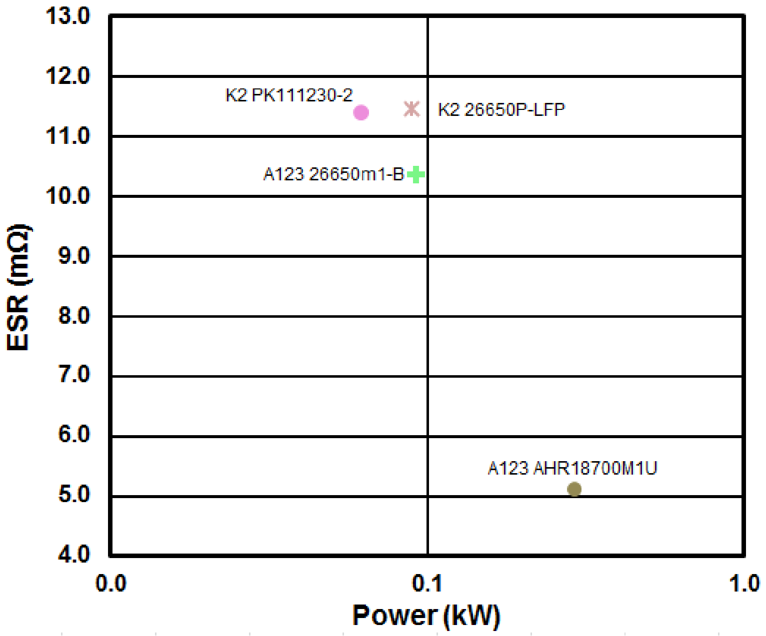

Figure 4-10: ESR value calculated when each cell is discharged for 100ms.

Aging of Two 26650 - 2.6 Ah $LiFePO_4$ Lithium-Ion Batteries

In the experiments discussed here, two identical 2.6 Ah LiFePO4 batteries manufactured by K2 Energy have been cycled to understand the impact current rate as well as the DoD on the cycle life of the cells. A photograph of the cell along with a listing of its datasheet properties are shown in Figure 4-11 and Table 4-2 respectively. During discharge, both of the cells have been discharged using the Maccor cycler at 28 A (11 C) in a pulsed manner with 5 s of continuous conduction followed by 1 s of rest. This pulsed discharge operation is repeated until the cell voltage decreases to the experiment's lower defined voltage minimum. One of the cells was cycled with a minimum voltage of 2.0 V, which is the absolute safe minimum voltage of the cell, while the other was cycled to 2.5 V, the manufacturers recommended discharge voltage. Both cells were recharged using a 9A CC procedure till the voltage reached 3.65 V after which a CV procedure was in place till the current decreased below 0.1 A. During a first fifty cycles, a baseline procedure was performed after every ten cycles. After the completion of fifty cycles, the baseline procedure was repeated after every fifty subsequent cycles. During the baseline procedure, each cell is cycled using a 1C CC - CV charge and discharge procedure in order to measure the capacity fade of each respective cell as a function of cycle number. The 1C CC-CV charge/discharge procedure is used to ensure each of the two cells are being compared using a fair metric. Also as part of the baseline procedure, electrochemical impedance spectroscopy (EIS) measurements are made for use in hypothesizing what may be occurring inside the cells. The experimental procedure is highlighted graphically in Figure 4-12 to Figure 4-15.

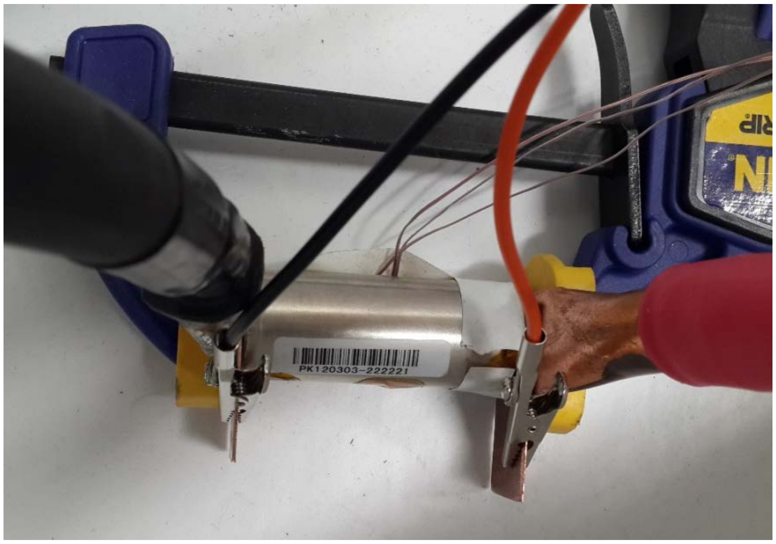

Figure 4-11: K2 26650 form $LiFePO_4$ battery

Table 4-2: Datasheet properties for K2 26650 form $LiFePO_4$ battery

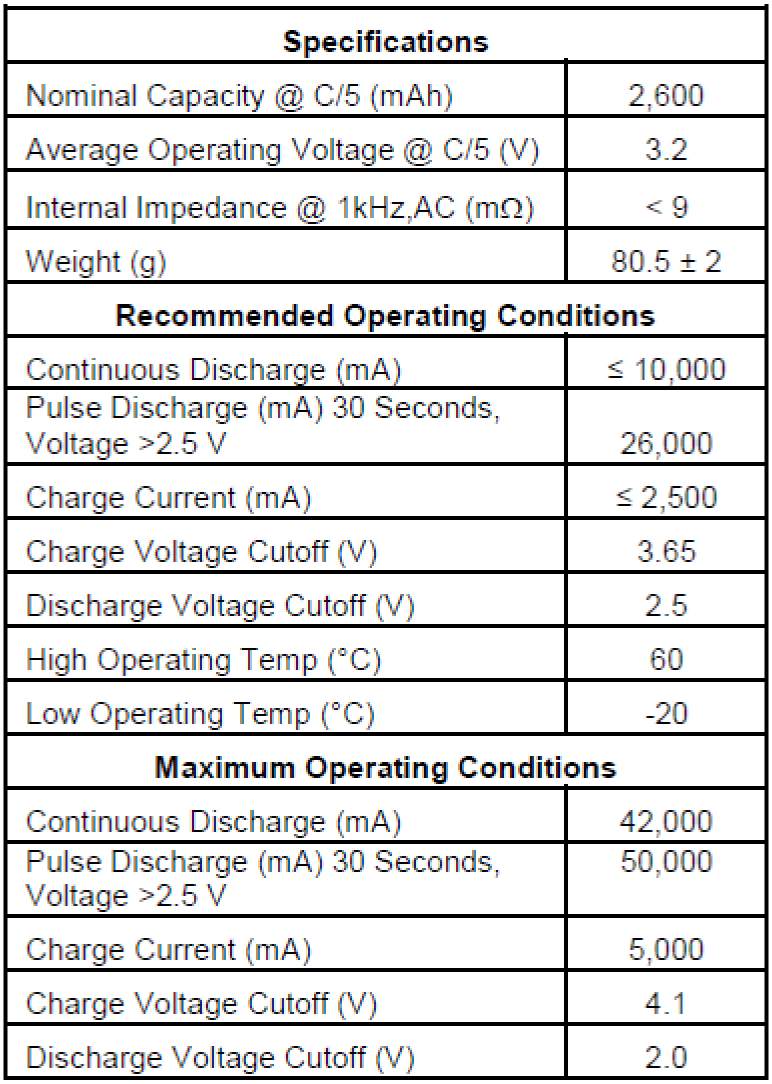

Specifications	
Nominal Capacity @ C/5 (mAh)	2,600
Average Operating Voltage @ C/5 (V)	3.2
Internal Impedance @ 1kHz,AC (mΩ)	< 9
Weight (g)	80.5 ± 2
Recommended Operating Conditions	
Continuous Discharge (mA)	≤ 10,000
Pulse Discharge (mA) 30 Seconds, Voltage >2.5 V	26,000
Charge Current (mA)	≤ 2,500
Charge Voltage Cutoff (V)	3.65
Discharge Voltage Cutoff (V)	2.5
High Operating Temp (°C)	60
Low Operating Temp (°C)	-20
Maximum Operating Conditions	
Continuous Discharge (mA)	42,000
Pulse Discharge (mA) 30 Seconds, Voltage >2.5 V	50,000
Charge Current (mA)	5,000
Charge Voltage Cutoff (V)	4.1
Discharge Voltage Cutoff (V)	2.0

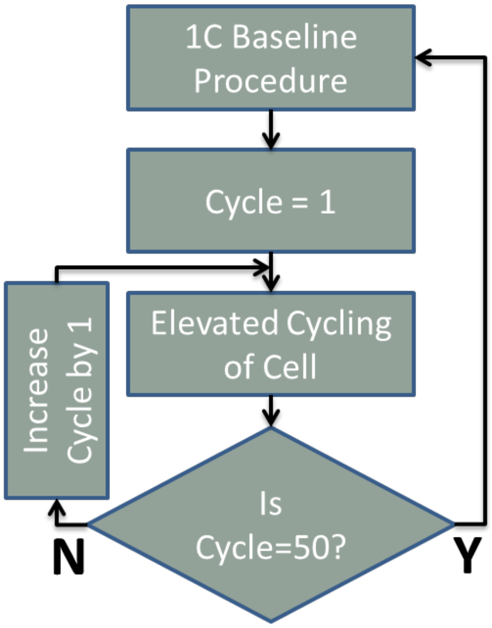

Figure 4-12: Elevated rate cycling

In Figure 4-12, the elevated rate cycling procedure is shown. In the two tests performed, all the test procedures and parameters are kept the same except for the lower discharge voltage during elevated cycling of the cell. The elevated rate discharge procedure used in the cycling of the cell down to 2.5 V is given in Figure 4-13 while that for the one cycled down to 2.0 V is given in Figure 4-14. Figure 4-15 displays the baseline procedure which is used in the periodic evaluation of each of the two cells. The current and voltage profile obtained from the elevated cycling procedure are shown in Figure 4 16 to Figure 4 19.

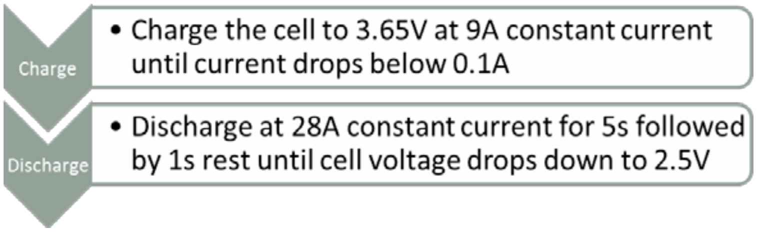

- Charge the cell to 3.65V at 9A constant current until current drops below 0.1A
- Discharge at 28A constant current for 5s followed by 1s rest until cell voltage drops down to 2.5V

Figure 4-13: Elevated cycling of cell procedure for cell discharged to 2.5 V

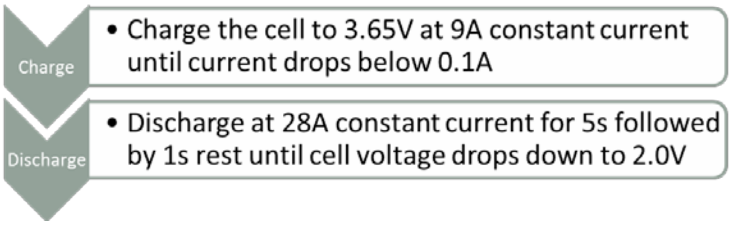

Figure 4-14: Elevated cycling of cell procedure for cell discharged to 2.0 V

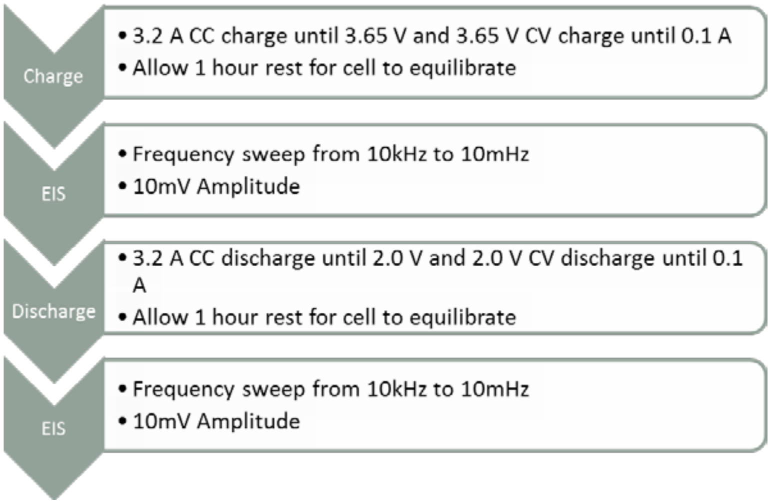

Figure 4-15: 1C baseline procedure

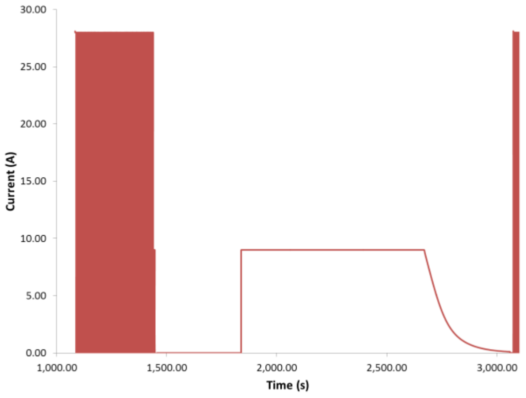

Figure 4-16: Current waveforms recorded during one complete 28 A elevated pulsed discharge cycle, between 1,100 s and 1,500 s and 9 A CC-CV charge, between 1,850 s and 3,000 s. This experiment was performed on the cell discharged to 2.0 V.

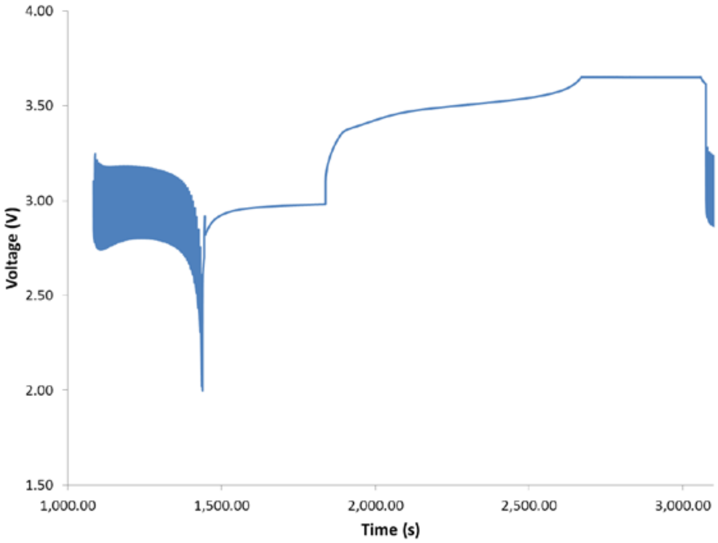

Figure 4-17: Voltage waveforms recorded during one complete 28 A elevated pulsed discharge cycle, between 1,100 s and 1,500 s and 9 A CC-CV charge, between 1,850 s and 3,000 s. This experiment was performed on the cell discharged to 2.0 V.

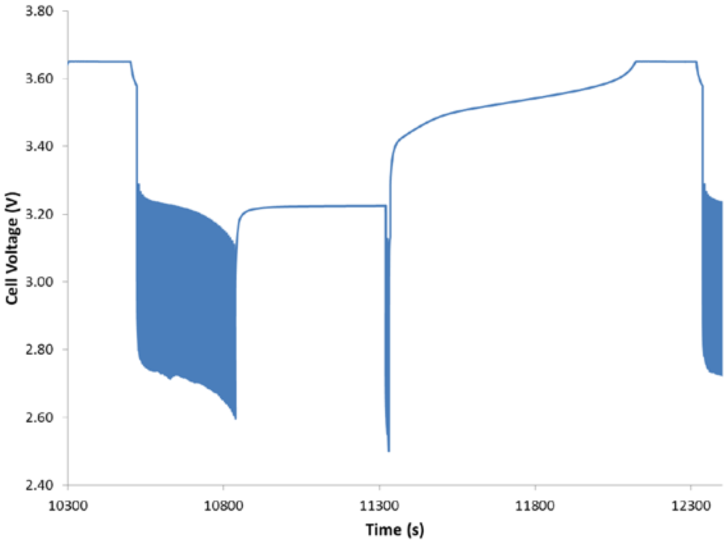

Figure 4-18: Voltage waveforms recorded during one complete 28 A elevated pulsed discharge cycle, between 10,300 s and 10,900 s and 9 A CC-CV charge, between 11,300 s and 12,300 s. This experiment was performed on the cell discharged to 2.0 V.

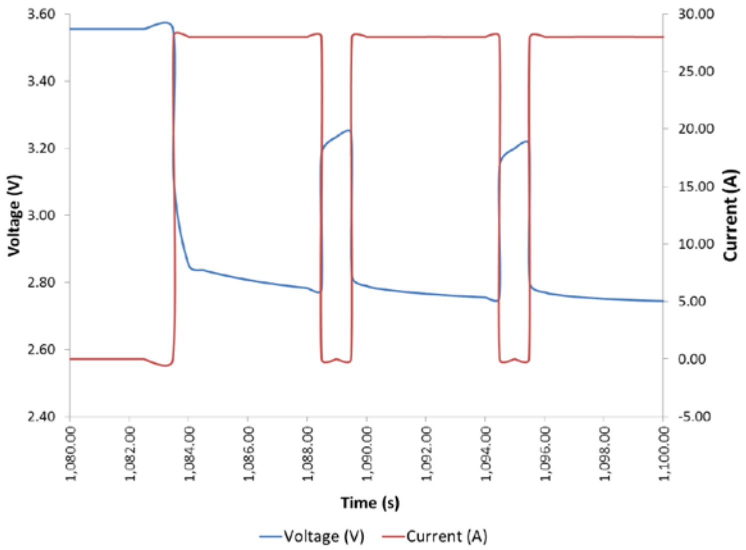

Figure 4-19: Zoomed in view of the current and voltage waveforms recorded during one of the elevated pulsed discharge experiments.

Figure 4-20 plots the capacity los versus cycle number for each of the two respective cells tested. Notice that after 420 cycles, the cell discharged down to 2.0V has experienced a capacity loss of roughly 20%. The cell discharged down to 2.5 V is able to be cycled just over 700 times before it reaches a capacity loss of 20%. The lower discharge voltage of 2.0 V forces more lithium ions out of the anode than the discharge to 2.5 V does. The result in higher stress placed on the anode and the SEI layer resulting in a faster capacity fade.

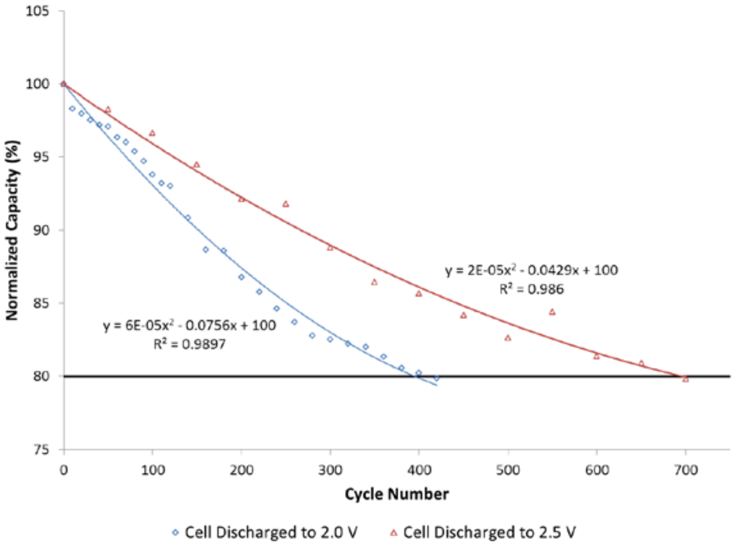

Figure 4-20: Normalized Capacity of 2.6 Ah $LiFePO_4$ lithium-ion cell under different test scenarios

The impedance analyses from the EIS Nyquist plots are used to help understand what may be occurring in the different cells. These are plotted in Figure 4-21 to Figure 4-23. The plots from the cell which was pulsed discharged to 2.0 V, indicate that the capacity fade is caused by an increase in electrolyte resistance and charge transfer resistance. Despite the fact that each cell has experienced the same 20% capacity fade, the total change in electrolyte and charge transfer, between the initial cycle and final cycle of each respective cell, is not the same as seen in Figure 4-23. However, the cell with lower discharge of 2.0 V could have aged earlier due to graphite exfoliation and cracking causing gas formation and reducing electron count in the cell system [5][49][50].

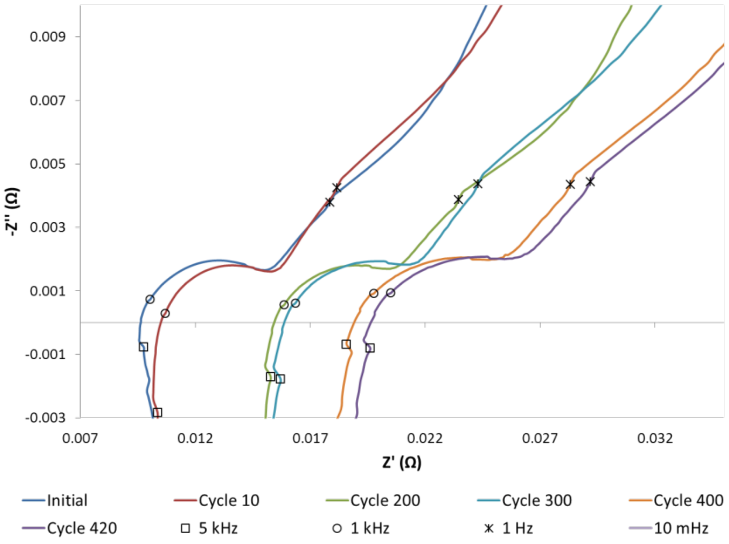

Figure 4-21: Nyquist Plot at 100 % SOC and 3.4 V for the cell discharged to 2.0 V

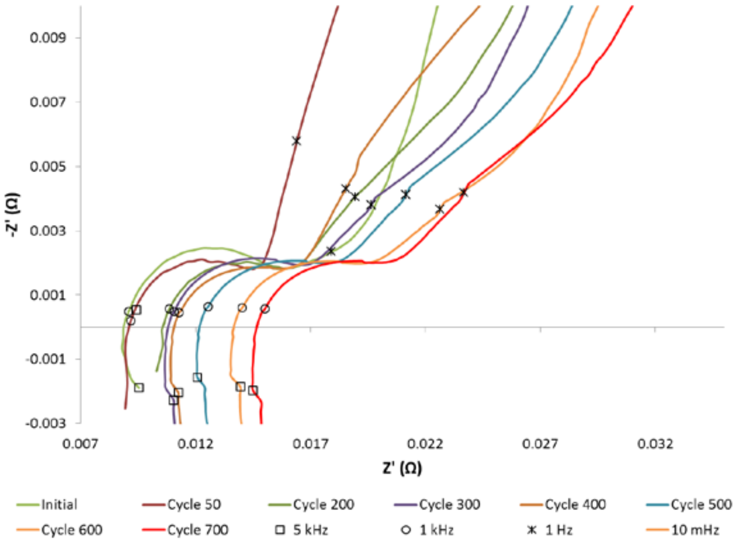

Figure 4-22: Nyquist Plot at 100 % SOC and 3.4 V for the cell discharged to 2.5 V

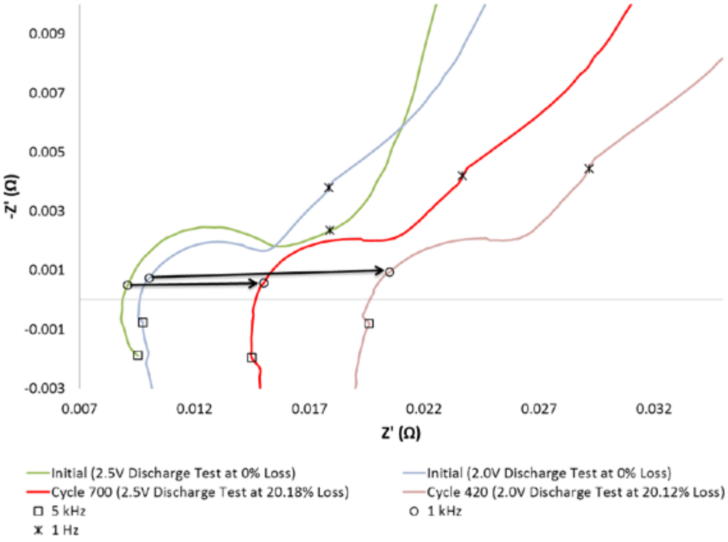

Figure 4-23: Nyquist Plot Comparison at 0% and ~20% Capacity Loss

Aging of three 3 Ah LiNiCoAlO2 (NCA) Lithium-Ion Batteries

In the experiments conducted here, three identical 3 Ah $LiNiCoAlO_2$ (NCA) lithium-ion cell are used. The datasheet properties of the cell are shown in Table 4-3. and a photograph is shown in Figure 4-24. One of the three cells was studied to independently observe the impact of high pulsed rate discharge on its cyclic aging. To achieve this, the cell was discharged at high pulsed rates, but recharged using a nominal 1C, constant current (CC) – constant voltage (CV) procedure. The novel test stand was used to discharge the cell at a peak C rate of roughly 85C. Because the test stand is unable to vary its resistance as the cell is discharged, the discharge rate also decreases proportional to the cell's voltage. The discharge frequency is 10 kHz with a 50% duty cycle. The second of the three cells was cycled at a continuous elevated discharge rate, equal to the average C rate recorded in the high pulsed discharge rate experiment, in attempt to discern the impact which the pulsed nature of the discharge has from the average high C rate itself. That particular cell was discharged using a 25C CC procedure and recharged using a 1C CC – CV procedure. Finally, the third cell was considered to be the control cell since it was both charged and discharged using a 1C, CC – CV procedure. As part of the experimental process, periodic 1C baseline procedures, identical to the manner in which the control cell was cycled, were performed to measure the capacity fade of each respective cell as a function of cycle number. The 1C charge/discharge procedure was used to ensure each of the three cells was being compared using a fair metric. Also, as part of the baseline procedure, electrochemical impedance spectroscopy (EIS) measurements were made for use in hypothesizing what may be occurring inside the cells. The experimental procedure performed on each of the three respective cells is detailed in Figure 4-25 in Table 4-4.

Table 4-3: Datasheet properties of the 3 Ah $LiNiCoAlO_2$ (NCA) lithium-ion battery

Capacity	**Weight**	**Specific Power Density**	**Specific Energy Density**	**ESR**
3 Ah	0.21 kg	17.3 kW/kg	71 Wh/kg	~1.5 mΩ

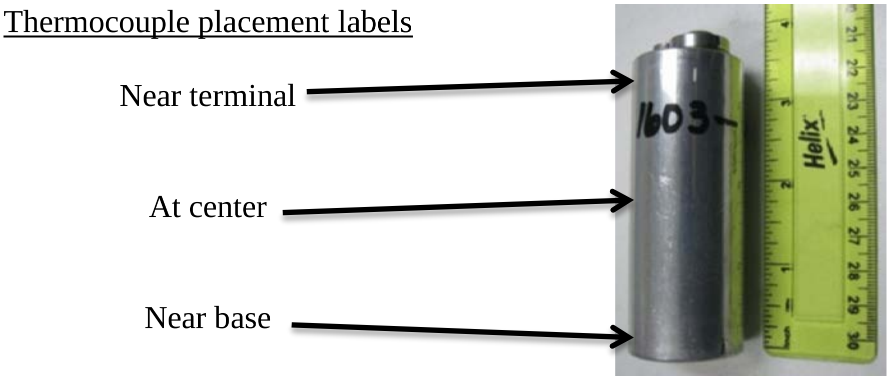

Figure 4-24: 3 Ah LiNiCoAlO2 (NCA) lithium-ion battery with a thermocouple placement label

Table 4-4: Experimental test procedure for high rate pulsed discharge variable cell, high rate continuous discharge variable cell, and control cell

	Cell 1 High Rate Pulsed Discharge Variable Cell	**Cell 2 High Rate Continuous Discharge Variable Cell**	**Cell 3 Control Cell**
Recharge Parameters	1. CC at 3 A (1C) until V equals 4.1 V 2. CV at 4.1 V until I is less than 0.3 A (C/10)	1. CC at 3 A (1C) until V equals 4.1 V 2. CV at 4.1 V until I is less than 0.3 A (C/10)	1. CC at 3 A (1C) until V equals 4.1 V 2. CV at 4.1 V until I is less than 0.3 A (C/10)
Discharge Parameter	1. 10 kHz discharge with a 50% duty cycle across a 1.4 mΩ load until V = 1.5 V – 2.0 V	1. CC at 75 A (25C) until V equals 3.0 V	1. CC at 3 A (1C) until V equals 3.0 V

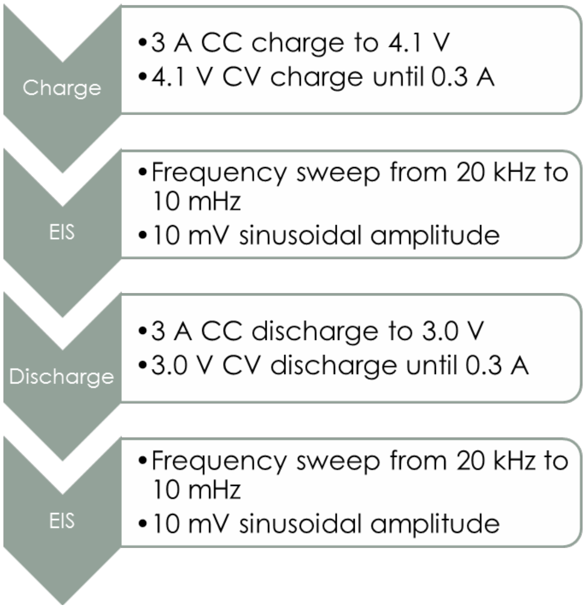

Figure 4-25: 1C baseline procedure

As indicated, EIS measurements were made in the periodic baseline procedure as an in-situ measurement technique aimed at understanding how the cell changes as a function of cycle life. EIS measurements were performed after the cell rested for at least 1 hr after a respective charge or discharge procedure, providing sufficient time for the cell's diffusion process to reach its steady state. The MetrOhm potentiostat applied a sinusoidal signal with amplitude of 10 mV over a frequency range of 20 kHz to 10 mHz.

Elevated Rate Pulsed Discharge Cycling Induced Aging

Elevated rate pulsed discharge cyclic aging is the focus of the experiments performed on this first cell. The cell underwent an elevated pulsed discharge coupled with a 1C nominal rate recharge along with the baseline measurement performed after every 10 cycles, as described by Figure 4-26. The manufacturer has stated that the cell can withstand more than 1000 cycles when used at nominal rates. The nominal cycling rate is 3 A with the operating voltage range of 3.0 V to 4.1 V at continuous rate and 1.5 V to 4.1 V at pulsed rates [1]. The objective is to understand the induced aging when the pulsed discharge is performed at high C rate. To avoid any contributions of early aging contributed by recharging the cell, the cell was recharged using a standard constant current and constant voltage (CC – CV) method with 3 A (1C) of constant current and 4.1 V of constant voltage until the current falls below 0.3 A (C/10). A capacity loss of 20% was observed after 400 elevated rate discharge cycles had been performed. The flow chart shown in Figure 4-26 describes the test procedure the elevated rate procedure that was performed on the cell.

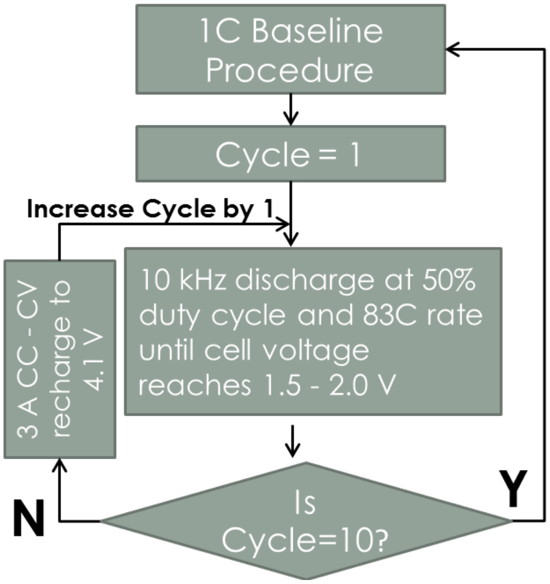

Figure 4-26: High rate pulsed discharge variable cell

The voltage and current profile for complete high rate pulsed discharge rate is shown in Figure 4-27 and Figure 4-28. In the those plots, the zoomed in area shown on the right side of each figure highlights the voltage and current profile for first 400 µs and comparative data recorded from discharge cycle 3 and 400. In the figure, the cell voltage during cycle 3 and 400 started at same potential of 4.02 V. Discharge 3 lasted roughly 140 s, at which point the cell's voltage had decreased to approximately 1.6 V. After the discharge is completed, the cell's voltage stabilizes with an open circuit potential (OCP) of just over 2.5 V. The lower conduction voltage and higher current in cycle 400 as opposed to cycle 3 indicates that contact impedance within the stand was slightly less in cycle 400 than in cycle 3. It is also possible that the ~1 mΩ variable resistance had been slightly altered between these two discharge cycles.

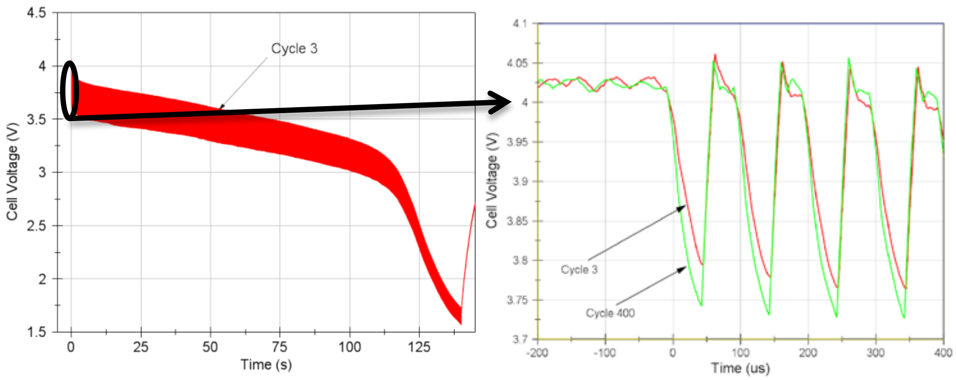

Figure 4-27: Voltage profiles measured during discharge cycle three on the left and zoomed plot shown on the right with data from cycle three and four hundred.

The observed peak discharge current is approximately 83C (250 A) and the average equivalent continuous discharge current was approximately 25C (75 A). In the zoomed plot of Figure 4-28, the comparative current data from discharge cycle 3 and 400 for the first 400 μs is shown. The peak current for cycle 400 is slightly higher than cycle 3, again as a result of the slightly varied stand impedance. The plot shows how the current magnitude decreases along with the voltage of the cell.

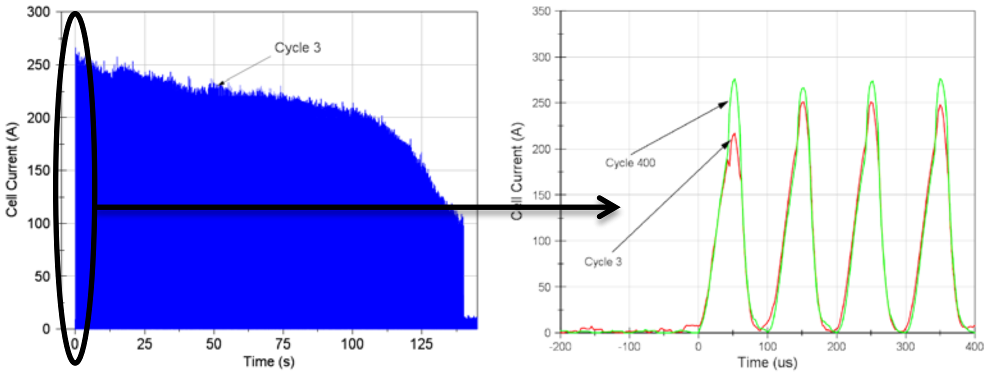

Figure 4-28: Current profiles measured during discharge cycle three on the left and the zoomed plot shown on the right with data from cycle three and four hundred.

The coulomb counting results, recorded during baseline procedure, are used to calculate the cell's capacity (Ah) and capacity loss in percentage as the cycling progresses. These results are shown in Figure 4-29 and Figure 4-30 respectively. The decrease in capacity measured with increasing cycle number shows how the cell ages as a function of cycle life. Before cycling began, the measured cell capacity was 3.13 Ah. After 400 elevated rate pulsed discharge cycles, the capacity had decreased to 2.45 Ah, equating to a roughly 20.48% capacity loss. The coulomb counting shows how the cell ages but does not tell why it ages. The steady increase in capacity loss fits a second order polynomial curve with a coefficient of determination (R^2) value of 0.95. The capacity of the cell as a function of cycle number (N) can be estimated with an equation 1 which has a roughly 5% error. The sinusoidal nature of the capacity loss curve is believed to be a function of rest time between cycles. The time between cycling could often go a few days or even weeks depending up on the laboratory schedule. It was observed that if a long period of time had lapsed between cycles, the capacity extracted from the first cycle performed after the rest would actually give more capacity than the cycle previously conducted. This is believed to be due to the cell having time to fully stabilize and for lithium to fully intercalate into the anode. Also, the long rest period allows the soluble precipitate on the surface of the electrodes deposited during cycling to dissolve back into the electrolyte [36]. This causes the lithium on the precipitate to return back to electrochemical process increasing the capacity [36]. This fluctuation causes the most of the error in the curve fit of equation 4.

$$Capacity\ (Ah) = \frac{Initial\ Capacity * (100 + 6^{-5} * N^2 - 0.0735 * N)}{100} \quad (6)$$

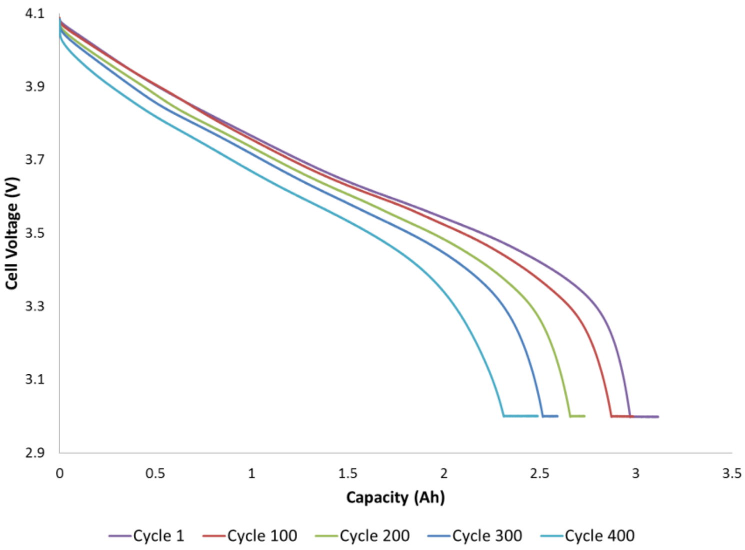

Figure 4-29: Cell capacity measured during baseline procedure after elevated rate pulsed discharge

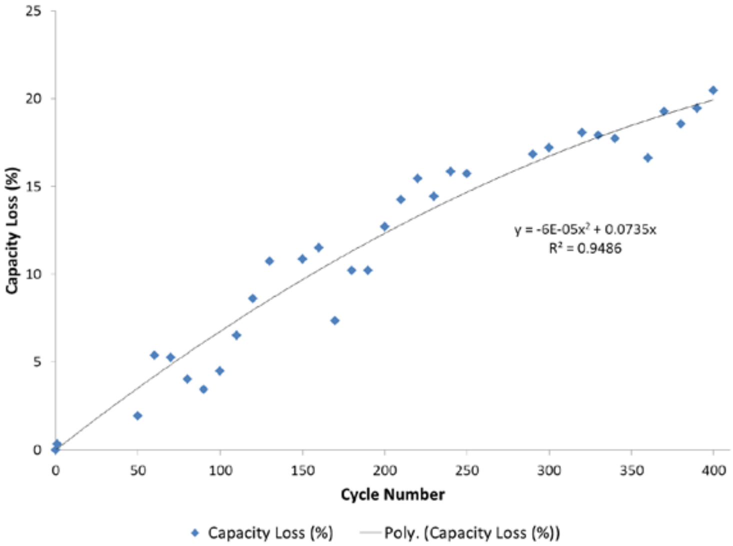

Figure 4-30: Capacity loss percentage as a function of cycle number during elevated rate pulsed discharge

The Nyquist plots obtained from periodic EIS measurements are shown in Figure 4-31. The EIS measurement on the cell was done periodically after every 10 elevated pulsed discharge cycles. The plot shown is obtained by performing the frequency sweep from 20 kHz to 10 mHz with an amplitude of 10 mV when the cell is at 100 % SOC. The plot shown can be divided into four parts – the inductive tail, mid frequency semi-circle, low frequency semi-circle, and Warburg impedance. Inductive tail is a higher frequency response shown on the left hand side of the graph below the zero of y-axis. In the battery, the inductive tail is of little interest to the aging study, therefore the complete tail recorded during the higher frequency response is not shown. The displacement along the x-axis, where the curve crosses x-axis, represents the electrolyte resistance [36]. From the Nyquist plot, it was observed that the electrolyte conductivity increased at the beginning due to the cell settling in. The plot shows that the electrolyte conductivity increased until roughly 110 cycles had been performed. After that, the electrolyte conductivity started to decrease significantly. Despite the growth, the electrolyte conductivity after cycle 400, at which point the cell has 20% less capacity, is still higher than that of initial. The width and height of the medium frequency semicircle decreases slowly, indicating that there is an increase in passive film formation on the electrodes. The width and height of low frequency semicircle increases with cycle number, indicating an increase in the internal charge transfer resistance (both the interfacial and surface film resistances of the cathode and anode).

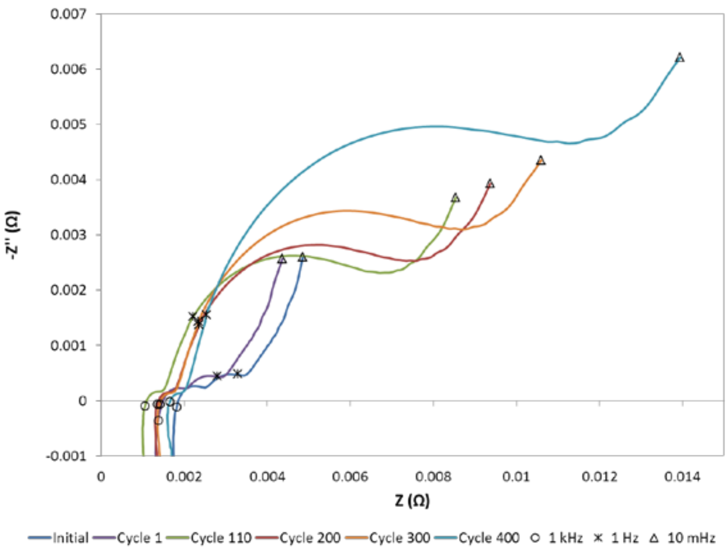

Figure 4-31: Nyquist plot at 100% SOC and 4.1 V

In Figure 4-32, the maximum temperature near the terminal, at the center, and near the base are shown as a function of cycle number. The placements of thermocouples are shown in Figure 4-24. The missing data point refers to the cycles in which the respective data points were not collected. Initially, not all three temperatures were measured. The plot shows that the maximum temperature never crosses above 50°C which is below the peak operating temperature as mentioned in datasheet [16]. Thus, the aging effect that could have been caused by temperature is neglected. On comparison, the temperature near the base is higher when compared to the temperature at the center and the temperature at the center is higher than the temperature near terminal. This is because the terminal of the battery is connected to large copper conductor which acts as a heat sink. On the other side, the base of the battery is in contact with an insulator limiting the rate of heat loss and thus resulting in a higher temperature.

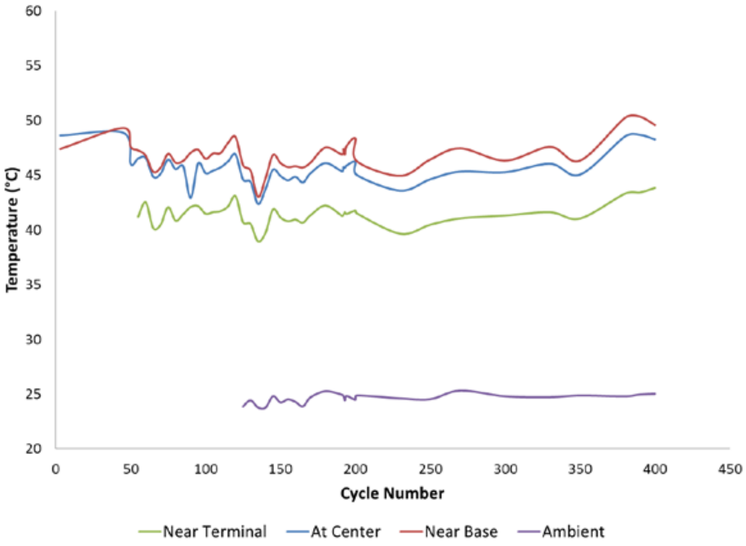

Figure 4-32: Maximum cell temperature attained during elevated rate pulsed discharge

Elevated Rate Continuous Discharge Cycling Induced Aging

Through the results obtained in the elevated rate pulsed discharge cycling, it was clear that the elevated pulsed discharge significantly ages the cell. In order to determine the difference in the aging rate when pulsed and continuous high rates are discharged, a second identical cell was discharged at an elevated continuous discharge rate. Only 400 cycles were performed as the desire was to compare the results from this cell to those obtained from the first cell. The flow chart detailing the experimental procedure is shown in Figure 4-33.

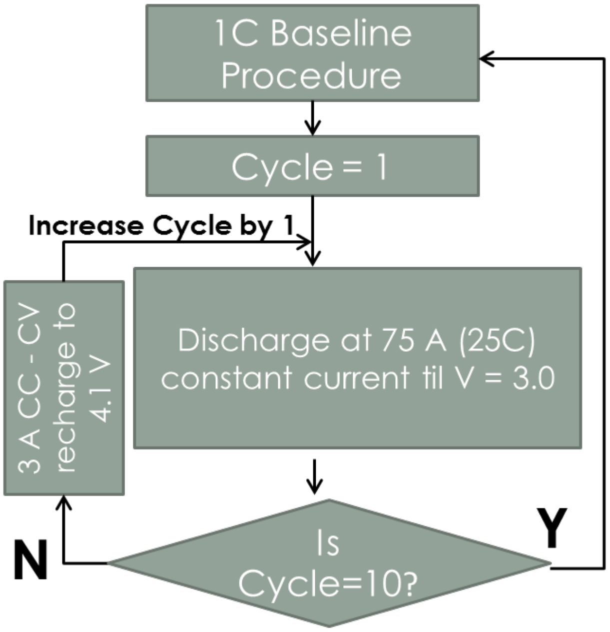

Figure 4-33: High rate continuous discharge variable cell

The discharge rate was chosen so that the continuous discharge rate is equal to the average equivalent continuous discharge rate extracted during the pulsed discharge. The average rate of the pulsed discharge was calculated to be approximately 25C or 75 A. The discharge current profile used in these tests is shown in Figure 4-34 and the corresponding voltage profile is shown in Figure 4-35. The cutoff discharge voltage was set to 2.0 V. It was observed that the elevated continuous discharge lasted for 122 s when compared to 140 s in elevated rate pulsed discharge because of the difference in the two cell’s initial capacity, which were measured to be 2.98 Ah for cell 2 vs. 3.13 Ah for cell 1 respectively.

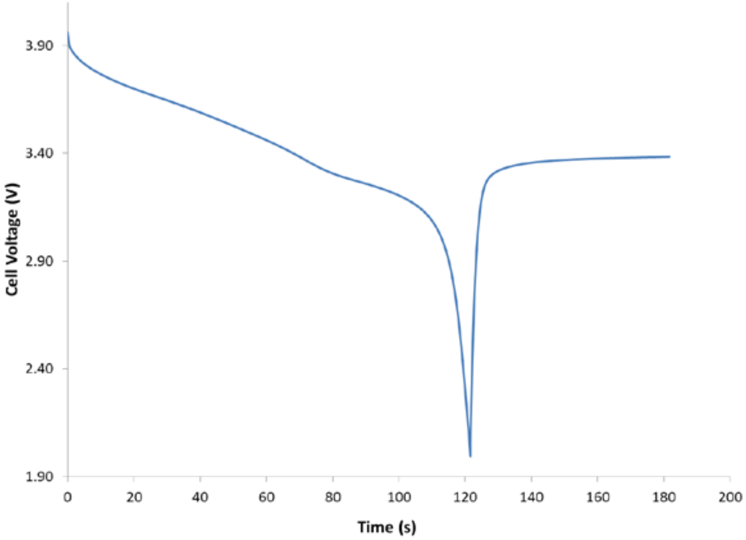

Figure 4-34: Cell current during elevated continuous discharge at 25C rate

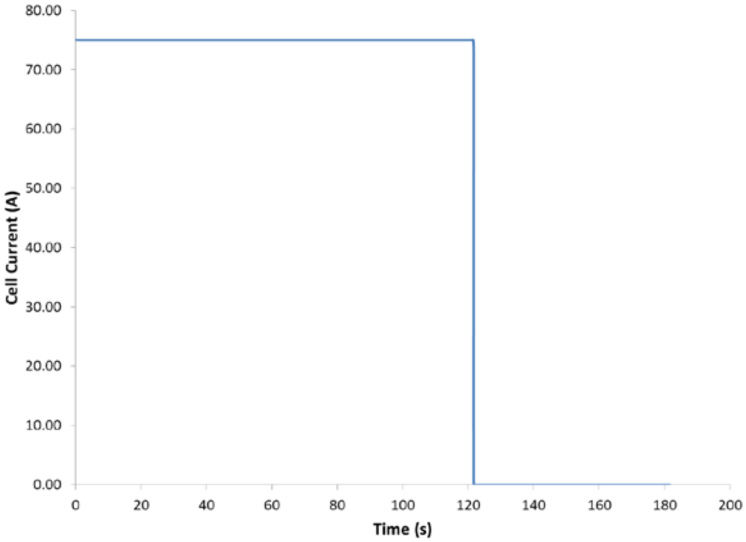

Figure 4-35: Cell voltage during elevated pulsed discharge at 25C rate

The cell's capacity and capacity loss percentage obtained through periodic coulomb counting is shown in Figure 4-36 and Figure 4-37 respectively. The steady increase in capacity loss percentage is shown in Figure 4-37. The increase in capacity loss fits a third order polynomial curve, with a coefficient of determination (R^2) value of 0.88. The capacity of the cell as a function of cycle number (N) can be estimated with an equation 5 which has a roughly 12% error. Mathematical model are fairly inaccurate with an error of 10% to 20% [53], so an error of 12% is can be considered normal.

$$Capacity\ (Ah) = \frac{Initial\ Capacity*(100-1^{-7}*N^3+1^{-4}*N^2-0.0426*N)}{100}$$

(7)

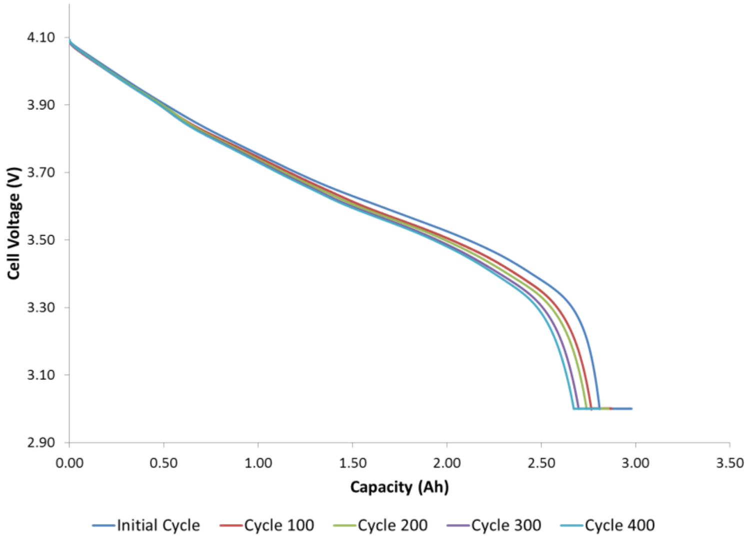

Figure 4-36: Cell capacity measured during baseline procedure after elevated continuous discharge at 25C rate

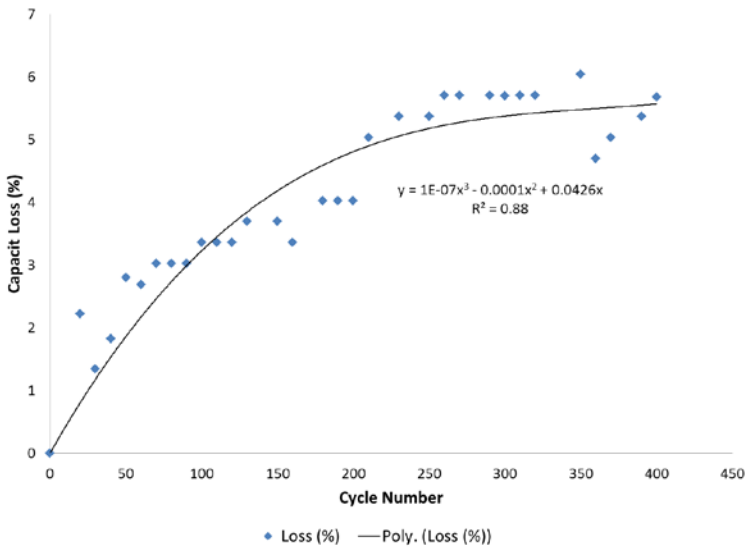

Figure 4-37: Capacity loss percentage as a function of cycle number during elevated continuous discharge at 25C rate

The Nyquist plots obtained from The EIS measurements are shown in Figure 4-38. The EIS measurements were obtained periodically after every 50 elevated continuous current discharge cycles. The plot shown is obtained by performing the frequency sweep from 20 kHz to 10 mHz with an amplitude of 10 mV and the cell at 100% SOC. From the Nyquist plots, it is observed that the electrolyte conductivity remained fairly consistent. The width and height of the medium frequency semicircle decreases at an almost negligible rate, indicating that there is not much of an increase in the electrodes' passive film formation. However, the width and height of low frequency semicircle is increases with the increase in cycle number indicating an increase in internal charge transfer resistance (both the interfacial and surface film resistances of the cathode and anode).

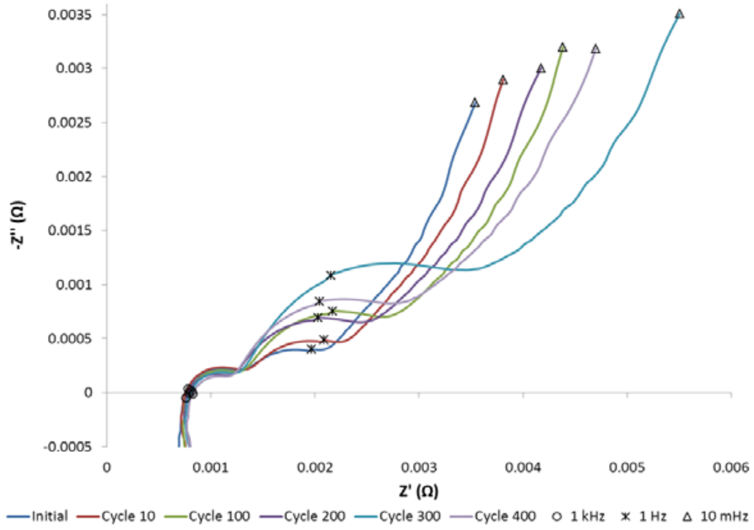

Figure 4-38: Nyquist plot at 100% SOC and 4.09 V

Figure 4-39 shows the peak cell temperature reached during the elevated rate continuous discharge cycles. The peak temperature during all of the experiments never went above 34°C which is within the operating temperature range of the cell. Thus, the aging effect that could have been caused by temperature is neglected.

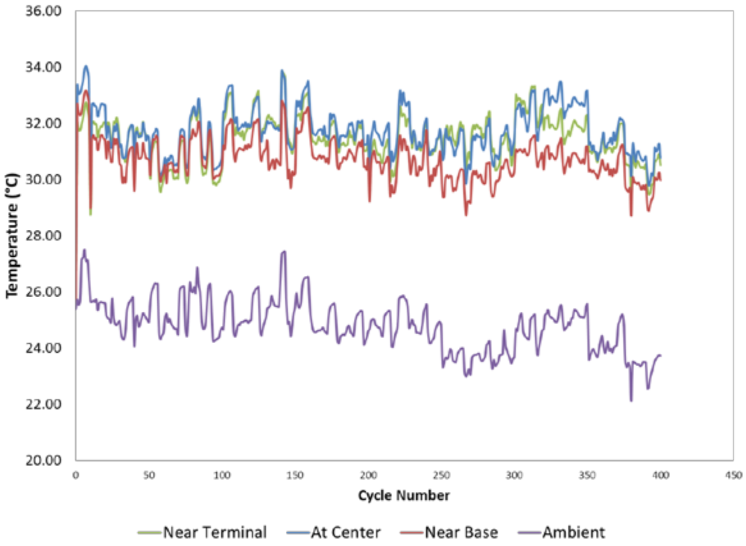

Figure 4-39: Maximum cell temperature observed during elevated rate continuous discharge

Nominal Rate Cycling Induced Aging

Nominal rate cycling, performed on a third identical 3 Ah NCA cell, consisted of a 1C charge and 1C discharge cycle with baseline measurement performed after every 50 cycles. This procedure is shown in Figure 4-40. The cycling was performed for 400 cycles for comparative analysis with the other two cells. After 400 cycles, the cell showed no significant aging. The measured cell capacity, as shown in Figure 4-41, showed no decrease in the cells 1C capacity. Similarly, the ES measurements, shown in Figure 4-42, shows negligible changes between cycles. In scrutinizing the Nyquist plots, it can be observed that there is a change in the electrolyte conductivity and charge transfer resistance but the change is so small that it does not have any effect on the capacity of the cell. The ambient temperature during nominal rate cycling was 25°C and the cell temperature was not monitored because of the low rate cycling, the temperature rise will be almost negligible.

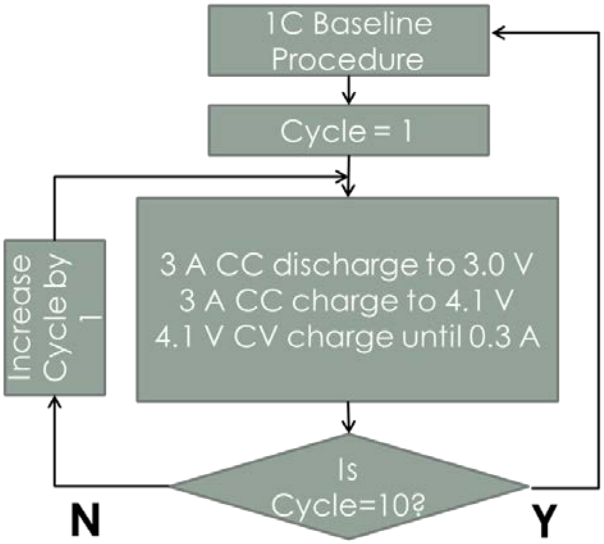

Figure 4-40: Nominal rate cycling control cell

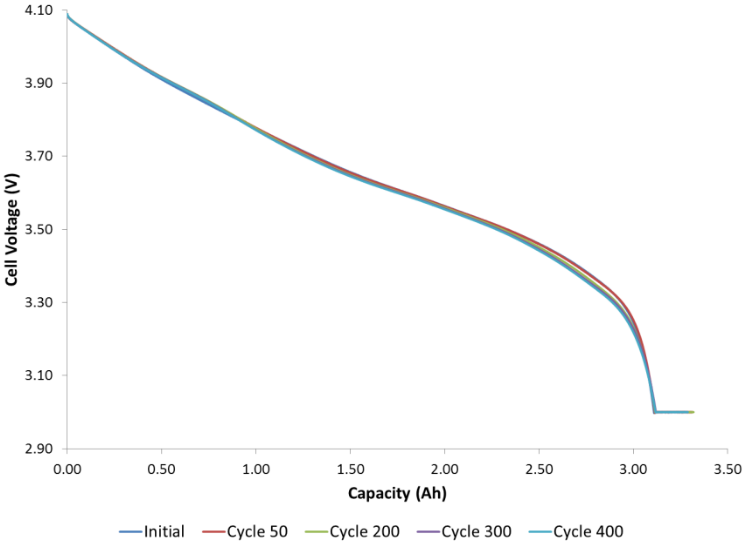

Figure 4-41: Cell capacity measured during nominal rate cycling

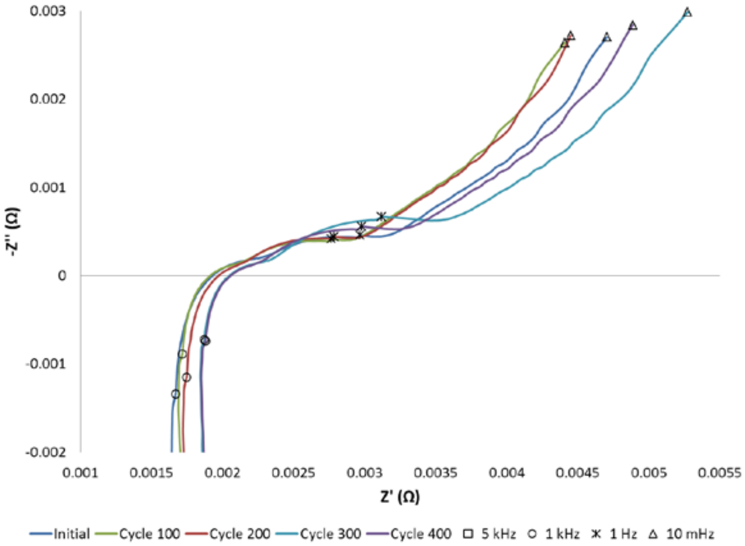

Figure 4-42: Nyquist plot at 100% SOC and 4.09 V

Aging Analysis

Figure 4-43 shows the comparative capacity loss observed from the three cells just discussed, those being the elevated rate pulsed discharge cell, the elevated rate continuous discharge cell, and the nominal rate cell. From a coulomb counting aspect, it can be concluded that the elevated rate pulsed discharge has a greater impact on aging compared to elevated rate continuous discharge if the average discharge rate is maintained. The nominal cycle shows no indication of aging after 400 cycles, thus it can be determined that the aging observed during elevated rate pulsed discharge cycling and elevated rate continuous discharge cycling is only due to the discharge profile. This means that the charge profile has not significantly contributed to aging of the two high rate cells. Further, the comparative capacities of three cells are listed in Table 4-5.

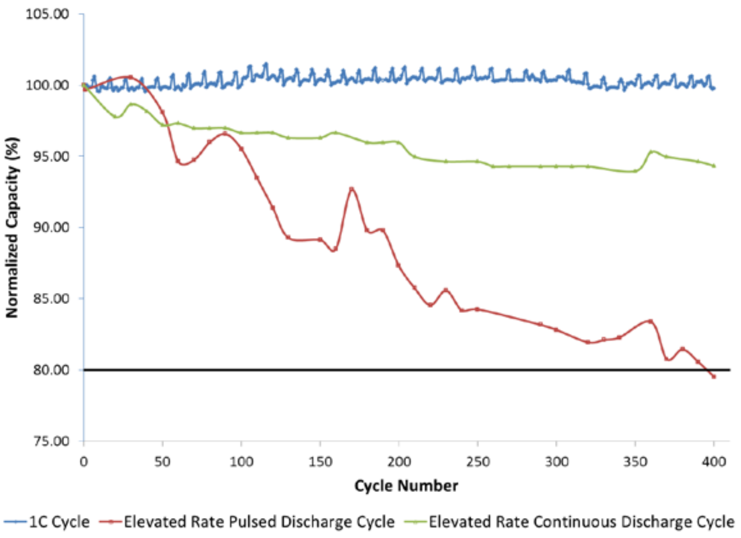

Figure 4-43: Normalized capacity of 3 Ah $LiNiCoAlO_2$ (NCA) lithium-ion cell under different test scenarios

Table 4-5: Capacity comparison between three 3 Ah $LiNiCoAlO_2$ (NCA) lithium-ion cell before and after cycling

	Initial Capacity (Ah)	Capacity after 400 cycles (Ah)	Capacity lost after 400 cycles (%)
Cell 1: High Rate Pulsed Discharge Variable Cell	3.13	2.49	20.48
Cell 2: High Rate Continuous Discharge Variable Cell	2.98	2.81	5.68
Cell 3: Control Cell	3.10	3.10	0

Chapter 5

Modeling and Simulation

Modeling Background

Modeling a lithium-ion battery is a complex task and often users must empirically derive a model of the battery they are using as no one model is universal. There are several types of models which can be used based on the situation needed. There are electrochemical models which use time-varying partial differential equations and these can be computationally extensive [52]. This type of model is often used in the physical design of electrodes and electrolytes. Mathematical models are good for predicting runtime, efficiency, and capacity using a stochastic approach or empirical equations but they often come with an error of approximately 5% to 10% [53]. This model bears no relationship between the model parameters and I-V characteristics of the batteries which makes it of less value in simulation software [54]. Electrical models as shown in Figure 5-1 use Thevenin equivalent, impedances, or runtime models [55]. A Thevenin model uses some assumptions such as open-circuit voltage is constant is normally constant along with use a series resistor with RC parallel network for transient response of the load [54]. In addition, the accuracy of the battery's response prediction can be increased by simply increasing the number of parallel RC networks. Impedance models are fairly accurate for predicting DC response and the battery runtime provided that the SOC and temperature remains constant. Impedance spectroscopy uses Thevenin models with time constants parameters obtained by fitting an equivalent network to the measured impedance spectra [13]. In runtime-based electrical models, continuous or discrete time is implemented to simulate battery runtime and DC voltage response for constant current discharges [13].

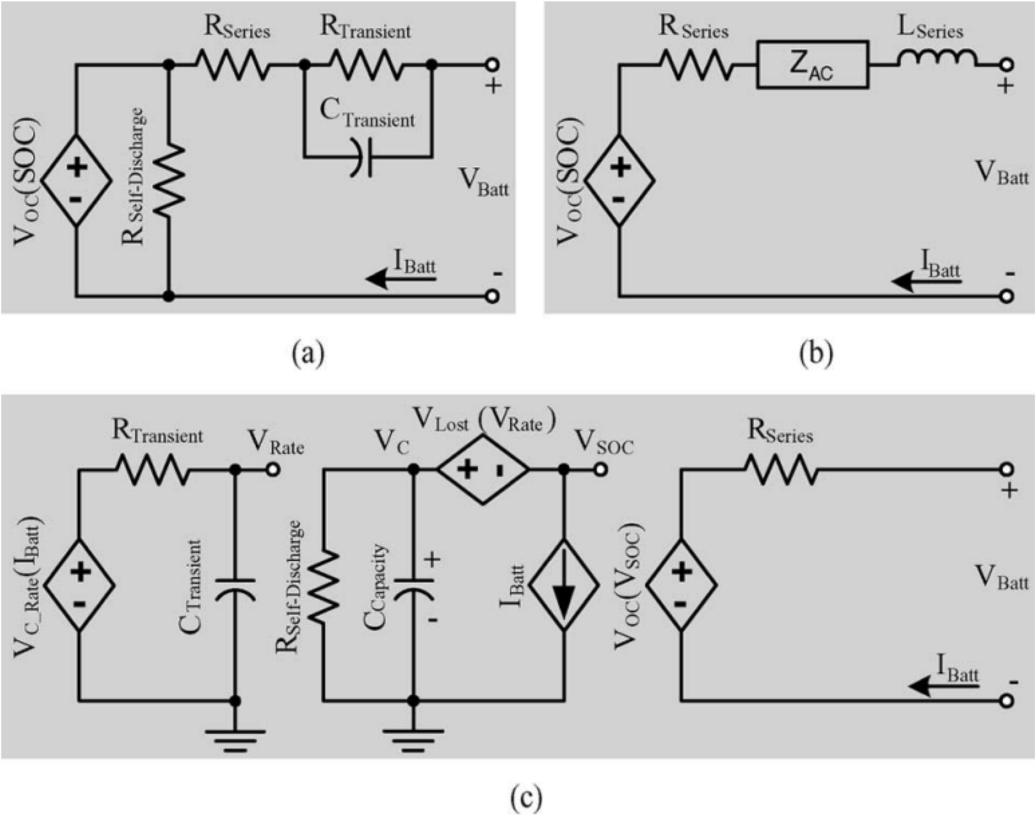

Figure 5-1: Electrical battery models: (a) Thevenin, (b) Impedance, and (c) Runtime-based [54]

Using a combination of different circuit models, Kroezee [13] proposed a generic battery model as shown in Figure 5-2, which can accurately represent lithium-ion battery behaviors including a prediction of its state of charge, determination of the I-V characteristics, and determination of its dynamic behavior. However, this model is accurate for constant temperature and capacity.

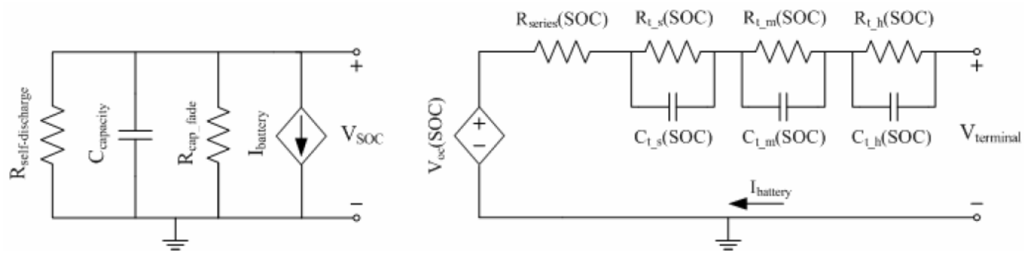

Figure 5-2: Generic battery model for battery at a constant temperature [14]

In another effort, Tremblay [14] developed a non-linear battery model as shown in Figure 5-3, which can be used to accurately represent the discharge curves of a battery. The model is simple and uses only the battery's state of charge as a state variable. The model's parameters are easily extracted from the manufacturer's discharge curve.

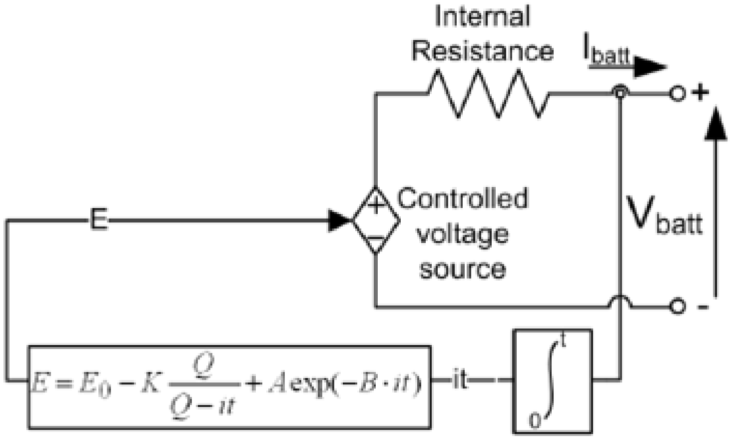

Figure 5-3: Non-linear battery model [15]

Impedance Model of 3 Ah LiNiCoAlO2 (NCA) lithium-ion cell

An impedance model of the 3 Ah NCA cell tested here was derived based on the Nyquist plots obtained from the cell's EIS measurements. The equivalent circuit model of the 3 Ah LiNiCoAlO2 (NCA) cell is shown in Figure 5-4. The circuit elements such as inductance (L), resistance (R), capacitance (C), constant phase element (CPE), and Warburg impedance (W) can be arranged to get the required impedance model. The constant phase element is nothing but is an equivalent electrical circuit model which behaves as a double layer capacitor. Warburg impedance on the other hand is an example of a constant phase element for which the phase angle is 45° regardless of frequency.

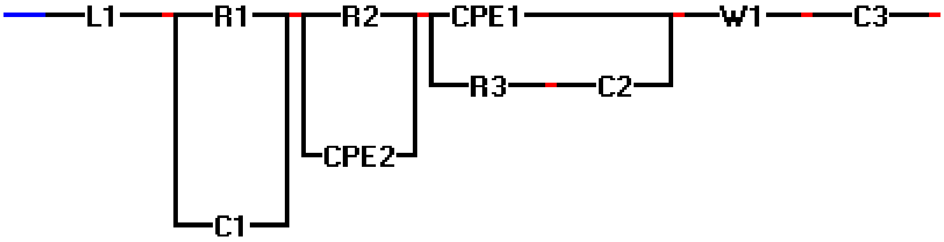

Figure 5-4. Equivalent impedance model for the 3 Ah $LiNiCoAlO_2$ (NCA) lithium-ion battery

Figure 5-5 to Figure 5-10 shows a comparison of the measured and simulated Nyquist plots before and after 400 cycles had been performed on the three cells tested. The equivalent circuit's component parameter values, including the inductance, capacitance, resistance, constant phase element, and Warburg element, are calculated using the EIS Spectrum Analyzer software. The data collected using this method as a function of cycle number is shown in Table 5-1 to Table 5-3.

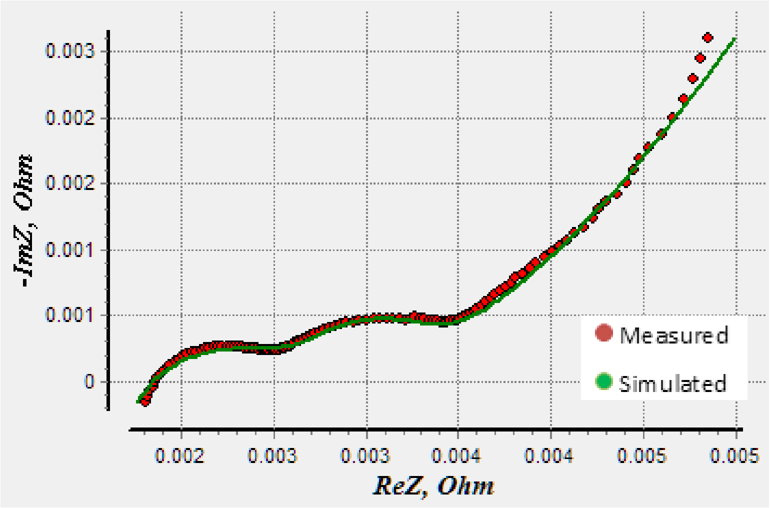

Figure 5-5 Comparison of the impedance curves, both measured and simulated, performed before any cycling was performed on the elevated rate pulsed discharge 3 Ah $LiNiCoAlO_2$ (NCA) lithium-ion battery

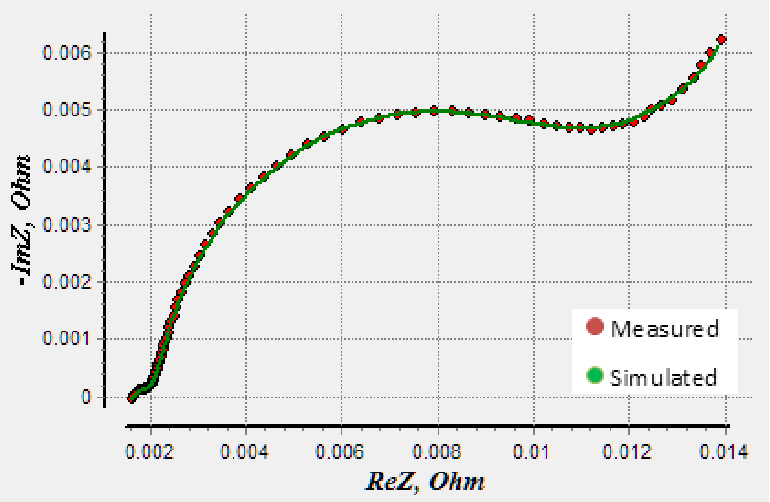

Figure 5-6: Comparison of the impedance curves, both measured and simulated, performed after 400 cycles were performed on the elevated rate pulsed discharge 3 Ah LiNiCoAlO2 (NCA) lithium-ion battery

Table 5-1 Parameters of impedance model at different cycles at 100 % SOC for the cell with elevated rate pulsed discharge cycle

Cycle	C1	C2	C3	R1	R2	R3	W	P1	N1	P2	N2	L1
Initial	247.51	2.73E+04	3.24E+04	3.95E-04	4.18E-10	3.06E-03	3.95E-04	2.16E+01	2.76E-01	7.74E+03	1.89E-14	7.74E-08
1	3.30E+00	1.65E+04	9.40E+04	2.60E-04	3.71E-04	2.47E-03	4.03E-04	1.66E+02	1.87E-01	1.05E-07	1.07E+00	1.05E-07
50	1.36E+02	1.00E+06	1.00E+06	2.64E-03	8.26E-12	1.20E-03	8.48E-04	6.92E-13	1.03E+00	2.72E+04	1.50E-03	1.44E-09
110	3.92E+03	1.67E+04	1.39E+05	6.93E-04	3.97E-03	1.58E-03	5.83E-04	9.89E+00	4.16E-01	1.52E+02	9.79E-01	6.08E-08
180	1.16E+03	4.52E+04	5.28E+04	1.38E-03	3.48E-03	1.68E-03	7.69E-04	7.30E+00	4.11E-01	1.73E+02	1.00E+00	6.23E-08
200	4.10E+03	1.66E+04	7.22E+04	8.36E-04	4.34E-03	1.86E-03	5.84E-04	9.10E+00	3.71E-01	1.51E+02	9.72E-01	4.88E-08
250	1.93E+03	2.34E+04	1.50E+05	1.15E-03	4.39E-03	1.86E-03	7.81E-04	6.00E+00	4.02E-01	1.62E+02	9.89E-01	7.34E-08
300	4.41E+03	1.38E+04	2.33E+04	1.19E-03	5.74E-03	1.89E-03	4.62E-04	9.32E+00	3.54E-01	1.44E+02	9.55E-01	4.56E-08
330	4.98E-13	5.11E+01	8.59E+03	3.73E-08	3.35E-11	3.92E-03	1.40E-04	1.20E+02	9.79E-02	5.86E-07	1.99E+00	5.16E-08
360	9.18E-13	5.65E+01	1.06E+04	2.57E-04	5.36E-05	3.72E-03	2.97E-04	1.21E+02	8.72E-02	4.24E-13	2.00E+00	2.60E-08
400	6.28E+00	6.87E+01	5.31E+03	9.22E-05	2.83E-04	2.76E-03	3.54E-05	9.71E+01	1.06E-01	4.82E+02	8.49E-01	2.54E-08

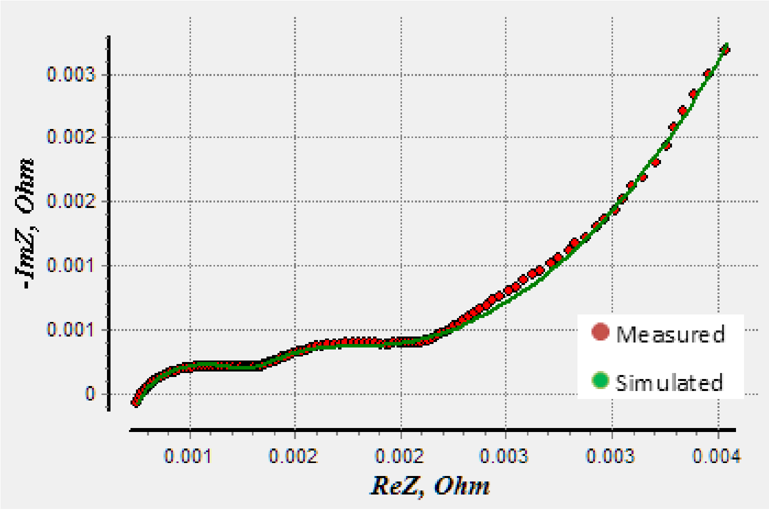

Figure 5-7: Comparison of the impedance curves, both measured and simulated, performed before any cycling was performed on the elevated rate continuous discharge 3 Ah $LiNiCoAlO_2$ (NCA) lithium-ion battery

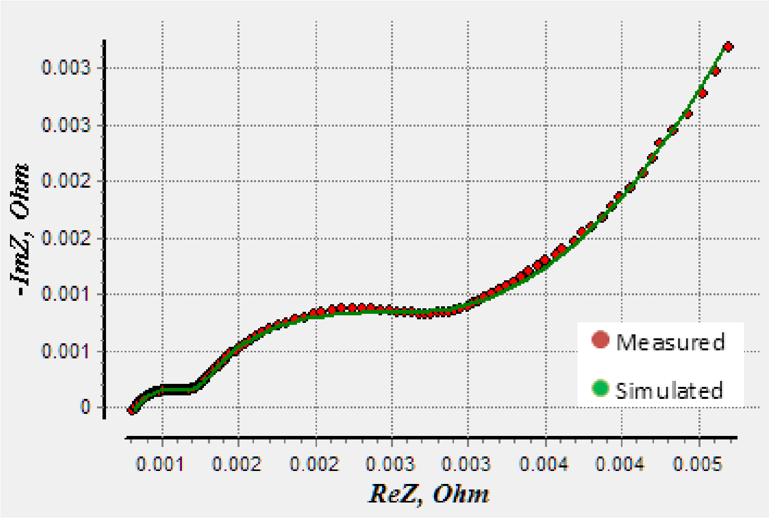

Figure 5-8: Comparison of the impedance curves, both measured and simulated, performed after 400 cycles were performed on the elevated rate continous discharge 3 Ah $LiNiCoAlO_2$ (NCA) lithium-ion battery

Table 5-2: Parameters of impedance model at different cycles at 100 % SOC for the cell with elevated rate continuous discharge cycle

Cycle	C1	C2	C3	R1	R2	R3	W	P1	N1	P2	N2	L1
Initial	3.91E-02	1.08E+00	1.20E+04	7.30E-04	2.69E-04	6.13E-06	2.79E-04	9.23E+02	1.19E-01	1.49E+02	1.11E+00	4.82E-08
50	3.81E-02	1.08E+00	1.17E+04	7.56E-04	7.20E-04	1.04E-05	4.01E-04	9.28E+02	1.12E-01	1.55E+02	1.03E+00	2.99E-08
100	2.78E+00	1.52E+01	8.25E+03	2.54E-04	5.77E-18	3.31E-03	1.90E-04	3.92E+02	1.04E-01	1.26E-16	7.88E-10	2.61E-08
150	2.92E+00	1.33E+01	1.08E+04	2.13E-04	1.91E-18	3.37E-03	2.83E-04	4.90E+02	7.72E-02	4.39E-15	2.82E-09	1.86E-08
200	2.92E+00	1.68E+01	9.95E+03	2.06E-04	1.89E-18	3.07E-03	2.66E-04	4.35E+02	8.81E-02	5.40E-15	8.24E-10	1.86E-08
250	3.05E+00	2.04E+01	1.16E+04	1.96E-04	5.75E-19	2.77E-03	3.09E-04	4.08E+02	8.99E-02	9.65E-15	1.62E-09	3.46E-08
300	3.47E+00	2.59E+01	7.29E+03	1.86E-04	4.37E-20	2.66E-03	8.90E-05	2.84E+02	1.27E-01	1.01E-16	5.54E-09	2.42E-08
350	3.44E+00	2.23E+01	1.07E+04	1.63E-04	8.02E-09	2.73E-03	2.86E-04	3.96E+02	8.90E-02	1.90E-15	3.36E-07	3.69E-23
400	3.19E+00	2.32E+01	1.04E+04	1.74E-04	3.19E-18	2.73E-03	2.82E-04	3.80E+02	9.32E-02	1.56E-16	2.26E-10	2.39E-08

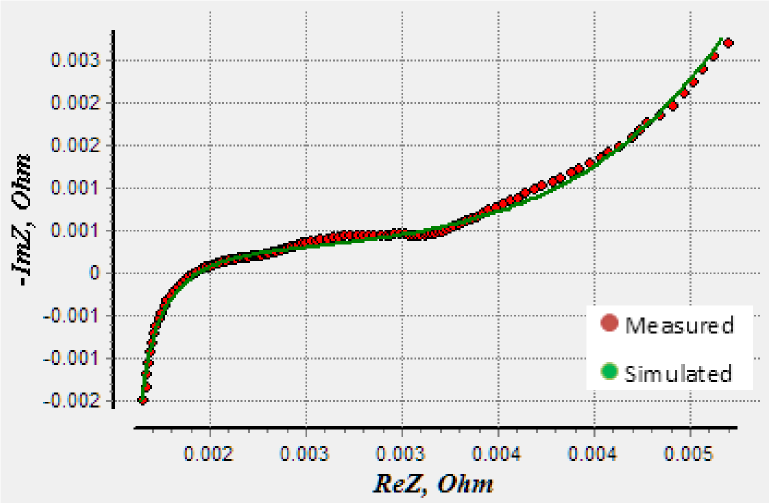

Figure 5-9: Comparison of the impedance curves, both measured and simulated, performed before any cycling was performed on the nominal rate 3 Ah LiNiCoAlO2 (NCA) lithium-ion battery

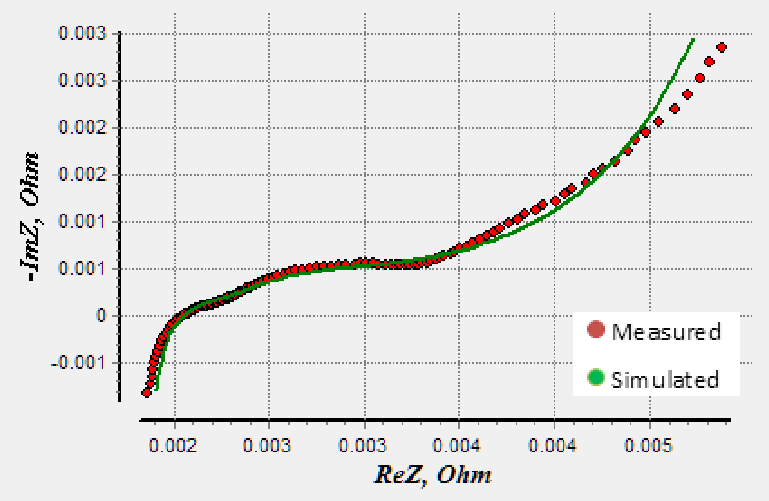

Figure 5-10: Comparison of the impedance curves, both measured and simulated, performed after 400 cycles were performed on the nominal rate 3 Ah $LiNiCoAlO_2$ (NCA) lithium-ion battery

Table 5-3: Parameters of impedance model at different cycles at 100 % SOC for the cell with nominal rate cycle

Cycle	C1	C2	C3	R1	R2	R3	W	P1	N1	P2	N2	L1
Initial	1.02E-12	7.05E-02	9.63E+03	8.93E-04	4.50E-08	4.42E-03	1.36E-04	4.15E+02	1.11E-01	3.68E-15	3.21E-06	2.46E-07
50	6.94E-03	1.70E+02	8.76E+03	9.60E-04	2.35E-20	2.06E-02	1.61E-06	4.11E+02	1.31E-01	1.47E-14	3.18E-05	2.11E-07
100	3.59E+00	3.76E+00	1.43E+04	2.18E-04	1.77E-04	1.13E-02	3.59E-04	4.17E+02	3.51E-02	1.05E-11	5.70E-04	1.64E-07
200	3.11E+00	6.98E-11	8.59E+03	1.06E-04	1.39E-03	6.95E-11	3.54E-18	5.62E+02	1.92E-01	1.74E-12	1.09E-04	2.10E-07
300	8.12E-01	6.51E+00	1.08E+04	2.44E-04	3.31E-20	1.20E-02	3.15E-04	3.09E+02	5.47E-02	1.25E-11	3.65E-06	1.59E-07
400	2.04E+00	5.65E+00	1.35E+04	1.84E-04	2.57E-05	1.18E-02	3.73E-04	3.41E+02	3.74E-02	7.81E-19	5.20E-23	1.48E-07

Impedance Model of K2 26650 2.6 Ah $LiFePO_4$ Lithium-Ion Cell

An impedance model of the K2 26650 2.6 Ah $LiFePO_4$ lithium-ion cell tested here was also derived based on the Nyquist plots obtained from the cell's EIS measurements. The equivalent circuit model is shown in Figure 5-11.

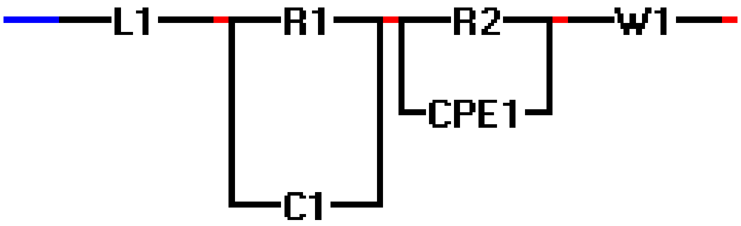

Figure 5-11: Equivalent impedance model for K2 26650 2.6 Ah $LiFePO_4$ lithium-ion cell

Figure 5-12 to Figure 5-15 shows the Nyquist plot comparison of an impedance model between measured and simulated values. Further, parameter values of the components, including the inductance, capacitance, resistance, constant phase element, and Warburg element, are calculated using the EIS Spectrum Analyzer software and the data are listed in Table 5-4 and Table 5-5.

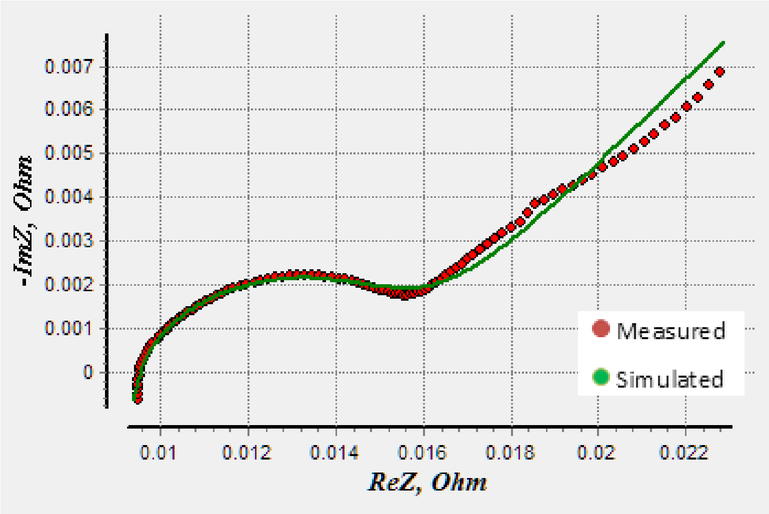

Figure 5-12: Impedance comparison between measured and simulated initially before elevated cycling with a lower discharge voltage of 2.0V

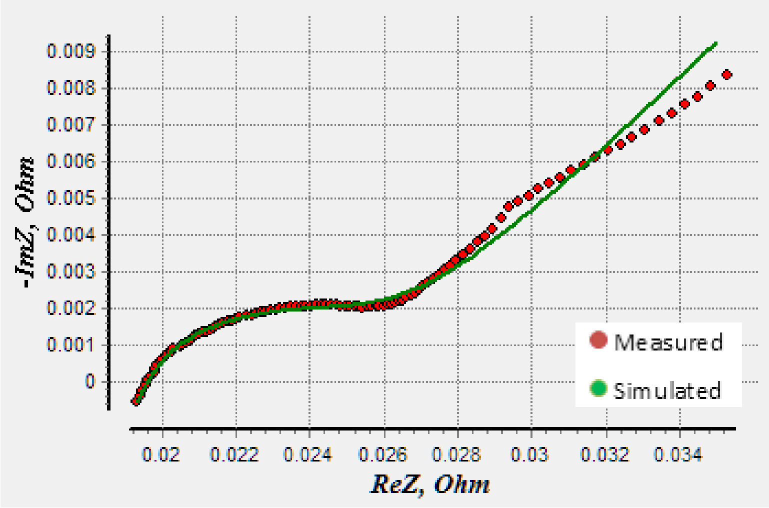

Figure 5-13: Impedance comparison between measured and simulated after 420 cycles and 20.12% capacity loss with a lower discharge voltage of 2.0V

Table 5-4: Parameters of impedance model at different cycles at 100 % SOC for the cell with lower discharge voltage of 2.0 V

Cycle	C1	R1	R2	W1	P	n	L
Initial	1.81E-11	9.10E-03	6.34E-03	7.68E-03	2.24E+00	6.68E-01	3.71E-08
10	2.59E-01	3.18E-03	9.81E-03	1.43E-02	3.97E-09	8.98E-01	7.42E-08
60	6.96E-06	1.11E-02	5.05E-03	8.53E-03	3.43E+00	6.11E-01	7.37E-08
100	1.19E+00	1.38E-03	2.84E-02	6.13E-03	1.48E+01	7.36E-02	8.73E-08
160	1.09E-12	1.61E-02	6.65E-03	7.74E-03	5.92E+00	4.96E-01	7.82E-08
200	1.18E+00	1.46E-03	2.43E-02	7.28E-03	9.35E+00	9.87E-02	8.69E-08
260	3.01E-04	1.48E-02	6.61E-03	9.25E-03	4.52E+00	5.35E-01	1.14E-07
300	1.03E+00	1.77E-03	2.06E-02	9.14E-03	3.09E+00	1.66E-01	9.43E-08
360	1.81E-04	1.88E-02	6.48E-03	8.61E-03	4.44E+00	5.41E-01	9.23E-08
400	2.26E-04	1.81E-02	7.17E-03	9.18E-03	4.76E+00	5.13E-01	1.15E-07
420	2.14E-04	1.87E-02	7.42E-03	9.32E-03	4.84E+00	5.02E-01	1.20E-07

Table 5-5: Parameters of impedance model at different cycles at 100 % SOC for the cell with lower discharge voltage of 2.5 V

Cycle	C1	R1	R2	W1	P	n	L
Initial	1.36E-06	8.66E-03	6.56E-03	5.07E-03	1.10E+00	7.80E-01	7.22E-08
100	2.14E-07	9.09E-03	7.67E-03	3.80E-03	3.16E+00	6.21E-01	7.68E-08
150	1.81E-06	1.01E-02	3.26E-03	1.29E-02	5.63E-01	9.05E-01	8.62E-08
300	1.72E-10	1.01E-02	6.57E-03	7.95E-03	3.11E+00	6.21E-01	8.55E-08
350	7.65E-10	1.09E-02	5.60E-03	9.09E-03	2.49E+00	6.60E-01	8.38E-08
400	2.34E-09	1.07E-02	3.85E-03	1.24E-02	1.08E+00	7.91E-01	6.76E-08
450	1.41E-09	1.10E-02	5.27E-03	9.88E-03	1.95E+00	7.05E-01	7.96E-08
500	2.82E-11	1.14E-02	6.62E-03	8.72E-03	3.86E+00	5.78E-01	6.84E-08
550	4.81E-13	1.20E-02	6.25E-03	8.64E-03	2.85E+00	6.43E-01	6.04E-08
600	3.90E-11	1.26E-02	7.80E-03	7.06E-03	5.70E+00	5.11E-01	7.89E-08
650	3.24E-07	1.26E-02	7.80E-03	7.06E-03	5.70E+00	5.11E-01	7.90E-08
700	3.38E-07	1.38E-02	6.85E-03	8.78E-03	4.32E+00	5.54E-01	8.31E-08

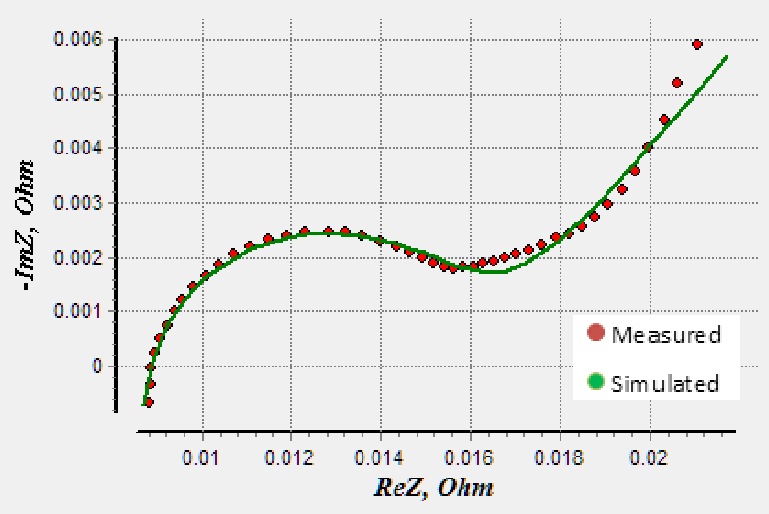

Figure 5-14: Impedance comparison between measured and simulated initially before elevated cycling with a lower discharge voltage of 2.5V

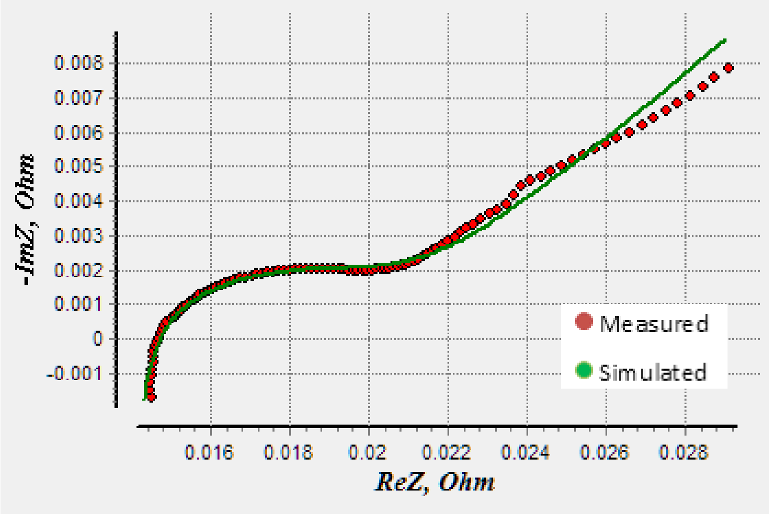

Figure 5-15: Impedance comparison between measured and simulated after 700 cycles and 20.81% capacity loss with a lower discharge voltage of 2.5V

Chapter 6

Summary and Conclusions

This thesis presents the aging study performed on to different types of high energy and high power lithium-ion batteries when they were cycled at high pulsed and continuous current rates. The study is focused on the aging induced by high C rate loading. The analysis of the aging was carried out using in-situ diagnostic methods including coulomb counting and electrochemical impedance spectroscopy (EIS). The capacity as a function of cycle number was periodically analyzed for each cell to evaluate the progression of the state of health.

The aging study performed on three 3 Ah $LiNiCoAlO_2$ (NCA) lithium-ion batteries shows that when the cell is discharged within a high C pulsed rate manner, the cell aging is accelerated when compared to the manner in which a similar cell ages when cycled with a high C rate continuous discharge rate which has the same average C rate as the high pulsed discharge experiment. The cells evaluated under high C pulsed discharge rates, high C continuous discharge rates, and nominal rate cycling saw a capacity fade of 20.18%, 5.67%, and ~0% respectively after 400 cycles each.

A similar study was performed on two K2 26650 2.6 Ah $LiFePO_4$ lithium-ion batteries where it was observed that if a cell is discharge to 2.0 V, the aging is quickly accelerated as compared to an identical cell which was cycled in a similar manner but to only 2.5 V. The cell discharged to 2.0 V lost 20.12% of its initial capacity after 420 cycles whereas the cell discharged to 2.5 V lost 20.81% capacity after 700 cycles.

From an electrical engineering perspective, modeling the electrical response of a cell as a near perfect voltage source in its continuous voltage range is often enough for the design of an application. Characterizing the aging and further postmortem analysis of the cell, where it is taken apart and studied, is often beyond the scope of an electrical engineering. Thus, an EIS method has been used to help better understand the electrical as well as the physical parameters changing within a cell without taking it apart. The EIS results obtained from the 3 Ah $LiNiCoAlO_2$ (NCA) lithium-ion batteries show an increase in the lithium loss rate when the cell is subjected to high C rate pulsed discharge cycling. In the study of two K2 26650 2.6 Ah $LiFePO_4$ lithium-ion battery, the EIS results show an increase in electrolyte resistance and charge transfer resistance. However, the cell with lower discharge of 2.0 V could have aged earlier due to graphite exfoliation and cracking causing gas formation and reducing electron count in the cell system [5][49][50].

References

[1] Ra, Issac., “Evolution of rechargeable lithium-ion battery,” International workshop energy storage technologies and application, ABD, Apr. 3, 2013.

[2] JM Energy Lithium-ion Capacitor Presentation, “ULTIMO” [Online]. Available: http://www.jmenergy.co.jp/en/product.html, JM Energy Corporation, Copyright(C), July 2010.

[3] G. Sarre, Ph. Blanchard, M. Broussely, “Aging of Lithium-ion batteries,” Journal of Power Sources, vol. 127, pp. 65-71, 2004.

[4] M. Broussely, Ph. Biensan, F. Bonhomme, Ph. Blanchard, S. Herreyre, K. Nechev, R.J. Staniewicz, “Main aging mechanisms in Li ion batteries,” Journal of Power Sources, vol. 146, pp. 90-96, 2005.

[5] J. Vetter, et. al., “Aging mechanisms in lithium-ion batteries,” Journal of power sources, vol. 147, pp. 269 – 281, 2005.

[6] Y. Chen and A. Sitzman, "Testing a Lithium-ion Battery as a Pulsed Power Source,” in 15th IEEE International Pulsed Power Conference, Monterey, 2005

[7] P. Novak, D. Wetz, B. Shrestha, G. Sarkar, J. Kelley, J. Reed. “Recharge of Electrochemical Energy Storage Devices at Pulsed Elevated Rates,” 18th IEEE International Pulsed Power Conference, Chicago, Illinois, June 19-23, 2011.

[8] Saft America, "Data sheet for the Saft VL 5U - Ultra high power cell," Space & Defense Division Inc., Doc No. 54073-2-1009, Edition: October , 2009.

[9] GAIA Advanced Lithium Battery Systems [Online]. Available: http://www.gaia-akku.com/en/gaia-cells.html, © 2011, LTC, May 16, 2012.

[10] Maxwell Technologies, K2 Series Ultracapacitors datasheet, [Online]. Available: http://www.maxwell.com/products/ultracapacitors/docs/DATASHEET_K2_SERIES_1015370.PDF.

[11] J Li, E Murphy, J Winnick, and P A Kohl, "Studies on the Cycle Life of Commercial Lithium-ion Batteries During Rapid Charge-Discharge Cycling," Journal of Power Sources, no. 102, pp. 294-301, 2001.

[12] L. Serrao, Z. Chehab, Y. Guezennee, G. Rizzoni, "An aging model of Ni-MH batteries for hybrid electric vehicles," Vehicle Power and Propulsion, 2005 IEEE Conference, pp.8, 7-9 September 2005.

[13] R. Kroezee, and P. Krein, "Electrical Battery Model for Use in Dynamic Electric Vehicle Simulations," Power Electronics Specialists Conference, pp. 1336 – 1342, 15-19 June 2008.

[14] O. Tremblay, L. A. Dessaint, and A. I. Dekkiche, "A Generic Battery Model for the Dynamic Simulation of Hybrid Electric Vehicles," Vehicle Power and Propulsion Conference, pp.284,289, 9-12 Sept. 2007.

[15] K2 Energy Solutions , K2 Energy LPF26650P Cell Data Sheet [Online]. Available: http://store.peakbattery.com/lfp-26650-p-hi-.html, May 16, 2012

[16] Saft Americas, www.saftbatteries.com, © 2007, Saft, May 16, 2012.

[17] R. Allen and J. Neri, "A Battery Powered, 200-kW Rapaid Capacitor Charger for a Portable Railgun in Burst Mode Operation at 3 RPS," 16th IEEE International Pulsed Power Conference, vol. 2, June 2007.

[18] C. Nunnally, J.R. Mayes, C.W. Hatfield, and J.D. Dowden, "Design and Performance of an Ultra-Compact 1.8-kJ, 600-kV Pulsed Power System," Proceedings of the 17th IEEE International Pulsed Power Conference, pp. 930-933, Washington, D.C., June 29 – July 2, 2009.

[19] B. Cadilhon, B. Cassany, J.-C. Diot, P. Modin, E. Merle, L. Pecastaing, M. Rivaletto, A. Silvestre de Ferron, V. Bertrand, "Self-Contained, Hand-Portable,

and Repetitive Ultrawideband Radiation Source," IEEE Transactions on Plasma Science, vol. 39, Issue 6, Part 2, pp. 1549-1559, 2011.

[20] A.J. Dragt, A.J. and J.M Elizondo, "Compact Battery-Powered, 400-kV, 40-Joule Marx Generator," Pulsed Power Plasma Science Digest of Technical Papers, vol. 2 pp. 1555-1558, 2001.

[21] Y. Teramoto, D. Deguchi, S. Katsuki, T. Namihira, H. Akiyama, and I.V. Lisitsyn, "All-Solid-State Trigger-less Repetitive Pulsed Power Generator Utilizing Semiconductor Opening Switch," Pulsed Power Plasma Science Digest of Technical Papers, vol. 1, pp. 540-543, 2001.

[22] S.K. Lyubutin, S.N. Rukin, B.G. Slovikovsky, and S.N. Tsiranov, "Experimental Study of SOS-based Generator for Low Impedance Load," Proceedings of the 12th IEEE Pulsed Power Conference, vol. 2, pp. 1230-1233, 1999.

[23] A. Bushlyakov, et. Al., "Solid-State SOS-Based Generator Providing a Peak Power of 4 GW," IEEE Transactions on Plasma Science, vol. 34, No. 5, pp. 1873 – 1878, October 2006.

[24] T. Tang, F. Wang, A. Kuthi, and M.A. Gundersen, "Diode Opening Switch Based Nanosecond High Voltage Pulse Generators for Biological and Medical Applications," IEEE Transactions on Dielectrics and Electrical Insulation Vol. 14, No. 4; August 2007.

[25] Issues in Physics and Society, "The Rocking Chair Battery (Lithium Ion Batter)", [Online]. Available: http://physicsandsocietybc.wordpress.com/2013/04/03/the-rocking-chair-battery-lithium-ion-battery/, April 3, 2013.

[26] F.E. Peterkin, B.J. Hankla, J.L. Stevens, J.F. Sharrow, D.C Stoudt, "Compact Marx Generator Test System," 25th IEEE Power Modulator Symposium, pp. 399-402, June 30 – July 3, 2002.

[27] A. Lewandowski, M. Galinski, “Practical and Theoretical Limits for Electrochemical Double-Layer Capacitors,” Journal of Power Sources, Vol. 173, Issue 2, pp. 822-828, November 2007.

[28] Maxwell Technologies Ultracapacitors, [Online]. Available: http://www.maxwell.com/ultracapacitors/products/large-cell/bcap0650.asp, © 2010 Maxwell Technologies, Inc.

[29] JSR Micro, “ULTIMO Lithium-Ion Capacitor,” [Online]. Available: http://www.jsrmicro.com/index.php/EnergyAndEnvironment/LithiumIonCapacitor/, © 2011, JSR Micro, May 16, 2012.

[30] Z.A Styczynski, P. Lombardi, R. Seethapathy, M. Piekutowski, C. Ohler, B. Roberts, and S.C. Verma, Electric Energy Storage and its Tasks in the Integration of Wide-Scale Renewable Resources,” Integration of Wide-Scale Renewable Resources Into the Power Delivery System, 2009 CIGRE/IEEE PES Joint Symposium, Calgary, Al Berta, Canada,pp. 1-11, 29-31 July, 2009.

[31] S.M. Lambert, V. Pickert, J.Holden, X. He, and W. Li, “Comparison of Supercapacitor and Lithium-Ion Capacitor Technologies,” 5th IET International Conference on Power Electronics, Machines and Drives, Brighton, UK, April 19-21, 2010.

[32] M.M. Joglekar, N. Ramakrishnan, “Cyclic Capacity Fade Plots for aging studies of Li-ion cells,” Journal of Power Sources, vol. 230, pg. 143-147, 15 May 2013.

[33] John Wang, Ping Liu, Jocelyn Hicks-Garner, Elena Sherman, Souren Soukiazian, Mark Verbrugge, Harshad Tataria, James Musser, Peter Finamore, “Cycle-life model for graphite-LiFePO4 cells”, Journal of Power Sources, vol. 196, iss. 8, pg. 3942-3948, 15 April 2011.

[34] Karthikeyan Kumaresan, Qingzhi Guo, Premanand Ramadass, Ralph E. White, “Cycle life performance of lithium-ion pouch cells”, Journal of Power Sources, vol. 158, iss. 1, pp. 679-688, 14 July 2006.

[35] C. Brissot, M. Rosso, J.-N. Chazalviel, S. Lascaud, “Dendritic growth mechanisms in lithium/polymer cells,” Journal of Power Sources, vol. 81–82, pp. 925-929, September 1999.

[36] N. D. Williard, “Degradation Analysis and Health Monitoring of Lithium-Ion Batteries”, M.S. Thesis, Dept. of Mechanical Engineering, Univ. of Maryland, College Park, MD, 2011.

[37] V. Agubra and J. Fergus, “Lithium-ion Battery Anode Aging Mechanisms”, Materials 2013.

[38] G. Ning, B. Haran, and B. N. Popov, “Capacity fade study of lithium-ion batteries cycled at high discharge rates”, Journal of Power Sources, vol. 117, pp. 160-169, 2013.

[39] D.A. Wetz, B. Shrestha, P. Novak, and Y. Chen, “Characterization of High Power Electrochemical Energy Storage Devices for use in Naval Applications,” Proceedings of the American Society of Naval Engineers Electric Machines Technology Symposium (EMTS) 2012, Philadelphia, Pennsylvania, 23-24 May 2012.

[40] B. Shrestha, D.A. Wetz, and P. Novak, “Pulsed Elevated Rate Discharge of Electrochemical Energy Storage Devices,” IEEE Transactions on Plasma Science, vol. 40, no. 10, Part: 1, pp. 2462 – 2469, 2012.

[41] D.A. Wetz, B. Shrestha, P. Novak, and Y. Chen, “Cycling of Electrochemical Energy Storage Devices at Elevated Rates,” Journal of Directed Energy, vol. 4, no.4, pp. 211 – 231, 2012.

[42] D.A. Wetz, B. Shrestha, and P. Novak, “High Power Electrochemical Energy Storage for Directed Energy Applications,” SAE Int. J. Passenger. Cars - Electron. Electr. Syst. / vol. 6, Issue 1, May 2013.

[43] A. Lasia, “Electrochemical Impedance Spectroscopy and Its Applications, Modern Aspects of Electrochemistry,” B. E. Conway, J. Bockris, and R.E. White, Edts., Kluwer Academic/Plenum Publishers, New York, vol. 32, pp. 143-248, 1999.

[44] H. Shih, and T.Lo, “Electrochemical Impedance Spectroscopy for Battery Research and Development,” Solatron Analytical Technical Report, 1996.

[45] S. Santhanagopalan, P. Ramadass, and J. Zhang, “Analysis of internal short-circuit in a lithium-ion cell,” Journal of Power Sources, vol. 194, pp. 550-557, 2009.

[46] S. K. Rahimian, S. Rayman, and R. E. White, “Optimal charge rates for a lithium-ion cell,” Journal of Power Sources, vol. 196, pp. 10297-10304, 2011

[47] W. A. Lynch, and Z. M. Salameh, “Electrical component model for a nickel cadmium electric vehicle traction battery”, IEEE Power Engineering Society General Meeting, pp. 5, 2006.

[48] J. L. Jespersen, A. E. Tonnesen, K. Norregaard, L. Overgaard, and F. Elefsen, “Capacity measurements of Li-Ion batteries using AC impedance spectroscopy,” World Electric Vehicle Journal, vol. 3, 2009.

[49] W. Kong, H. Li, X. Huang, and L. Chen, “Gas evolution behaviors for several cathode materials in lithium-ion batteries,” Journal of Power Sources, vol. 142, pp. 285-291, 2005.

[50] K. Kumai, H. Miyashiro, Y. Kobayashi, K. Takei, and R. Ishikawa, “Gas generation mechanism due to electrolyte decomposition in commercial lithium-ion cell,” Journal of Power Sources, vol 81-82, pp. 715-719, 1999.

[51] A. Sitzman, D. Surls, and J. Mallick, “Design, Construction, and Testing of an Inductive Pulsed-Power Supply for a Small Railgun,” IEEE Trans. on Magnetics, vol. 43, no. 1, pp. 270 – 274, January 2007.

[52] D. W. Dennis, V. S. Battaglia, and A. Belanger, “Electrochemical modeling of lithium polymer batteries,” Journal of Power Sources, vol. 110, no. 2, pp. 310-320, 2002.

[53] P. Rong and M. Pedram, “An analytical model for predicting the remaining battery capacity of lithium-ion batteries,” in Proc. Design, Automation, and Test in Europe Conf., 2003, pp. 1148-1149

[54] M. Chen and G. A. Rincon-Mora, “Accurate electrical battery model capable of predicting runtime and I-V performance,” IEEE Transaction onEnergy Conversion, vol. 21, no. 2, pp. 504-511, June 2006.

[55] S. Buller, M. Thele, R.W. D. Doncker, E. Karden, "Impedance-based simulation models of supercapacitors and Li-ion batteries for power electronic applications," IEEE Transactions on Industry Applications, vol.41, no.3, pp.742,747, May-June 2005.

[56] A123 Systems Inc., Cell Data Sheet, [Online]. Available: http://www.a123systems.com/, May 16, 2012.

[57] V. Lordi, J. Pask. M. Ong, and E. Draeger, “Li-ion battery solid-electrolyte interphase”, Lawrence Livermore National Laboratory, [Online] http://qsg.llnl.gov/node/40.html, 2013.

Biographical Information

Biju Shrestha was born in Nepal in 1985. He received the B.Sc. degree in electrical engineering from The University of Texas at Arlington (UT Arlington) in 2008. He was an associate RF engineer at MobileComm Professionals Inc. from 2008 to 2010. From 2010 to the time of this writing he has worked as a Graduate Research Assistant (GRA) in the UT Arlington Pulsed Power and Energy Laboratory (PPEL). He is a member of the IEEE and electrochemical society, and has actively published in their literature. His research interests include pulsed power, energy storage, and power system analysis.